Supplementary Materials: Recurrent Gene-Level Responses beneath Divergent Alternative Polyadenylation across Human and Mouse Reprogramming Routes

Sida Li, Zixuan Wang, Yanshi Hu, Qingyang Ni, Yuhao Chen, Yueming Hu, Shilong Zhang, Cong Feng and Ming Chen

S1. Supplementary methods

S1.1. Data, read recovery and cell processing

S1.1.1. Study units and analysis membership

Seven public 10× Genomics Chromium 3′ studies were analyzed (Table S1b): Xing2020 (GSE118258), Liu2020 (GSE150311), Guan2022 (GSE178325, the single-cell component of SuperSeries GSE188461), and Panariello2023 (GSE221739) in human, and Guo2019 (GSE103221), Schiebinger2019 (GSE115943, with related accession GSE122662), and Jaber2022 (GSE171127) in mouse [1–7]. Each Gene Expression Omnibus (GEO) study counted once, with related accessions, induction routes, and the donor-specific series in Guan2022 treated as parts of one study. Of 210 aligned libraries, 161 entered the expression atlas (59 human and 102 mouse), while 49 (including the Guo2019 mature embryonic-stem-cell reference and the Schiebinger2019 serum branch) served only for alternative polyadenylation site (PAS) discovery (Section S1.10). Table S1c records deposited GEO sample metadata separately from cell-state annotations, and Table S1d lists atlas membership.

Study eligibility followed state and reference availability (Table 1 of the main text, Figure S3c). Documented-source P–S contrasts used Xing2020 and Guan2022 (donor series 0618 and 0809) in human and Guo2019–CIP and Schiebinger2019–2i in mouse, excluding Liu2020 (no separable documented-source library) and Panariello2023 (unrecoverable day-0 controls GSM6894025 and GSM6894026, leaving an induced day-3 reference as earliest sample). Paired P–M contrasts used Xing2020, Liu2020, and Panariello2023 in human and the same two mouse routes, whereas Jaber2022 (no P state) entered only the atlas, state-resolved displays, and observed-S M–S comparisons. Cross-species documented-source comparisons crossed the two eligible studies per species, and interval reconstruction used Xing2020, Liu2020, Guo2019–CIP, and Schiebinger2019–2i.

S1.1.2. Read recovery and alignment

All libraries were realigned with Cell Ranger v6.0.2 [8] against refdata-gex-GRCh38-2024-A or refdata-gex-GRCm39-2024-A, excluding intronic reads from expression counts and taking PAS reads from genomic BAMs. Paired FASTQ files were rebuilt from 10× BAMs with `bamtofastq` for Xing2020 and recovered via the Waddington-OT workflow for Schiebinger2019 where standard Sequence Read Archive (SRA) exports omitted barcode reads. For Panariello2023, `fasterq-dump` (`--split-files --include-technical`) exported index reads, read 1 containing the cell barcode and unique molecular identifier (UMI), and transcript read 2 across two sequencing runs staged as separate Cell Ranger lanes. Five Panariello2023 samples (GSM6894025, GSM6894026, GSM6894031, GSM6894038, and GSM6894041) were excluded because deposited matrices contain only gene counts and their ten SRA runs had truncated read lengths (8, 49, and 16 nt versus 8, 26, and 91 nt in recoverable runs).

For Jaber2022, day 3 libraries (GSM6071749 and GSM6071750) were aligned with `SC3Pv3` (`--r1-length=26`) and day 6 and day 12 libraries (GSM5219400 and GSM5219399) with `SC3Pv2` because GEO lists v2 for all four samples whereas the publication specifies v3

for day 3 and v2 for days 6 and 12 [7], as confirmed by 10-nt raw (`UR`) and corrected (`UB`) UMI tags in the first 100,000 coordinate-ordered day 3 records. Across all 210 libraries, 176 used `SC3Pv2` and 34 used `SC3Pv3` (Table S1c). Because each Jaber2022 day 3 capture pooled approximately 7,000 reprogramming cells with 3,000 Sox2-GFP induced trophoblast stem cells [7], induction history is known only at the capture level, and those two libraries were treated as reference-admixed and excluded from complete S–R–E–P profiles.

S1.1.3. Cell quality control

Per-library thresholds over all Cell Ranger-called cells required total UMIs $u \geq \max(1500, 10^{m_u - 3d_u})$ and detected genes $g \geq \max(750, 10^{m_g - 3d_g})$, where m and d are the library median and unscaled median absolute deviation (MAD) of $\log_{10}(\max(\cdot, 1))$, alongside mitochondrial percentage at most $\min(20\%, \text{library median} + 3\ \text{MADs})$, complexity $\log_{10}(\max(g, 1)) / \log_{10}(\max(u, 10)) \geq 0.75$, and at least 100 passing cells per library. Scrublet v0.2.3 [9] was run per library with default settings (expected doublet rate 0.06, seed 0) strictly as a diagnostic without filtering cells. Schiebinger2019 membership intersected the primary-cell registry with the common-to-2i route, yielding 551,201 atlas cells: 215,114 human (Xing2020 29,000, Liu2020 12,484, Guan2022 140,593, and Panariello2023 33,037) and 336,087 mouse (Guo2019 139,248, Schiebinger2019 158,631, and Jaber2022 38,208).

S1.1.4. Study- and route-specific clustering

Outside Schiebinger2019, each analysis unit (one study or Jaber2022 subset) retained genes detected in at least ten cells, normalized counts to 10,000 per cell with $\log(1 + x)$ transformation, and standardized the top 3,000 Seurat-dispersion genes (Scanpy `highly_variable_genes` [10]) with clipping at ± 10. The first 30 of 50 principal components (randomized singular value decomposition, four power iterations) fed a 30-nearest-neighbor graph in PyNNDescent v0.5.13 [11] with directional edge weights $\exp(-d_{ij}/s_i)$, where $s_i \geq 10^{-6}$ is the median distance to the 30 neighbors of cell i, and directional weights were symmetrized by taking the maximum across each cell pair. Leiden clustering [12] optimized the Reichardt–Bornholdt configuration partition to convergence (seed 20260825 for human and 20260901 for mouse).

Cluster resolution was selected on a library-stratified 20% evaluation subset (10,000–50,000 cells, capped at unit size) across 100 library-stratified 80% resamples with fixed variable genes and principal components and a rebuilt neighbor graph. Co-clustering frequency was divided by the number of resamples containing both cells. Cell silhouettes from one minus this frequency were averaged within clusters, and the resolution yielding the most evaluation clusters among those reaching the highest 95% bias-corrected and accelerated bootstrap lower bound (25,000 draws) on the median cluster score was rerun on the full graph, so final state counts can differ from evaluation counts (Table S1e, where Guan2022, Panariello2023 and the two late Jaber2022 subsets carry review flags).

Schiebinger2019 used its route-specific partition: after log-normalizing to 10,000 counts per cell and excluding mitochondrial and ribosomal genes, 2,500 Seurat-dispersion genes were clipped at ± 10 to compute 30 principal components, and Leiden clustering (resolution 0.45, seed 218) resolved 12 states across the 158,631 common-to-2i cells, giving 62 human and 49 mouse atlas states overall (Table S1e).

S1.2. Expression-state framework and joint display

S1.2.1. Within-species expression and temporal graphs

Species-specific scVI v1.3.3 models [13,14] (seed 20260902, 3,000 study-aware Seurat-dispersion genes per species) were trained on up to 500 cells per study–series–time–condition stratum across all 59 human libraries (24,500 reference cells) and up to 500 cells per route–time stratum from the largest eligible mouse library (31,500 reference cells),

then used to encode all atlas cells into 20-dimensional species-standardized latent coordinates. Local expression graphs connected 20 nearest neighbors within each human study and mouse route (with the four Jaber2022 subsets sharing one graph) using weights $\exp[-(d_{ij}/s)^2]$, where s is the subset median neighbor distance, symmetrized by the maximum directional weight and row-normalized to kernel L. Cross-study kernel C retained reciprocal 10-nearest neighbors with $q_{ij} = d_{ij}/\sqrt{r_i r_j} \leq 2$ (r the 20th local neighbor distance), weighted by $\exp(-q_{ij}^2)$.

The temporal kernel T combined 34 human and 57 mouse within-study adjacent-time couplings (preserving registered series and separating elapsed days from ordered stages in human, excluding stage-pooled Liu2020 [2] and uncoupled Jaber2022 day-3 libraries, and following Schiebinger2019–2i, Guo2019–OSK, Guo2019–CIP and the pooled Jaber2022 day-6-to-day-12 pair in mouse). Each coupling fitted uniform-mass endpoint cells in route-standardized scVI space with moscot v0.5.0 [15] (mean-scaled costs, $\epsilon = 0.05$, $\tau_a = \tau_b = 0.95$, $\leq$ 2,000 iterations, convergence tolerance 10^{-4}), drawing 64 forward and reverse samples per cell from converged couplings (seed 20260906). The combined kernel $P = \mathrm{rownorm}(0.4L + 0.4T + 0.2C)$ was symmetrized as $(P + P^\mathsf{T})/2$, scaled to unit maximum edge weight, and embedded with UMAP [16] (200 epochs, minimum distance 0.35, spread 1.1). Transport associations organize sampled states and do not establish lineage or a common clock.

S1.2.2. Joint human–mouse embedding

The joint display used 2,128 Ensembl release 116 one-to-one ortholog pairs (`ortholog_one2one`, BioMart, 1 August 2026 [17,18]) shared between the human reference universe and stored mouse variable-gene matrices (2,023 confidence 1 and 105 confidence 0 in Table S1g, distinct from the 16,092-pair cross-species universe in Section S1.9). Integer counts across all 551,201 cells entered a joint scVI model with species as the sole batch covariate. Reciprocal 20-nearest-neighbor cross-species links were queried with FAISS v1.9.0 IVF-Flat indices [19] (4,096 lists, 128 probes, recall 94.62% human-to-mouse and 96.26% mouse-to-human on 512 random queries), retaining 265,171 links with $d_{ij}/\sqrt{r_i r_j} \leq 2.5$ (r the 20th within-species neighbor distance) weighted by $\exp[-(d_{ij}/\sqrt{r_i r_j})^2]$ to form matrix B. With block-diagonal within-species graph W, $P = \mathrm{rownorm}(0.65W + 0.35B)$ was symmetrized and scaled as above, and UMAP was initialized from median-centered native layouts aligned by orthogonal Procrustes on up to 100,000 reciprocal links (250 epochs, minimum distance 0.35, spread 1.1, seed 20260910, where parallel optimization precludes bitwise reproducibility). Local partitions, state labels, and optimal transport remained strictly within species.

S1.2.3. Annotation evidence and display families

Fixed local partitions were annotated from species-specific expression summaries (Tables S1a and S1f). Human states were assigned using fibroblast and matrix markers (DCN, LUM, collagens, PRRX1, FN1) for S/M, keratins, SPINT2, CD24, and MIR302CHG with residual source programs for E, DPPA4, DNMT3B, ESRG, L1TD1, and TDGF1 for P (requiring endogenous pluripotency markers beyond introduced factors in Panariello2023), DNMT3L, DPPA3, NLRP7, and ALPG for naive-associated candidates (hN), and TTR, APOA1, AFP, FABP1, and GATA6 for the Guan2022 endoderm-associated secretory state. Mouse annotations combined local markers with cell-level AUCell scores [20] for 14 gene sets (Table S1h, top 1,685 ranks over each library's gene universe, $\geq$ 5 matched targets, seed 20260902).

The 111 states were organized into 14 display families (S, R, E, P, M, K, hN, hX, hU, and mouse-specific mB, mN, mI, mY, mU), retaining state identifiers, species, cell counts, source annotations, and qualifications. The weaker Schiebinger2019 pluripotency subtype,

the candidate Guo2019–CIP epithelial subtype, and the Jaber2022 day-12 neural and keratin mixture kept their qualifications, and human naive-related candidates were kept distinct from the mouse neural group. In the Jaber2022 day-3 captures, epithelial and trophoblast-associated expression was read against the added reference cells [7], while GETM C002 and OSKM C002 stayed unresolved because myeloid markers were too sparse. Families summarize broad identity, process, alternative program, or unresolved membership and do not imply identical cell identities between studies.

S1.2.4. Marker displays, program scores and partition stability

Marker panels (Figures S1a–d and S2a–d) display ten core markers per species plus study-local markers (28 human and 33 mouse genes) using $\log(1 + \text{CP10K})$ (where CP10K is counts per 10,000) state–library means and detection fractions averaged equally across libraries with at least 20 state cells (all libraries for Schiebinger2019 L11). Program scores (Figures S1e, S2f and S3d) averaged $\log(1 + \text{CP10K})$ across fixed modules in library–state units with at least 20 cells: extracellular matrix (COL1A1, COL3A1, DCN, LUM, FN1), epithelial (CDH1, EPCAM, KRT8, KRT18) and pluripotency (human DPPA4, DNMT3B, ESRG, L1TD1, TDGF1 and mouse Dppa4, Esrrb, Zfp42, Dppa5a, Tdgf1).

Partition stability was evaluated on each unit's fixed graph across nine Leiden runs (selected and adjacent grid resolutions across seeds 20260913–20260915, with the selected resolution and seed reproducing all 11 partitions exactly), reporting each state's median best-match Jaccard index J and display-family compatibility fraction F (values < 0.80 flagged in figures, unit-level adjusted Rand indices [ARI] in Table S1e). Within-library boundary-state contrasts (Figure S2e,g) compared AUCell (mouse) or fixed-module (human) scores against pooled same-family states in libraries with at least 20 cells per group for Schiebinger2019–2i L00 versus L03/L06 (R), Guo2019–CIP C012 versus C008/C009/C011 (E), and Xing2020 C005 versus C004/C006 (E).

S1.2.5. Evaluation of the joint display

Joint-display evaluation covered seven series (453,242 cells, 143 libraries, 12 human–mouse route pairs): Xing2020, Guan2022 donor series 0605 and 0618, and Panariello2023 in human, plus Guo2019–OSK, Guo2019–CIP and Schiebinger2019–2i in mouse (Guan2022–0605 entered this evaluation and the observed-S R–S overview, whereas 0809 entered documented-source and observed-S P–S comparisons). The 62×49 state-pair map (Figure S3e) normalized cross-species edge weights by each human state's outgoing weight. Held-out expression support (Figure S3f) evaluated 2,000 disjoint orthologs across 875 state–library units centered gene-wise on study baselines (libraries weighted equally within states, then states weighted equally), comparing the edge-weighted mean Spearman correlation across unique human-to-mouse edges against 200 permutations of mouse units within human-library $\times$ mouse-library strata (keeping strata with < 2 units per side fixed). Across 12 full-atlas scVI refits (original or symmetric features, species or species–study batch, seeds 20260913–20260915, all 12 kept in the denominator), support required positive excess (observation minus null mean) and an observation above the 97.5th null percentile, and because connections and nulls vary across refits, excess values are graph-conditional summaries.

S1.3. PAS catalog and integrated reference

S1.3.1. Study catalogs and counting

PASs were called with polyApipe v0.1.0 (commit `43d866e15b22`) [21] in documented multi-sample mode on barcode-filtered Cell Ranger BAMs of the 161 atlas libraries. First, poly(A)-ending reads were extracted per library, and for each study these per-library poly(A) BAMs were passed together to polyApipe (`--polyA_bams --no_count`) to call one

common peak set (GFF) per study without cross-study pooling. Under default parameters (mapping quality $\geq$ 10, poly(A) tail $\geq$ 5 A with no non-A base, peak depth $\geq$ 1 non-duplicate barcode/UMI-tagged poly(A) read without cross-library UMI deduplication, and a 250-nt upstream window retaining the deeper peak among same-strand overlaps so peaks are $\geq$ 251 nt apart), each native peak was treated as one PAS without further clustering. Study catalogs comprised 206,705 (Xing2020), 113,976 (Liu2020), 1,105,589 (Guan2022), 546,693 (Panariello2023), 253,922 (Guo2019), 242,936 (Schiebinger2019) and 169,324 (Jaber2022) peaks, with polyApipe's read-based mispriming flag retained solely as provenance.

Every library was then counted against its study catalog: featureCounts v2.0.6 [22] assigned single-mapping, non-multi-overlapping reads in each 250-nt window (`-t polyAends -g peak -F GTF -f -s 1 -R BAM`), and UMI-tools v1.1.5 [23] deduplicated UMIs per peak and cell by chromosome (`--per-gene --gene-tag=XT --per-cell --umi-tag=UR --cell-tag=CB`, directional method, edit distance 1). Counts include all window reads (not only poly(A) reads), and because every study PAS was counted in every library of that study, a zero is an observed zero. Counts were summed within the fixed cell-to-metacell map across all 551,201 cells and 11,104 metacells, conserving integer totals (10,927,812,289 UMIs).

S1.3.2. Coordinates, annotation and analysis layers

Each native peak was converted to a zero-based interbase cleavage cut (GFF end on the positive strand, GFF start minus one on the negative strand) and annotated against GENCODE v44 (GRCh38) or GENCODE M33 (GRCm39, both Ensembl 110), retaining all candidate assignments and exclusion reasons. Candidates were identified within a 51-nt window around the genomic-base coordinate (interbase cut minus one on the positive strand, unchanged on the negative strand) using 250-, 1,000- and 2,000-nt transcript-end zones (2,000-nt gene-downstream bound). Priority followed same-strand annotated 3′ untranslated regions (3′ UTRs) and terminal exons, core transcript ends (0–250 nt downstream, inclusive), other exons, terminal and other introns, and downstream transcript ends ($250 < d \leq 2000$ nt), selecting the nearest transcript end per tier and marking exact cross-gene distance ties as ambiguous. Core assignments were preserved when another same-strand gene had an exonic candidate (recording the overlap), and opposite-strand overlaps did not override a same-strand assignment. Downstream rescue assignments, ambiguous or nonterminal assignments, and terminal-exon coding-sequence overlaps without UTR support were excluded from the primary layer and retained only for sensitivity. An internal-priming screen flagged cuts whose 20 downstream gene-strand nucleotides had an A fraction $\geq$ 0.8 or a run of at least eight A bases. Primary sites had an unambiguous same-strand terminal assignment and no flag, whereas flagged and sensitivity-only sites formed a relaxed tier excluded from the two primary analysis layers defined below. No splice-junction, A-stretch-mask or other post-calling filter was applied, and annotation never altered the count matrix. Of 2,639,145 catalog sites, 385,068 were primary (Table S2a).

Main analyses used the reference-supported layer (301,489 primary sites within 50 nt of a same-strand integrated reference cut), while the expanded primary layer retained all 385,068 primary sites as a sensitivity layer. Position weights were always computed on each gene's complete primary catalog, so the two layers share each gene's axis (Section S1.4).

S1.3.3. Integrated PAS reference

The integrated reference (release dated 3 October 2026) merged PolyASite v2.0, PolyA_DB v4.1 Main and GENCODE `polyA_site` records (human release 40, mouse release M25) [24–27] in that priority order. Within each source, records were ordered

by descending mean expression (without comparing scores across sources, resolving ties transcript-downstream) and assigned to the nearest same-strand representative within 10 nt (ties downstream, without chained propagation) or founded a new representative. PolyASite and PolyA_DB coordinates were converted from one-based to zero-based retained-base positions, and GENCODE records wider than 2 nt were excluded (71 human, 37 mouse), retaining the rightmost genomic base of 1–2-nt `polyA_site` records. This yielded 745,275 human representatives (568,982 founded by PolyASite, 167,526 by PolyA_DB and 8,767 by GENCODE) and 469,698 mouse representatives (300,999, 164,113 and 4,586).

One-base BED intervals were converted to interbase cuts (BED end on the positive strand, BED start on the negative strand). Human hg38 contig names were reconciled with GRCh38, retaining all 745,275 human representatives. Lifting mouse mm10 intervals to GRCm39 with UCSC `liftOver -multiple -minMatch=1` [28] excluded multiple mappings, non-single-nucleotide mappings, and invalid contigs, leaving 469,449 unique mappings, 249 unmapped records, and seven target collisions (469,442 distinct GRCm39 cuts). Inclusive matching windows of 25, 50 (defining reference support), and 100 nt were recorded with source provenance tags, noting that reference coverage describes annotation support rather than PAS-calling accuracy.

S1.3.4. Measurement checks

Sequence context (Figure S4b) was evaluated in 201-bp transcript-oriented windows around primary PASs as AATAAA and ATTAAA start frequencies (upstream signal at -40 to -10 bp), comparing 1,000 random primary PASs per study and layer against GC-matched (± 0.05) genomic positions in the same region class (3′ UTR, coding sequence, intron or other) at least 100 bp from any primary or reference cut (548–619 matches per study). Read-end profiles (Figure S4c) tallied non-duplicate whitelisted reads in 5-bp bins over ± 400 bp around 1,000 seeded primary PASs per layer (> 400 bp from other same-strand primary PASs, ≥ 1 UMI) in the lower-median UMI library of each study. Figure S4d reports complete S–R–E–P profile gene counts in the three fitting routes at 20, 40 and 80 PAS UMIs per metacell.

S1.4. DWUI, metacells and state comparisons

S1.4.1. DWUI and coverage rules

For each gene g with at least two primary PASs on one chromosome and strand, sites were ordered in the direction of transcription with relative position

$$r_{gj} = \frac{x_{gj} - \min_k x_{gk}}{\max_k x_{gk} - \min_k x_{gk}},$$

where x is the strand-oriented cut coordinate and extrema span the complete primary catalog of the gene in that study. Each analysis layer selected at least two sites for the distance-weighted PAS usage index (DWUI) without renormalizing r_{gj}, so axis ends can lie outside the reference-supported subset.

Metacells were constructed per library with SEACells [29] from log-normalized highly variable gene expression (10,000 counts per cell, up to 30 principal components, 15-neighbor kernel, 10–100 iterations, target size $\sim$50 cells, seed 20260905) independently of time or state labels. For gene g and metacell m with UMI count c_{mi} at selected site i,

$$\mathrm{DWUI}_{gm} = \frac{\sum_{i \in g} c_{mi}\, r_{gi}}{\sum_{i \in g} c_{mi}}.$$

Values from fewer than 20 PAS UMIs were missing, and zero-count sites retained their weights. Metacells required majority-state purity ≥ 0.8. Each library–state group required

at least three qualifying metacells and 30 cells, and each gene required at least three metacells with $\geq$ 20 PAS UMIs. The observed-S overview (Figure 1d, upper) and state-resolved profiles (Figure S20) applied the 30-cell gate to the whole group, whereas endpoint contrasts required the gene-qualified metacells themselves to total at least 30 cells. Averaging gene-qualified metacell usage vectors within each library–state group yielded library–state DWUI values equal to the mean metacell DWUI. Within a route, a gene required at least two count-supported sites ($\geq$ 10 UMIs in $\geq$ 2 metacells). Target-minus-reference differences define ΔDWUI (negative for proximal shifts).

S1.4.2. Reference designs and estimators

Three reference designs were kept distinct. (i) The observed-S overview (Figure 1d, upper, Figure S5a, left) averaged library-balanced DWUI(state)$-$DWUI(S) with equal gene weight over all available genes for each state and route, where S cells could include induced or mixed samples, and a route-specific fixed background of genes measurable in S and every observed R, E, P or M state served as a sensitivity (Figure S5a, right). (ii) The documented-source P–S contrast used D0, source or Stage I day-0 libraries as reference, requiring estimable library–state means at both ends and at least two PASs each supported by ten pooled UMIs in two metacells across the pair. Effects were computed for every target–source library pair and aggregated by five-level hierarchical equal weighting: target dates equally, target sampling units equally within a date, source dates equally within a target unit, source units equally within a source date, and library pairs equally within a unit pair. This estimator served the global summaries (Figure 1d, lower, Figure S5b–d) and within-species recurrence, with the two donor-specific series in Guan2022 (0618 and 0809) displayed separately but counted as one study. (iii) Paired P–M compared P and M co-captured in the same physical library and averaged within-library contrasts through the same unit and date hierarchy. Common P/M/S analyses applied one shared weight vector across all three states so that $\mathrm{P}-\mathrm{S} = \mathrm{P}-\mathrm{M} + \mathrm{M}-\mathrm{S}$ identically (Section S1.6), whereas native estimates used each contrast's own contributors. Global summaries weighted genes equally in means, medians and distal excess $(n_{\geq\tau} - n_{\leq-\tau})/n$ ($\tau = 0.02$ or 0.05, keeping subthreshold genes in the denominator).

S1.4.3. Marker-defined reference

Within-library M was also redefined from two marker programs, pluripotency (DPPA2, DPPA4, SALL4, and TDGF1) and extracellular matrix (COL1A1, COL3A1, DCN, LUM, and FN1). Counts per 10,000 over all genes were log-transformed and standardized across candidate metacells of each route and physical library, requiring at least two variable markers per program. A metacell was assigned to marker-defined M (M*) when it lay in the upper third of the matrix program and lower third of the pluripotency program with at least two high-side markers at one or more counts per 10,000 and at most one opposite-side marker expressed, with P* defined inversely. The planned common-background comparison across P–M*, P*–M, and P*–M* was not estimable in Guo2019–CIP (which yielded only three P* metacells, all in cluster-defined E outside paired P–M libraries) or Guan2022 (which lacks paired P–M). A pre-specified single-replacement design therefore matched backgrounds for one replacement at a time, keeping cluster-defined P and replacing M with M* on identical genes, libraries, and weights (Table S10a). Cross-species direction pairing (100,000 permutations per definition, threshold, and model) replaced M with M* in human only (primary) or in both species (control) across the 728 one-to-one orthologs of the cluster-defined P–M background measurable in at least two studies per species under both M and M* (Table S10b).

S1.4.4. Measurement settings and backgrounds

Four measurement settings were evaluated: reference-supported PASs at purity $\geq$ 0.8 (primary), purity $\geq$ 0.9, at least five qualifying metacells per end, and expanded primary PASs at purity $\geq$ 0.8. Each setting was crossed with four gene backgrounds (16 combinations): all available genes, genes measurable across all four settings within the route, the species-wide intersection across all routes and settings (P–S: 3,047 human and 2,181 mouse genes, P–M: 427 and 1,040), and one-to-one orthologs measurable in every eligible series and setting (1,306 for P–S and 208 for P–M). Shifting from the supported ($\bar{s}$) to the expanded ($\bar{e}$) layer (Figure S5b, right) was decomposed into common-gene (c) re-estimation and added-gene (a) admission as $(n_c/N)(\bar{e}_c - \bar{s}_c) + (n_a/N)(\bar{e}_a - \bar{s}_c)$ with $N = n_c + n_a$. Source-library sensitivity (Figure S5c) evaluated individual documented sources in Guan2022–0618 (GSM5387809, GSM5683317) and Schiebinger2019–2i (GSM3195648, GSM3195649) across available genes, a fixed gene intersection and target libraries evaluable against every source.

S1.4.5. Tandem-3′ UTR genes

Tandem-3′ UTR genes were those whose complete primary PAS catalog lay entirely within the 3′ UTR of one stop-codon-containing terminal exon of at least one coding transcript in assembly-matched Ensembl release 116 [17] (giving identical membership in both PAS layers). Multiplying ΔDWUI by the strand-oriented primary-catalog span converted relative shifts to nucleotide differences (Figure S5d, Table S2c).

S1.4.6. Naive-related state in a single library

In the Liu2020 RSeT library GSM4546548 (11 S, 13 P and 21 hN qualified metacells at the primary setting, and 0 M metacells, Section S1.12), ΔDWUI was evaluated for hN$-$P, hN$-$S and P$-$S across the four measurement settings on genes meeting eligibility for all three contrasts so that $(\mathrm{hN} - \mathrm{S}) = (\mathrm{hN} - \mathrm{P}) + (\mathrm{P} - \mathrm{S})$ identically (Figure S5e,f).

S1.5. State-resolved DWUI profiles

S1.5.1. Candidate selection and profile classes

State-resolved profiles were referenced to S within each route under the primary setting and group-level 30-cell gate (Section S1.4), with gene expression quantified in the same metacells from counts per million (CPM) as $\log_2(\mathrm{CPM} + 1)$. Candidates were selected from three study pairs: Schiebinger2019–2i with Guo2019–CIP on S–R–E–P, Xing2020 with Guan2022–0618 on S–R–P, and Xing2020 with Liu2020 on S–E–P. Eligibility required measurements in every paired state of both studies, a DWUI range $\geq$ 0.01 across those states in each study, and Pearson correlation $\geq$ 0.6 between the two studies' centered matched-state profiles (plus a complete Xing2020 S–R–E–P profile with range $\geq$ 0.01 for the union of the two human pairs), retaining 902 human and 796 mouse genes (Table S8a).

Complete S–R–E–P profiles were mean-centered and scaled to unit Euclidean norm, averaging the two mouse routes per gene and weighting species equally against Xing2020. Species-weighted k-means (50 initializations, $\leq$ 500 iterations, tolerance 10^{-7}, seed 91327) was evaluated across k = 2–6 by species-balanced silhouette width, weighted within-cluster inertia, and minimum species cluster size, ordering classes by their center's P–S coordinate (C1 most proximal). Although $k = 2$ maximized silhouette width (Table S8a), $k = 3$ was used descriptively to separate distal-then-proximal reversal ($\max(R, E) - S \geq 0.15$ and $P \leq \max(R, E) - 0.5$ on normalized centers) from monotonic proximal change (Figure S20a,c).

S1.5.2. Path geometry

For each complete gene–route profile, total path length L, net endpoint displacement D and turn score T were defined as

$$L = |R - S| + |E - R| + |P - E|, \qquad D = |P - S|, \qquad T = 1 - D/L,$$

with endpoint retention D/L, step contributions equal to each adjacent step's absolute change divided by L, and the dominant step defined by the largest contribution. Route summaries report medians and interquartile ranges across genes (Figure S20b,d,e, Table S8d).

S1.5.3. Class identity across species

Candidate one-to-one orthologs (139 pairs, Table S8b) were cross-tabulated by human and mouse profile class against two 10,000-draw permutation nulls with fixed margins: a composition null (seed 2026100401, expected 36.0 same-class pairs) and a measurement null stratified by median splits of human and mouse expression and PAS coverage (14 occupied strata, seed 2026100402, expected 37.8). For each count C (the diagonal and nine cells) with null expectation E over B draws, two-sided $P = (1 + \#\{|C_{\text{null}} - E| \geq |C_{\text{obs}} - E|\})/(B + 1)$ was adjusted by Benjamini–Hochberg (BH) [30] across all 20 exploratory tests (q_{20}).

S1.5.4. Ranked-set tests of profile amplitude

On the background of genes with complete reference-supported S–R–E–P profiles in all fitting routes per species (4,378 human and 2,914 mouse), Gene Ontology (GO) biological-process and Kyoto Encyclopedia of Genes and Genomes (KEGG) terms [31–33] (constructed as in Section S1.6.12) were retained when they had 10–500 annotated background genes and ≥ 10 non-members. Retained terms were tested for elevated S–R–E–P range (maximum minus minimum DWUI or $\log_2(\text{CPM} + 1)$) by two-sided Mann–Whitney tests with rank-biserial correlation $2U/(nm) - 1$ and joint GO and KEGG BH correction within each layer, route and measure (7,780 tests per layer and measure across three routes, Figure S7c, Table S8c).

S1.6. Within-species recurrence and its controls

S1.6.1. Recurrence definition and measurement-matched null

Recurrence was evaluated separately by species for documented-source P–S and paired P–M on the primary setting (Section S1.4) at $|\Delta\text{DWUI}| \geq 0.02$ and ≥ 0.05. A study contributed one directional vote only when all its evaluable series shared the same sign and reached the threshold, and recurrence required same-direction votes from at least two studies (allowing an opposing study). For each species, contrast and threshold, 10,000 permutations shuffled each study's event labels (-1, 0, $+1$) among its measurable genes within the measurement-matched L3 strata defined below, preserving each study's measurable gene set and positive, negative and non-event counts. Reference DWUI and covariates (mean expression, alternative polyadenylation [APA] coverage, PAS count and directional capacity, i.e., whether every series could shift by at least the tested threshold in each direction) were reconstructed from qualified comparisons under hierarchical unit and date weights (Section S1.4), taking the median across series of a multi-series study and the minimum for directional capacity. Unless stated otherwise, each permutation test used seed 20261003 plus the first 12 hexadecimal digits of the SHA-256 hash of its test key. Sensitivities omitted the series-combination stratum, rebuilt strata and nulls under leave-one-study-out deletion (only human P–M retained two studies after every deletion, Figure S6e), or treated the two Guan2022 series as separate units in human P–S (Figure S6e).

S1.6.2. Nested nulls

The contribution of each matching layer (Figure S6a) was quantified by evaluating recurrence counts across five nested stratification levels with fixed study event margins. Within-study covariates were binned into terciles of mean expression, APA coverage, and PAS number, quintiles of reference DWUI (S for P–S, co-captured M for P–M), and binary directional capacity in each direction. L0 matched the number of eligible studies, exact combination of measurable series (for example Guan2022–0618 versus –0809), and directional capacity. L1 added expression and APA-coverage terciles to L0. L2 baseline added the reference-DWUI quintile to L1, whereas L2 PAS-first added the PAS-number tercile to L1 instead. L3 combined all covariates, reproducing the primary measurement-matched null strata with its own permutation draws. Across $B = 10{,}000$ draws per species–contrast–threshold test, one-sided upper-tail empirical P values were $P = (1 + \#\{T_{\text{null}} \geq T_{\text{obs}}\})/(B + 1)$ (10,001 denominator), with BH adjustment applied over the eight primary species–contrast–threshold tests (q_8) and over all 40 nested-null model–combination tests (q_{40}).

S1.6.3. Alternative PAS-usage summaries

Alternative summaries used the reference-supported catalog, eligibility rules, and hierarchical weights of Section S1.4, averaging PAS usage proportions p_i (including zero-count sites) across eligible metacells within library–state groups before hierarchical aggregation. For n supported PASs ordered by transcription, the rank-weighted usage index was RWUI $= \sum_i p_i i/n$, the distal and proximal PAS usage indices were PDUI $= p_n$ and PPUI $= p_1$, and for aggregated target-minus-reference differences $d_i = p_{i,\text{target}} - p_{i,\text{reference}}$, the maximum difference in proportion change was MPRO $= \max_i d_i - \min_i d_i$ (range 0–2, unsigned). With a fixed catalog and identical weights, ΔDWUI $= \sum_i r_i d_i$, and when two PASs occupy the axis ends, ΔRWUI $= 0.5\Delta$DWUI and MPRO $= 2|\Delta\text{DWUI}|$.

DWUI and RWUI were tested at thresholds of 0.02 and 0.05 and MPRO at 0.10 and 0.20 (requiring every measurable series of a study to exceed the unsigned MPRO threshold and at least two responding studies for recurrence). Metric-specific 10,000-draw L3 nulls matched series combination, expression, APA coverage, and PAS count as above, plus reference quintile and directional capacity for signed metrics or terciles of reference concentration $\sum_i p_i^2$, maximum possible redistribution, and threshold eligibility for MPRO, with BH correction per metric (q_8) and across all 24 tests (q_{24}).

S1.6.4. Measurement controls

Measurement controls recomputed gene and library eligibility, backgrounds, and recurrent counts from all qualified endpoint gene–library pairs under each perturbed setting (Figure S6c,d).

Conditional intervals. Five hundred within-library–state metacell bootstrap draws with replacement (sharing one resampled vector per draw for reused source libraries) were aggregated by the hierarchical weights (Section S1.4). Interval support required every series' percentile 95% interval to exclude zero for DWUI, or observed MPRO to exceed the 95th percentile of centered bootstrap error.

Same-state halves. Library–states with at least six qualified metacells and 60 cells were split 100 times into two halves ($\geq$ 30 cells each, requiring two PASs with $\geq$ 10 UMIs in $\geq$ 2 metacells and reusing source splits across targets) to form S/S and P/P (or M/M) pseudo-contrasts under the endpoint weighting.

Depth, cycle, and common axis. PAS counts were subsampled without replacement to exactly 20 or 40 UMIs per gene and metacell (20 draws, first draw tested in permutation and all draws summarizing stability). The P–S cycle-matching control stratified S-phase

and G2/M scores into route-specific tertiles (up to nine joint bins), weighted shared bins by the smaller state metacell count ($\geq$ 3 metacells and $\geq$ 30 cells per side), and yielded no estimable P–M comparison. Common cross-study PAS axes paired Guo2019–CIP with Schiebinger2019–2i (2,477 mouse genes) and Xing2020 with Guan2022 (3,774 human genes, leaving one eligible human P–M study) by chaining same-strand reference-supported PASs within 50 nt into clusters ($\geq$ 2 shared clusters per gene) on a 0–1 cluster-mean axis before summing counts and reapplying eligibility.

Correction. Each control was tested against 10,000 series-matched L3 permutations across one 112-position BH family (native series-matched/unmatched, interval, two depth, cycle, and common-axis settings $\times$ DWUI 0.02/0.05 and MPRO 0.10/0.20 $\times$ four species–contrast positions, with the 12 single-study positions entering as $P = 1$).

S1.6.5. Cycle scores and common support

Metacell S-phase (MCM5, PCNA, TYMS, FEN1, MCM2, MCM4, RRM1, UNG, GINS2, MCM6) and G2/M (CDK1, TOP2A, NUSAP1, CDC20, CDC45, UBE2C, BIRC5, TPX2) module scores averaged $\log(1 + \text{CP10K})$ across case-normalized symbols (resolving placeholder identifiers via the Cell Ranger GTF), and their equal-weight average defined the combined cell-cycle score. State means over purity-$\geq$ 0.8 metacells (Section S1.4) were compared within physical libraries (weighted equally per route) for paired P–M, M–S, and observed-S P–S, and via documented-source weights (Section S1.4) for documented-source P–S (Figure S18a, Table S7a). Within-library score differences were tested by two-sided library sign flips (exact for $\leq$ 20 libraries, 10,000 draws with $+1$ correction otherwise, plus 10,000-draw library-bootstrap intervals) with BH adjustment over the 14 estimable tests of the 102-position score family shared by both PAS workflows (Table S7g).

Cycle-adjusted APA comparisons sought nonnegative metacell weights (w_s, summing to one per state) within the observed common cycle-score support of each library context (five paired P/M studies and three P/M/S routes pairing target P/M libraries with documented-source S in Xing2020, Guo2019–CIP, and Schiebinger2019–2i) that equated S-phase and G2/M module means across states while minimizing $\sum_s n_s \| w_s - 1/n_s \|^2$ (alongside a 2×2 median-split bin-reweighting sensitivity). Both before and after restricting fixed context weights to gene-eligible metacells ($\geq$ 20 PAS UMIs and $\geq$ 2 jointly count-supported PASs, keeping the M–S joint-PAS filter in P/M/S), validity required four criteria across all states, state pairs, and both module scores: (i) at least three positively weighted metacells and 30 cells per state, (ii) effective sample size $1/\sum_m w_m^2 \geq 3$, (iii) absolute standardized mean difference ≤ 0.1, and (iv) weighted population-variance ratio in $[0.5, 2]$ with weighted Kolmogorov–Smirnov distance ≤ 0.2. The planned 16-position family (two PAS workflows $\times$ five P/M and three P/M/S routes) evaluated direction-aligned changes in $d\Delta\text{DWUI}_{\text{P}-\text{M}}$ or $\min(d\Delta\text{DWUI}_{\text{P}-\text{S}}, d\Delta\text{DWUI}_{\text{P}-\text{M}})$ on fixed primary candidates (with $d \in \{-1, +1\}$ denoting each candidate's primary recurrence direction) by library sign flips and bootstrap intervals. Because P and M lacked common cycle-score support, zero eligible libraries or usable P–M estimates were available in any route (Table S7g, with within-library P stratification and the human common-support window detailed in Section S1.7).

S1.6.6. Core CPA-factor expression and within-state cycle association

Eleven core cleavage and polyadenylation (CPA) factors (NUDT21, CPSF6, CSTF2, CSTF2T, FIP1L1, PCF11, CPSF1, CPSF2, CPSF3, CPSF4, PABPN1) were summarized per state as mean $\log_2(\text{CPM} + 1)$ and contrasted in paired P–M and documented-source P–S (Figure S18b, Table S7b). Within each library and state, cell-cycle score and mean DWUI across a fixed gene panel were correlated by Pearson r of their ordinary-least-squares residuals after adjusting for five standardized covariates: panel mean $\ln(1 + \text{CP10K})$,

panel mean $\ln(1 + \text{gene PAS UMIs})$, $\ln(1 + \text{cell gene UMIs})$, $\ln(1 + \text{cell PAS UMIs})$, and $\ln(\text{metacell cell count})$, requiring ≥ 5 residual degrees of freedom and nonconstant residuals (Figure S18g, Table S7a, equal library weights and 10,000-draw library-bootstrap 95% ranges).

S1.6.7. S–M contrast and within-date well differences for the shared proximal set

The 27-ortholog shared P–M proximal set and complete P–M proximal recurrent sets (144 human and 372 mouse genes) were compared between S (documented source in Xing2020, Guan2022–0618, and both mouse routes, observed S in Liu2020 and Panariello2023) and M using hierarchical date and unit weights (Section S1.4) with sign reversed to S−M, averaging measurable genes equally (27 in Xing2020, 26 in Guan2022–0618, 16 in Liu2020, 27 in Panariello2023, 27 in Guo2019–CIP, and 26 in Schiebinger2019–2i for the 27-ortholog set) alongside same-metacell cycle-score differences (Figure S19a, Table S7d). Across the 11 two-library dates (22 of 24 paired P–M libraries over 13 dates) in Schiebinger2019–2i, within-date well differences in cycle score and proximal shift ($-\Delta$DWUI) were related by the uncentered correlation $\sum XY / \sqrt{\sum X^2 \sum Y^2}$ on three 24-library gene panels (85 high-coverage genes, 45 orthologs, and 8 mouse proximal recurrent genes outside the 27-ortholog set, with leave-one-date-out ranges). On the 27-ortholog shared proximal set, within-date differences across seven prespecified two-library dates (14 libraries, 5–22 measurable genes per date) were tested for cycle score and 11-CPA-factor mean expression by enumerating all $2^7 = 128$ within-date label flips (two-sided P, q_2, Figure S19b, Table S7e).

S1.6.8. Independent wells in Schiebinger2019–2i

In Schiebinger2019–2i destructive-sampling wells [6] from one cell line with co-captured P and M, genes measurable on at least four dates having ≥ 2 qualified wells were tested across five metrics (DWUI, RWUI, PDUI, PPUI, MPRO, weighting dates equally and wells equally within dates) by synchronized sign flips of each well's equal-metacell PAS-proportion difference vector. Linear metrics used the absolute weighted mean difference and MPRO was recomputed after aggregation (exact enumeration with one sign fixed up to 18 wells, and 131,071 sampled patterns with $+1$ correction and seed $20260930 + n$ otherwise). BH adjustment was applied per metric and jointly across all $5 \times 614 = 3{,}070$ tests, with simultaneous 95% Clopper–Pearson Monte Carlo bounds flagging two boundary-uncertain calls (Figure S6f,g, Table S3d).

S1.6.9. External bulk PAS-seq

In GSE99922 bulk PAS-seq [34] (two MEF and two iPSC libraries, GSM2664305–GSM2664308), LastExon coordinates for the 604 mouse P–S recurrent candidates were mapped by gene identifier or unambiguous symbol, lifted from mm9 via mm10 to GRCm39, and matched uniquely within 50 nt to same-strand PASs under both coordinate-origin conventions (excluding overlapping $\pm$40-nt windows, multi-gene sites, and many-to-one mappings). Eligible genes (≥ 2 shared PASs, $\geq$ 100-bp span, ≥ 20 shared counts and $\geq 80\%$ LastExon count retention per library, and ≥ 2 sites with ≥ 10 pooled counts) were summarized across equally weighted replicates by total variation distance $\frac{1}{2}\sum_i |p_{i,\text{iPSC}} - p_{i,\text{MEF}}|$, MPRO, and direction-aligned position shifts, reported as median candidate excess over 1:3 non-candidate controls matched within PAS-number strata on expression, count support, external site count, shared-count fraction, span, pooled usage, and proportion impurity (with balance acceptance criteria of $\geq 80\%$ candidate retention and maximum absolute standardized mean difference [SMD] ≤ 0.20), alongside 50- or 100-count and 1:2-control sensitivities (Figure S6h). Only six whole-library label assignments exist, and because

GSE99922 may contribute to external PAS references, shared site existence is not independent support.

S1.6.10. Matched references

The 268 human and 420 mouse DWUI 0.02 P–M recurrent genes were evaluated on matched P/M/S triplets (co-captured P and M plus documented-source S in Xing2020, Guo2019–CIP and Schiebinger2019–2i) using shared weights and joint two-PAS support so that $\mathrm{P{-}S} = \mathrm{P{-}M} + \mathrm{M{-}S}$ identically (Section S1.4). A gene was P–S/P–M aligned when both matched contrasts reached 0.02 in its recurrent P–M direction in every route with matched triplets.

S1.6.11. Recurrence across opposing expression responses

On the common cross-study PAS axes of Guo2019–CIP/Schiebinger2019–2i and Xing2020/Guan2022 (eligibility as in Section S1.4), study-level APA calls ($|\Delta\mathrm{DWUI}| \geq \tau$, $\tau = 0.02$ or 0.05) and expression calls ($|\Delta\mathrm{GEX}| \geq 0.25$ in mean $\log_2(\mathrm{CPM}+1)$ across the same metacells) classified dual-responding genes into four APA-by-GEX sign-agreement classes. Enrichment of APA-same/GEX-opposite genes was tested against 10,000 permutations in both study-shuffle orientations under a response-identity null (fixing GEX relationships within strata of GEX category, APA-depth tercile, PAS count capped at four, baseline-DWUI quintile, directional capacity and measurable Guan2022 series) and a direction null (additionally fixing APA responder status), taking the larger P and smaller enrichment across orientations with BH adjustment over the eight prespecified tests (q_8, plus a 3-bin baseline sensitivity, Figure S8a–c, Table S3e).

S1.6.12. Functional backgrounds of recurrent genes

Functional enrichment of the DWUI 0.02 recurrent sets (G2, tested as pooled, proximal and distal sets) was evaluated against detected genes in ≥ 2 studies (G0) and APA-testable genes in ≥ 2 studies (G1$\subset$G0, plus G1/G0 once, totaling 28 analyses per database) using GO biological-process annotations (`go-basic.obo` of 26 July 2026, Ensembl 116 [17,18,31,32], propagated to non-root ancestors) and KEGG pathways (27 September 2026 UTC REST snapshot, PATHWAY release 25 September 2026 [33], with Ensembl-to-NCBI conversion) for terms with 10–500 annotated background genes. Exact upper tails $P(\sum_s X_s \geq h_{\mathrm{obs}})$ convolved stratum-wise hypergeometric variables $X_s \sim \mathrm{Hypergeom}(N_s, K_s, n_s)$ across nested L0–L3 strata parallel to the recurrence nulls above (using terciles for reference DWUI in L2/L3 and conditioning G0 comparisons on expression-measurable study count and mean-expression quintile from L1 onward, Figure S7a,b,d), with BH applied per comparison, across each database's 28-analysis grid (reported in the main text) and across stages. Conditional power under L3 (Figure S7e) convolved exact noncentral hypergeometric distributions at odds ratios 1, 2, 4 and 8 (at nominal 0.05 and $0.05/m$ for m terms) across five background-size quantile terms (minimum, quartiles, maximum) per G2 comparison.

S1.7. Cell-cycle stratification within P

S1.7.1. Within-library median split of P and residual cycle-score differences

Because co-captured P and M metacells lacked common cycle-score support for direct reweighting across the 36 paired P–M physical libraries (Section S1.6, Table S7g, where library sign-flip tests and within-state partial correlations are also defined), P metacells were partitioned within each physical library by their combined cell-cycle score (Table 1 and Figure 5a of the main text, Figure S18e). Across the five contributing studies, the 36 libraries (nine human: two in Xing2020, one in Liu2020 and six in Panariello2023, and 27 mouse: three in Guo2019–CIP and 24 in Schiebinger2019–2i) contained 878 purity-$\geq$ 0.8 P and 521 purity-$\geq$ 0.8 M metacells. Within each physical library, purity-$\geq$ 0.8 P metacells were

ordered by ascending combined cell-cycle score (Section S1.6, ties broken by lexicographic metacell identifier), assigning the first $\lfloor n/2 \rfloor$ metacells to the lower-cycle half (P_{low}) and the remaining $\lceil n/2 \rceil$ metacells to the higher-cycle half (P_{high}). This partition was fixed before computing any split-specific APA effects and held constant across all genes and measurement settings. Metacell and cell counts, group-level eligibility (Section S1.4) and combined cycle-score medians and interquartile ranges were recorded for M, full P, P_{low} and P_{high} in each library.

Within-library contrasts of P_{low} (and descriptively P_{high}) against co-captured M were reconstructed from the metacell-by-PAS count matrices across all four measurement settings and four gene backgrounds (both on backgrounds recomputed within P_{low} and on original full-P–M backgrounds intersected with P_{low}-measurable genes, Sections S1.4 and S1.12), recomputing gene-level eligibility, five-level hierarchical weights and covariates on the retained metacells and retaining routes without an eligible library under a stricter setting as unavailable rather than dropping them from recomputed cross-route intersections.

S1.7.2. Recurrence, cross-species direction pairing and within-P high-minus-low differences

For P_{low} relative to co-captured M on the primary setting (Section S1.4, all genes measurable in P_{low}), within-species cross-study recurrence was tested at $|\Delta\text{DWUI}| \geq 0.02$ and ≥ 0.05 in human (1,860 measurable genes across three studies) and mouse (1,089 measurable genes across two studies) against 10,000 permutations of the L3 measurement-matched null (Section S1.6) reconstructed from P_{low} covariates (base seed 20261105, one-sided upper-tail empirical P, BH q_4, Figure 5b of the main text). Proximal and distal recurrent counts were reported alongside their null means as directional components, and recurrence counts in P_{high} relative to M (1,837 human and 1,328 mouse measurable genes) were summarized descriptively.

Cross-species direction pairing for P_{low} relative to M at $|\Delta\text{DWUI}| \geq 0.02$ was evaluated on the 608 one-to-one orthologs measurable in at least two studies per species under 10,000 permutations of the full-assay conditional null (defined in Section S1.9) with quantile strata recomputed on the 608-pair inventory (one-sided upper-tail P, BH q_4 across the four directional cells, Figure 5c of the main text). For the 27 orthologs of the primary shared proximal P–M set (Section S1.9), species-specific and joint retention in P_{low} were tallied by distinguishing genes that re-qualified for cross-study proximal recurrence at 0.02 from genes measurable in at least two studies without recurrence and genes measurable in fewer than two studies.

Within-library PAS-usage differences between P_{high} and P_{low} (D) were evaluated on the primary setting for two fixed candidate sets per species: the 27-ortholog primary shared proximal P–M set (Section S1.9) and the complete primary P–M proximal recurrent sets (144 human and 372 mouse genes, Section S1.6, Figure 5d of the main text). For label assignment z, gene g and study r, $L_{gr}(z)$ denoted the physical libraries in which P_{low}, P_{high} and M all met group- and gene-level eligibility and both paired contrasts against M had at least two jointly count-supported PASs (Section S1.4). Within each library $\ell \in L_{gr}(z)$, the co-captured M reference on the shared primary PAS axis canceled identically between the two paired contrasts, giving

$$D_{gr}(z) = \sum_{\ell \in L_{gr}(z)} w_{gr\ell}(z) \left[\mu_{\text{high},g\ell}(z) - \mu_{\text{low},g\ell}(z)\right],$$

where $\mu_{\text{high},g\ell}(z)$ and $\mu_{\text{low},g\ell}(z)$ are the library–state DWUI values of P_{high} and P_{low} and $w_{gr\ell}(z)$ are the hierarchical date and sampling-unit weights renormalized over $L_{gr}(z)$ (negative D indicating more proximal PAS usage in P_{high}). The gene-level difference $D_g(z)$

averaged $D_{gr}(z)$ equally across evaluable studies, and the set statistic $T(z)$ averaged $D_g(z)$ equally across evaluable genes of the fixed set under assignment z. The null distribution drew 2,000 uniform random assignments of $\lfloor n/2 \rfloor$ lower-cycle labels within each library's purity-$\geq$ 0.8 P metacell pool (fixed jointly across all 36 libraries, both species and both candidate sets before computing observed D), recomputing eligibility, $L_{gr}(z)$, weights and $T(z)$ from the count matrices on every draw ($B_{\text{valid}} = 2{,}000$ valid draws for all four sets). Two-sided empirical P values were

$$P = \min\left\{1,\, 2\min\left(\frac{1 + \#\{T_b \leq T_{\text{obs}}\}}{1 + B_{\text{valid}}},\, \frac{1 + \#\{T_b \geq T_{\text{obs}}\}}{1 + B_{\text{valid}}}\right)\right\},$$

with BH adjustment across the two candidate sets within each species (q_2).

S1.7.3. Common cycle-score support window in human

As a complementary check restricted to the overlapping range of P and M cell-cycle scores within each physical library, the library-specific common support window over purity-$\geq$ 0.8 P and M metacells (Figure S18c) was defined as

$$[c_{\min}, c_{\max}] = \left[\max(\min P, \min M),\ \min(\max P, \max M)\right].$$

After P and M metacells were restricted to $[c_{\min}, c_{\max}]$, group- and gene-level eligibility, hierarchical weights and covariates were recomputed on the primary setting (Section S1.4). In species with at least two studies having a group-eligible library within $[c_{\min}, c_{\max}]$, P–M recurrence among genes measurable in at least two studies was tested at $|\Delta\text{DWUI}| \geq 0.02$ and ≥ 0.05 against 10,000 permutations of the window-reconstructed L3 null (Section S1.6, one-sided upper-tail P, BH q_2). Restricting metacells to $[c_{\min}, c_{\max}]$ enforces range overlap without equating within-window cycle-score distributions between P and M.

S1.8. Candidate intervals and predicted sites

S1.8.1. Candidate pools

Interval analyses used a candidate pool separate from the cohorts of Figures 1–5. The DWUI pool contained genes with same-direction $|\Delta\text{DWUI}| \geq 0.01$ in a fixed majority of studies for at least one local-state contrast on the primary setting, with coarse-state references and Guan2022–0618 for Guan2022. A study voted only when every route specified for the contrast was measurable and crossed 0.01 in the same direction, while missing or conflicting routes abstained and the denominator stayed fixed. Human P–S, M–S and P–M required three of four studies (Xing2020, Liu2020, Guan2022 and Panariello2023). Mouse R–S and E–R required Schiebinger2019–2i and both Guo2019 routes, P–E, P–S and P–M required Schiebinger2019–2i and Guo2019–CIP, and M–S required two of three studies (adding Jaber2022), yielding 1,217 human and 1,801 mouse genes. The Figure 6 union pool added the MPRO ≥ 0.10 recurrent genes of each P–S or P–M contrast and retained each gene's admission basis. Because every DWUI-pool gene carries all its planned contrasts, the union per contrast is not the set of genes supported in that contrast (Table S5a).

S1.8.2. Recognition resources and scans

MicroRNA (miRNA) sites were canonical target-side matches to mature miRNA seeds: 8mer (reverse complement of nucleotides 2–8 followed by A), 7mer-m8 (nucleotides 2–8), and 7mer-A1 (nucleotides 2–7 followed by A), and 7mers nested within an 8mer of the same seed were collapsed to the strongest type [35]. Names and accessions were reconciled to miRBase [36] (release 22.1) and MirGeneDB 3.0 [37]. Specifically, miRNAs with identical seeds were grouped (394 mouse and 372 human seeds), and mature sequences annotated `functional_mapped_rpm>10` in external bulk reprogramming small-RNA data (mouse

SRP046744, human GSE62776 and SRP049345) [38,39] were retained. RNA-binding protein (RBP) position-weight matrices came from the *Homo sapiens* and *Mus musculus* downloads of CisBP-RNA database build 2.00 [40]. Only parsable matrices directly determined for their source RBP (excluding inferred matrices) were evaluated across three layers (Table S5g): (i) 259 human-derived matrices for 145 human RBPs, (ii) seven mouse-derived matrices for six mouse RBPs (Khdrbs1, Pcbp1, Pcbp3, Pum2, Rbm38, and Rbm45, where the short Pum2 matrix cannot reach the $P < 10^{-4}$ scan threshold and therefore yields zero hits), and (iii) 202 human-derived matrices transferred to 111 mouse RBPs via high-confidence one-to-one orthologs with supporting CisBP-RNA family and RNA-binding-domain transfer records in Ensembl release 115 [17]. Transferred matrices were kept separate from mouse experimental motifs. Matrices were scanned on the annotated UTR strand with FIMO v5.5.2 [41] (`--norc`, scan threshold $P < 10^{-4}$, species-specific backgrounds). A hit counted only if it lay within every annotated UTR model of its terminal family. Non-identical overlapping hits of the same factor were dropped as ambiguous, and physical sites were deduplicated by category and coordinates with factor labels pooled to indicate sequence compatibility.

S1.8.3. Terminal families and interval inclusion

A terminal family grouped the annotated 3′ UTR models of a gene sharing the same terminal-exon start on one chromosome and strand, with the common family region defined as the stretch shared by all models of the family. A PAS was assigned to a family when its cut-site cluster lay within at least one model of that family and no model of any other family, provided that every model of the family matched a catalog UTR region and no two assigned clusters in the family overlapped. Interval analyses in Guo2019–CIP, Schiebinger2019–2i, Xing2020, and Liu2020 matched strict primary, reference-supported PASs on chromosome and strand within 50 nt to an integrated-reference identity (PolyA_DB Main, PolyASite, or GENCODE, chosen by source support, nearest distance, and deterministic ties) and summed counts per identity within study, gene, terminal family, and library–state. Single-PAS families and genes with multiple multi-PAS families were excluded. Library–states met the group eligibility rules of Section S1.4, and a contrast was modeled only when pooled family count reached 50 UMIs and pooled family coverage (the family's share of the gene's reference-supported PAS UMIs) reached 0.5 in both states. Common UTR boundaries and annotated PAS cuts partitioned each family into atomic intervals with constant inclusion masks.

For interval i in qualified library ℓ of state s,

$$I_{is\ell} = \frac{\sum_j n_{js\ell} R_{ij}}{\sum_j n_{js\ell}},$$

where $n_{js\ell}$ is the merged count of annotated PAS j in the terminal family and R_{ij} is one when that PAS retains the complete interval. With $\Delta I = I_{\text{target}} - I_{\text{reference}}$ in percentage points (pp), libraries required a family count of at least 20 or 50 UMIs and family coverage of at least 0.5. P–S used separate-state library-equal means, whereas P–M used the libraries $L_{i,k}$ qualified for both states at threshold k,

$$\Delta I_{i,\mathrm{P-M},k} = \frac{1}{|L_{i,k}|} \sum_{\ell \in L_{i,k}} (I_{i\mathrm{P}\ell,k} - I_{i\mathrm{M}\ell,k}).$$

A strict inclusion change (SIC) required same-sign changes of at least 10 pp at both 20 and 50 UMIs, with at least five included and five excluded UMIs in each compared state at 50 UMIs (in $L_{i,50}$ for P–M). Gene measurability for Figure S13a required an eligible model with

at least two annotated PASs and at least one reference and one target library at 50 UMIs in both studies.

S1.8.4. Interval agreement and partial retention

Physical sites were deduplicated by species, gene, category, chromosome, strand, and coordinates, and site-level recurrence required matching coordinates and factor, evaluability in both studies, and an SIC in the same direction. Intervals of the two studies that shared at least one site and were both strictly observed and changed formed matched interval pairs deduplicated by gene and interval. Descriptive cross-study agreement (same-sign fraction at 20 UMIs) and effect correlation (Spearman correlation of the mean 20- and 50-UMI effects) were summarized with 5,000 gene-block bootstrap draws (Figure 6a; Figure S13b,c; Table S5b).

Whole-gene net displacement was classified descriptively starting from strict recurrent interval genes whose deduplicated interval pairs had a uniform local sign s (the sign of ΔI averaged over both UMI layers and studies). Using primary-setting native effects from paired P–M or documented-source P–S (where local P–S used observed S and Liu2020 lacked documented-source S), genes with finite effects in both studies were classified as captured in the local direction when both $s\Delta\text{DWUI} > 0$ with $|\Delta\text{DWUI}| \geq 0.02$, same-direction subthreshold when both signed effects were positive with at least one below 0.02, and nonmatching otherwise (subdivided by whether a nonpositive signed effect reached magnitude 0.01), keeping mixed local directions and unavailable native effects separate on each workflow's measurable denominator (Table S6a).

A gene–factor relationship entered the partial-retention denominator with at least two evaluable sites and one SIC, and the numerator when the modeled family also retained a structurally constitutive site of the same factor, with 95% intervals from 4,000 gene-block bootstrap draws. Exact cross-study partial recurrence required matching coordinates and factor for both a strictly recurrent changed site and a retained constitutive site in both studies (Figure S16c,e; Table S5f), with top-gene examples per species shown as library-equal state inclusion and empirical interquartile ranges (Figure S16b,f,g).

S1.8.5. Weighted predicted-site retention

For each gene, $W_{g,t} = \sum_{i \in g} n_i \Delta I_{i,t}$ summed over atomic intervals that changed strictly in the same direction across both studies and both UMI layers ($|\Delta I| \geq 0.10$ in all four estimates), where n_i counts deduplicated complete sites of a category in interval i, $\Delta I_{i,t}$ is the two-study mean fractional change at UMI layer $t \in \{20, 50\}$, and gene signs used $W_{g,20}$ among genes with at least one complete site without requiring a matched stable window (Figure 6e; Figure S13d,e; Table S5c).

S1.8.6. Site density of changed windows

Within the sequence shared by both studies' terminal families, the union of interval boundaries defined atomic intervals. Each changed interval (defined as for W) was matched to an equal-length stable window (intervals with all four $|\Delta I| < 0.05$ plus upstream constitutive sequence) in the same gene with GC difference $\Delta\text{GC} \leq 0.05$ and relative-center distance ≤ 0.20, minimizing $\Delta\text{GC}/0.05 + \text{distance}/0.20$ with coordinate tie-breaking and control reuse allowed. Complete deduplicated hits were converted to site-density differences (sites/kb, changed minus control), averaged within and then equally across genes, and evaluated with 5,000 gene-bootstrap draws and 10,000 within-gene sign permutations (BH across the eight species–contrast–category positions, with < 10 genes descriptive). Detection power applied random signs to observed differences and added 0, 2, 5, 10 or 20 sites/kb to all or one quarter of genes (1,000 datasets per point; Figure S16d). Sensitivity blocks S5d.6 and S5d.7 (Table S5d) evaluated a 12-setting grid of GC limits (0.05,

0.10, 0.20, none) and position limits (0.20, 0.40, none; 96 direct-site and 24 transferred-site BH positions) and six random-priority backgrounds drawn from the same gene or a bipartite-matched external donor gene under unconstrained, GC-matched or GC- and position-matched rules (48 direct-site and 24 transferred-site BH positions).

S1.8.7. External miRNA expression groups

Enrichment of lost windows (all four $\Delta I \leq -0.10$) for pluripotent- versus somatic-expressed miRNA seeds (Figure S17a,b,d–f) was tested by quantifying mouse seeds in mapped reads per million from embryonic stem cell and fibroblast small-RNA sequencing (GSM307156 and GSM307157, GSE11724) [42], requiring an exact mature sequence followed by at least 6 nt of 3′ adapter starting with TCGTAT. Human seeds used the differentially expressed miRNA values of Asikainen et al. [43] (their Table S2, leaving unmapped seeds unknown). Seeds were classified as pluripotent-stem-cell (PSC) expressed at ≥ 10 and $\geq 4\times$ the somatic value, somatic under the converse rule, and neither otherwise (mouse: 105 PSC, 63 somatic and 226 other of 394 seeds; human: 43 PSC and 25 somatic of 78 mapped seeds). Barrier denotes the miR-34/449 seed (GGCAGTG) [44] and embryonic stem cell-specific cell cycle-regulating (ESCC) denotes the miR-290/302 seed (AAGTGCT) [45]. Lost-minus-control seed-site density differences (sites/kb per seed in the group) were averaged within and across genes and tested across the eight primary comparisons (two species $\times$ two contrasts $\times$ somatic minus PSC and barrier minus ESCC) by 10,000 gene-bootstrap draws and sign tests (exact for ≤ 18 nonzero genes, otherwise 50,000 permutations, BH over eight), alongside a 30-test control family covering three alternative mouse expression mappings and position-randomization nulls.

S1.8.8. Candidate RBP expression

Candidate RBPs with a shared physical site and a strict same-direction change in both studies were evaluated separately for direct and transferred factors (Table S5e). Using unique case-normalized gene symbols on the qualified library–states of Section S1.4, all-gene metacell counts were converted to $\log_2(\mathrm{CPM}+1)$, averaged within library–states and weighted equally across libraries, with P–M differences averaged over the common libraries (3, 24, 2 and 1 in Guo2019–CIP, Schiebinger2019–2i, Xing2020 and Liu2020). Following a developmental APA atlas [46], an expression flag marked candidates reaching ≥ 2 CPM in at least one qualified library–state without filtering candidates, and the transferred-motif rug of Figure 6c retained factors reaching ≥ 2 CPM in P of both mouse studies (Figure S17c,g,h).

S1.8.9. Low-net-shift screen and native-axis decomposition

Among mouse genes with primary-setting paired P–M $|\Delta\mathrm{DWUI}| < 0.02$ and MPRO ≥ 0.10 in both Guo2019–CIP and Schiebinger2019–2i (51 genes), eight also had a strict recurrent interval in both studies (Figure S14e), and of these eight, four had $|\Delta\mathrm{DWUI}| < 0.01$ in both studies, ranked by descending minimum MPRO (Figure S14b,e, Table S6b).

For the 102 gene–study records of the 51-gene screen, native PASs whose retained base lay within the common-family bounds were joined to P and M usage and contributor weights, flagging records without at least two native family PASs or nonzero family usage share. With x_i the strand-oriented distance of native PAS i from the family origin (lower bound on $+$, upper bound on $-$), L the complete native primary-axis span, $m_s = \sum_{i\in F} p_{is}$ the total terminal-family PAS usage share in state s, and μ_s the conditional family mean of x in state s,

$$\Delta\mathrm{DWUI} = \frac{\bar{m}(\mu_\mathrm{P} - \mu_\mathrm{M})}{L} + \frac{(m_\mathrm{P} - m_\mathrm{M})\bar{\mu}}{L} + \frac{\sum_{i\notin F}(p_{i\mathrm{P}} - p_{i\mathrm{M}})x_i}{L},$$

where bars denote P/M means and F is the terminal family. The within-family position term (with nucleotide shift $\mu_P - \mu_M$), the family-mass term (labeled Mass in Figure 6d and Figure S14b and Family mass in Figure S15d) and the outside-family usage term sum identically to ΔDWUI and depend on the stated origin rather than representing independent mechanisms (Figures S14 and S15). The same decomposition and common-library inclusion rules at 20 and 50 UMIs were applied to *Riok3* (Figure 6c, chosen outside the screen because its strict interval was supported under both PAS workflows) and to *Fgfr1op2* (970- and 492-nt strict intervals in polyApipe, unavailable for interval modeling in the alternative workflow; Table S6a).

S1.8.10. *Trip12* external evidence

The 842- and 706-nt strict *Trip12* intervals (GRCm39 chr1:84,701,184–84,702,026 and chr1:84,700,478–84,701,184, minus strand) and their 68 predicted miRNA sites were mapped to archive assemblies by unique, gap-free reciprocal liftOver (Figure S15e, Supplementary Table S6c). In GSE282319 filtered long-read transcript models and IsoQuant abundances [47], compatible isoform pairs shared an identical intron chain and terminal-exon anchor while retaining versus completely excluding the interval. In GSE25310 AGO2 HITS-CLIP tracks [48], same-strand overlaps of at least 1 bp were tallied separately for individual wild-type libraries (WT1A, WT1B and WT2) and merged wild-type or Dicer-knockout tracks as descriptive compatibility checks.

S1.8.11. Upstream UGUA content

Paired P–M 0.02 recurrent genes (proximal, distal or not recurrent) with a single-terminal-UTR primary PAS axis, cross-study transcript compatibility and complete 100-nt upstream sequences at the most proximal and most distal reference-supported PAS anchors were scored from the reference genome FASTA for distal-minus-proximal TGTA (UGUA) counts in $[-100, -40)$ nt, with $[-100, 0)$ and $[-80, -40)$ nt windows and TGAT/CGTA motifs as controls. Proximal responders were compared against nonrecurrent and distal responders on the 52 jointly eligible one-to-one orthologs and on each species' strict tandem-3′ UTR background under 20,000 permutations stratified by the L3 assay/capacity covariates of Section S1.6 plus PAS spacing, GC content and core hexamer, with BH over the eight primary and 208 exploratory tests (Figure S18d; Table S7c).

S1.9. Cross-species comparisons

S1.9.1. Ortholog universe and node effects

Cross-species analyses used the 16,092 Ensembl release 116 high-confidence one-to-one ortholog pairs (BioMart, 1 August 2026 [17,18]). Study-specific PAS axes leave homologous PASs unaligned except in the homologous-PAS analysis below. Node-based effects (R–S, E–S, P–S and M–S, each relative to the observed-S node of the route) followed the catalog and route PAS-support rules of Section S1.4 (requiring a reference-supported catalog of ≥ 2 sites spanning ≥ 200 nt) and required at least ten qualified metacells in both states. Paired P–M effects were computed within libraries and aggregated across sampling units and dates as in Section S1.4, requiring at least two qualified sampling units in each mouse study and one in each contributing human study.

S1.9.2. Continuous correspondence

Spearman correlations between human and mouse node effects were calculated on the orthologs measurable in both species for every study pair in which both species had the state, giving four pairs each for R–S and E–S and eight each for P–S and M–S (24 study-pair × contrast combinations; Figure S9d). State summaries averaged the pairs equally. Uncertainty came from 1,000 ortholog-block bootstrap draws of the ortholog

union, applying one resample (and thus each gene's multiplicity) to all pairs of a state, with per-pair intervals using the same draws restricted to that pair's genes.

S1.9.3. Documented-source study-pair sharing

Sharing used documented-source P–S effects on all jointly measurable orthologs, independently of recurrence, for the four pairs of Xing2020 or Guan2022 with Guo2019–CIP or Schiebinger2019–2i. Signed labels were -1, $+1$ or 0 (requiring all Guan2022 series to agree) at thresholds of 0.02 and 0.05 for DWUI and RWUI and 0.10 and 0.20 for unsigned MPRO, with same-direction sharing summing shared proximal and shared distal events. Each species' labels were shuffled independently (10,000 permutations, $P = (1 + \#\{\text{null} \geq \text{observed}\})/10{,}001$, with seed 20261003 plus a configuration hash) under the Q5 signed strata (measurable study/series count, terciles of expression, APA coverage and PAS number, median source-DWUI quintile and source-dependent directional capacity) and metric-specific MPRO strata of Section S1.6. Expected counts were computed analytically from within-stratum label probabilities and verified against permutation means. The 24 sharing tests across DWUI, RWUI and MPRO (same-direction sharing for DWUI and RWUI, unsigned sharing for MPRO) formed the primary reporting family (q_{24}), with eight-test per-metric and 56-test signed-component families in Table S4a.

Direction differences were tested in a separate 80-test family sharing no hypothesis with the sharing family (Figure S9c; Table S4a). For DWUI and RWUI at 0.02 and 0.05, 48 synchronized tests comprised, for each metric and threshold, four pair tests, one pooled test giving each of the 3,246 unique orthologs equal total weight split over its pairs, and one between-pair heterogeneity test, each evaluated for the absolute estimand $[(O_{\text{distal}} - E_{\text{distal}}) - (O_{\text{proximal}} - E_{\text{proximal}})]/n$ and the relative estimand $\log[(O_{\text{distal}} + 0.5)/(E_{\text{distal}} + 0.5)] - \log[(O_{\text{proximal}} + 0.5)/(E_{\text{proximal}} + 0.5)]$. Their null shuffled each species' complete two-study label vector intact within the intersection of all study-pair Q5 strata and the eligibility pattern independently between species (10,000 draws), keeping a study's gene label identical across pairs containing it. A further 32 pair-specific tests reused the per-pair sharing null draws, with differences tested two-sided and heterogeneity upper-tailed.

S1.9.4. Shared proximal candidates

A gene was a shared proximal candidate when it had a proximal effect of at least 0.02 ($\Delta\text{DWUI} \leq -0.02$) in both Schiebinger2019–2i and Guo2019–CIP and in at least two of the four human studies, with no human study at $+0.02$ or higher, using observed-S node effects for P–S (Guan2022–0618 for Guan2022) and paired effects for P–M. Overlap between the species' proximal sets was tested in the 16,092-pair universe, keeping unmeasured pairs in their own strata stratified by each species' number of studies with a measurable effect so that genes unable to qualify received no events while remaining in the universe, under three nulls (Figure S9a; Table S4b). The joint measurement–PAS null stratified orthologs by the number of studies with a measurable node and the median supported-PAS count in each species and drew within-stratum overlaps from the hypergeometric distribution (5,000 draws). This joint null was also repeated across a 16-test grid at $|\Delta\text{DWUI}| \geq 0.01$, 0.02, 0.03 and 0.05 in both PAS layers. The two reference-capacity nulls shuffled each species' labels independently (20,000 permutations; BH q_2 per null) within common base strata combining measurable-study counts, median supported-PAS terciles and proximal capacity (number of reference nodes with DWUI ≥ 0.02, using observed S for P–S and M for P–M), adding either the quintile of median reference DWUI (Quintile null) or separate 0.1-wide bins of minimum and maximum reference DWUI (Range null).

A sensitivity analysis added species-level gene expression (pooled CPM) and APA coverage (PAS UMIs per qualified metacell) terciles to both reference-capacity nulls on the

16,092-pair universe at the primary 0.02 threshold. Reconstructed from the gene-qualified metacells with the endpoint weights of Section S1.4, averaged equally across target and reference states and summarized by the median across measurable studies, both covariates were cut into terciles on all measurable background genes within each species and contrast (keeping ties together and unmeasured genes in missing-value strata) and appended to the Quintile and Range strata without redefining them (20,000 permutations per model and contrast; BH q_2 and q_4). Raw and $\log_2(1+x)$ covariate balance, minimum endpoint and library coverage, label mobility, fixed overlap, null variability, and conditional calibration and power across 3,000 simulated datasets at overlap odds ratios of 1, 2 and 4 were evaluated under the same strata (Table S4b). Power curves (Figure S9f) shuffled human labels within the Quintile strata, drew mouse overlaps from a Fisher noncentral hypergeometric distribution at odds ratios 1, 2, 4 and 8 preserving all margins (3,000 datasets each), and tested each dataset against the 20,000-draw L1 and L3 nulls of Section S1.6 at $\alpha = 0.05$ with exact binomial intervals.

S1.9.5. Direction pairing of recurrent orthologs

Direction pairing (Figures 3a–c and S10; Tables S4f and S4g) started from the fixed within-species recurrence calls (proximal, distal or not recurrent) on the one-to-one orthologs measurable in at least two studies of each species (1,656 pairs for P–S and 751 for P–M, excluding unmeasured pairs), unlike the shared proximal candidates tested on the full 16,092-pair universe above. Labels were permuted independently in each species within strata preserving the three label counts per stratum under two models. The measurement-and-PAS-capacity model crossed the exact measurable study/series combination with PAS-number terciles and threshold-updated counts of studies whose native reference left room for a proximal or distal shift. The full-assay model added terciles of median expression and APA coverage and quintiles of median reference DWUI, with quantile bins formed once on each contrast's common ortholog inventory. Analytic conditional expectations of the 3×3 cells and one-sided upper-tail P values were evaluated with $N = 10{,}000$ permutations at 0.02 and 100,000 per threshold in the scan (seed 20261003 plus 12-hex SHA-256 hash). Event-class analyses restricted foreground and background to pairs classed alike in both species while keeping the 751-pair strata without rebinning (100,000 permutations). Strata with immobile labels were reported rather than merged, and under the full-assay model every human label of the alternative-last-exon (ALE)-compatible class lay in such a stratum, so that test cannot exclude a shared ALE response.

S1.9.6. Naive specificity of the shared proximal response

For the human naive-related state (hN), the two Liu2020 naive conditions (N6 and N8) were each compared with primed P7 and averaged with equal weights because they represent distinct culture conditions rather than replicates. Mouse target sets were the proximal P–M recurrent genes and their subset also proximal in P–S across the same contributing studies. Human controls were primed P–S against source-like cells of another library (P7–S5), within-library primed P–S, M–S, E–S and P–M in Liu2020 (P7–S7, M7–S7, E7–S7 and P7–M7), and the multi-study human P–S and P–M recurrent sets. On the common one-to-one background measurable for all contrasts of each comparison, human and mouse response labels were permuted within strata preserving joint response patterns and directional capacity (20,000 permutations) across a coarse tercile model (primary) and a fine model (reference quintiles and mouse expression terciles), each with and without human pseudobulk mean $\log_2(\mathrm{CPM}+1)$ terciles. The statistic $O_{\mathrm{naive}}/E_{\mathrm{naive}} - O_{\mathrm{control}}/E_{\mathrm{control}}$ used exact null expectations with one-sided BH correction over the 14 planned compar-

isons at 0.02 (primary) and 0.05 (sensitivity) and over four mismatched-direction negative controls (Figure S12; Table S4i).

S1.9.7. Homologous PASs

Native PASs were summed by 50-nt integrated-reference identity (Section S1.8), and human GRCh38 and mouse GRCm39 identity cuts were mapped in both directions with UCSC `liftOver -multiple -minMatch=1` (`hg38ToMm39` and `mm39ToHg38`) as strand-oriented 1-nt intervals ($[c-1, c)$ on $+$, $[c, c+1)$ on $-$), excluding unmapped, multi-hit, or non-single-nucleotide mappings. Within one-to-one ortholog partners on the mapped chromosome and strand, a deterministic greedy one-to-one assignment performed once before tolerance filtering prioritized reciprocal 25-nt matches (primary), reciprocal 50-nt matches (sensitivity), smaller forward and reverse differences, and annotation identifiers, rather than a global maximum matching or mutual-nearest-neighbor rule.

Each gene and study pair required at least two matched PASs with strictly increasing transcript-oriented order in both species (excluding crossing orders) and a matched usage share of at least 0.8 in every state of both species before renormalizing matched-state vectors. The P/M/S cohort (Xing2020 with Guo2019–CIP and Schiebinger2019–2i) used the common P/M/S contributors and weights of Section S1.6, and the P/E/M control (Liu2020 with Guo2019–CIP) used libraries with qualified P, E, and M and at least two jointly count-supported PASs for both P–M and E–M, weighting dates, sampling units, and libraries equally. For K ordered sites, state positions were inner products of renormalized usage with rank weights $(i-1)/(K-1)$ or distance weights $(x_i - x_1)/(x_K - x_1)$ computed separately in each species, so P–M equaled P–S minus M–S identically, and study pairs entered correlations only with at least ten eligible genes.

Spearman correlations and paired correlation differences on the same genes (taking the arithmetic mean of the two Xing2020 pairs in P/M/S) were summarized with 3,000 ortholog-block bootstrap draws applying identical gene multiplicities across pairs to compute weighted midrank correlations conditional on the measured genes and fixed study pairs. On the 25-nt rank axis, two conditional nulls shuffled each mouse ortholog's complete contrast vector within strata with human values fixed (5,000 permutations; seeds 20261008 and 20261009): coarse strata combined study-pair availability, median matched-site count (< 3 vs ≥ 3), and minimum matched usage share (< 0.9 vs ≥ 0.9), and capacity strata additionally split the mean matched-rank reference position at 0.5 for S and M in P/M/S and M in P/E/M. BH covered eight one-sided rank-axis tests per null (q_8: P–S, M–S, P–M, P–M minus P–S, and P–M minus M–S in P/M/S; P–M, E–M, and P–M minus E–M in P/E/M), with a separate coarse q_8 family at 50 nt and bootstrap intervals only on the native and distance axes (Figure S11; Table S4c).

For *PDLIM7/Pdlim7*, versioned Ensembl release 116 exon and coding-sequence records verified coding lengths of 669 and 1,374 nt including the stop codon (predicted 222- and 457-amino-acid products) for the human and mouse transcripts ending at the proximal and distal matched PASs (separated by 6,852 nt in human and 8,360 nt in mouse; transcript accessions and coordinates in Figure S11f,g and Supplementary Table S4d). In mouse, the proximal matched PAS ends the alternative-terminal-exon transcript encoding the 222-amino-acid LIM-domain-truncated isoform, whereas the distal matched PAS lies 235 nt downstream of the stop codon within the terminal 3′ UTR of the full-length coding transcript, retaining the complete 457-amino-acid coding sequence despite an overlapping retained-intron primary-transcript tag. Per-study native ΔDWUI values of the gene are shown in Figure 4a.

S1.9.8. Cis-feature models

On one-to-one orthologs with a measurable P–S or paired P–M effect in at least two studies per species, a gene was active in the discovery species when at least one study reached $|\Delta\text{DWUI}| \geq \tau$ (direction defined by the nonzero discovery median), and the binary outcome was a predicted-species median effect of at least τ in that direction. In the discovery species, the annotation-mapped PASs with the largest mean P-minus-reference gain and loss formed the switching PAS pair (ties broken by lexicographic identifier), defining five cis predictors from the 25-nt homologous-PAS matching: matched switching-PAS count (0–2), matched fraction of discovery PASs, architecture score $A_g = 2 \times \text{matched PASs}/(\text{human} + \text{mouse PASs})$, mean phastCons score from the UCSC mm10 60-way track [28,49] over $[\text{cut} - 100, \text{cut} + 50)$ after liftOver to mm10, and best upstream hexamer rank (AATAAA 3; ATTAAA, AGTAAA, AATACA, AATATA, CATAAA, and TATAAA 2; AAGAAA, AATAAT, AACAAA, AATAGA, AATGAA, and GATAAA 1; otherwise 0) in $[-35, -9]$ nt.

Firth-penalized logistic models [50] were fitted for each layer, contrast, discovery species and $\tau \in \{0.01, 0.02, 0.03, 0.05\}$ with median-imputed, standardized predictors (dropping constant study-count predictors): M0 (absolute discovery effect, eligible study counts in both species and discovery PAS count), M1 (adding discovery supporting-study fraction), and separate expansions of M1 adding the two homology predictors (PAS), A_g (Architecture), phastCons and motif rank (Sequence), or all five predictors (All cis), so model gains are not additive. The joint cis test compared All cis against M1 by a 5-df likelihood-ratio statistic referred to 4,999 conditional parametric bootstrap outcome vectors simulated from the restricted fit (q_4 primary reporting family on the reference-supported layer at $\tau = 0.02$; 32-setting sensitivity family). Out-of-fold prediction used ten class-stratified five-fold partitions (seeds 2200–2209) shared across models with training-only imputation and scaling, summarizing mean within-repeat paired AUC gain and log-loss reduction (where AUC is the area under the receiver operating characteristic curve) with 2,000 gene-bootstrap draws and penalized-likelihood profile 95% intervals for coefficients (Table S4e).

S1.9.9. Candidate mechanisms for the shared proximal set

Post hoc mechanism checks compared the 27-ortholog shared proximal set against matched expectations within each measurable background (Figure S19c–e; Table S7f). Sequence and perturbation tests evaluated three candidate mechanisms. First, selective decay of long isoforms was tested by scanning 67 distal regions complete in both species for 7-mer or 8-mer sites of the ESCC miRNA seed AAGUGCU (miR-302/372/294) and U-rich elements under length and GC matching (BH over 18 tests). Second, exit from the mesenchymal program was tested across 605 genes measured in external QKI-knockdown proximal and epithelial–mesenchymal transition (EMT) distal target tables [51] (BH over 36 tests). Third, U1-dependent PAS choice was evaluated descriptively across 10 shared proximal versus 176 other measurable genes shifting proximally under U1 inhibition and distally under U1 overexpression in pooled external tracks (GSE140543 [52]) at $|\log_2 \text{ratio}| \geq 0$, 0.2 and 0.5, together with assay-matched tests of PAS anchor architecture for the shared proximal set (proximal PAS rank, rank difference and log anchor span; BH over 12 tests). Functional checks evaluated membrane-system deployment across four GO categories under joint measurement and PAS-capacity matching on the 751 P–M pairs (BH over 16 tests) and an external endoplasmic-reticulum distribution proxy (BH over four tests), together with three RNA-regulation GO categories tested among the 48 orthologs with same-direction responses in both species in P–S or P–M (Table S4j).

S1.10. Alternative PAS calling workflow

Dependence of the conclusions on PAS calling was tested by re-calling PASs from the same Cell Ranger alignments with an in-house workflow (apaDetect v0.4.1, with v0.3.0 used for detection in 32 libraries; code included in the archived analysis repository of the main-text Data Availability Statement) and building a second count matrix in six steps.

(1) Discovery. Across all 210 libraries of the seven studies (including the 49 discovery-only libraries), strand-specific read-end coverage was smoothed with a triangular kernel of the sample read length, and candidate PASs were called at derivative changes on covered islands. Candidates with a same-strand splice donor at $-10 \leq (\text{donor} - \text{PAS}) \times \text{strand} \leq 100$ nt were removed using donors supported by at least 20 split reads with 70–500,000-nt introns and $\geq$ 8-nt anchors.

(2) Localization. Within each positive-coverage component, a single candidate was placed by a half-read-length correction or at a supported boundary read-end cluster. In multi-candidate components, the most downstream candidate was retained, and each upstream candidate was retained when it lay more than two read lengths upstream of the next retained candidate, when the intervening smoothed valley was at most half the lower peak, or when cell-barcode and UMI evidence separated them, followed by a second splice-donor check.

(3) Study catalog. Within each study, calls on the same chromosome and strand were merged when adjacent sites lay within 25 nt and the cluster spanned at most 50 nt, taking the integer midpoint as the representative coordinate and rechecking against the study union of passing splice donors.

(4) Counting. Count windows were constructed from the median left and right offsets of member windows, split at midpoints between neighboring sites (retaining empty-window sites as non-quantifiable), and recounted across every atlas library using corrected cell barcodes and UMIs on the full expression-atlas barcode axis.

(5) Internal-priming filter. Within annotated gene spans, same-strand genomic A-rich stretches ($\geq$ 10 nt of A with at most one interruption) were extended 500 nt upstream and 20 nt downstream of the stretch start, removing sites whose representative coordinate fell within the mask after counting.

(6) Terminal protection. Masked sites without cross-gene ambiguity or unknown sequence were retained when they lay within 50 nt of the nearest annotated transcript 3′ end of the same gene (within the terminal exon or up to 50 nt downstream) and the 20 nt downstream of both the site and the annotated end had an A fraction below 0.8 and no run of $\geq$ 8 A, selecting rows of the fixed count matrix without reassigning UMIs.

The resulting count matrix underwent the same gene assignment, primary-site rules, integrated-reference support, metacell aggregation, hierarchical weighting, and L3 stratified permutation tests as the polyApipe counts (Sections S1.4 and S1.6), holding expression states, quality-controlled barcodes, and metacell memberships fixed while rebuilding workflow-specific eligibility, candidates, backgrounds, and effects. Comparisons with polyApipe summarized outputs on common measurable backgrounds without averaging inputs or adding differential tests, assessing computational robustness rather than independent replication (Figure S21; Table S9a). Classifications of local change relative to whole-gene net displacement (Table S6a) and cycle-adjustment feasibility diagnostics against fixed primary candidate sets (Table S7g, sharing the GEX-based cycle-score tests) were evaluated on each workflow's eligible background, and *Fgfr1op2* lacked an evaluable alternative interval model and was recorded as unavailable. Each polyApipe strict recurrent interval pair was mapped to the alternative coordinate region of the same route, gene, and contrast containing its 3′-most base and classified as reproduced (both studies strictly changing in the polyApipe direction), below threshold (measured with the same direction

or no change, not strict in both), conflicting (opposite-direction change in either study), or not measurable (subdivided into absent alternative interval model versus outside the alternative terminal family or lacking an eligible effect; Table S9b).

S1.11. Ortholog attrition and candidate-level retention

S1.11.1. Retained and excluded one-to-one orthologs

All 16,092 high-confidence one-to-one human–mouse ortholog pairs of Ensembl release 116 were traced descriptively through the primary-setting eligibility funnel (reference-supported primary PAS layer, purity $\geq$ 0.8, Section S1.4, Table 1 of the main text, Figure S24a–f). A gene was measurable in a study when at least one planned library pair passed all gene-level eligibility rules across the contributing studies: Xing2020 and Guan2022 (series 0618 and 0809 combined) in human and Guo2019–CIP and Schiebinger2019–2i in mouse for documented-source P–S, and Xing2020, Liu2020 and Panariello2023 in human with the same two mouse studies for paired P–M (excluding Jaber2022, which lacked P). Direction pairing retained pairs measurable in at least two studies per species (1,656 retained vs 14,436 excluded in P–S; 751 vs 15,341 in P–M), partitioning the 16,092 pairs into retained in both species, measurable in fewer than two human studies only, measurable in fewer than two mouse studies only, and measurable in fewer than two studies in both species.

Within each contrast and species separately, the 16,092 orthologs were partitioned into five mutually exclusive categories summing to 16,092 according to the furthest sequential eligibility stage reached across relevant studies: retained ($\geq$ 2 measurable studies), or exited at stage (1) primary catalog requirement (no primary PAS catalog in any relevant study), (2) axis and retained-PAS requirement (primary catalog in $\geq$ 1 study, but no study with $\geq$ 2 primary PASs on one chromosome and strand and $\geq$ 2 reference-supported retained PASs), (3) library-pair measurement requirement (passing stage 2 in $\geq$ 1 study, but no library pair passing all sub-steps, summarized in order of gene-qualified metacells, $\geq$ 30 cells, and $\geq$ 2 jointly count-supported PASs), or (4) study-count requirement (measurable in exactly one study). Because genes can fail at different stages across studies, this partition summarizes sequential filter exit rather than independent biological causes.

Retained and excluded orthologs (1,656 vs 14,436 in P–S; 751 vs 15,341 in P–M) were compared descriptively across five features without hypothesis tests. First, design-wide gene expression was computed from integer gene-by-metacell count matrices across all purity-$\geq$ 0.8 metacells $A_{r\ell s}$ of each state group in the fixed endpoint library pairs (P and documented S for P–S; co-captured P and M for P–M; $\geq$ 3 metacells and $\geq$ 30 cells per state, without a gene-level PAS UMI depth filter) as

$$E_{gr\ell s} = 10^6 \times \frac{\sum_{m \in A_{r\ell s}} C_{gm}}{\sum_{m \in A_{r\ell s}} T_m},$$

where C_{gm} is the UMI count of gene g in metacell m and T_m is the all-gene UMI total in m. Equal-weight state means within library pairs were aggregated to routes using the fixed endpoint weights (Section S1.4) and summarized by the route median within each study and the study median per species, keeping zero counts as zero and recording genes absent from expression tables (401 human and 425 mouse genes) as unavailable. Second and third, primary catalog PAS count and reference-supported retained PAS count were summarized per species by the median across relevant studies (0 where absent). Fourth, longest annotated terminal 3′ UTR length (nt) was extracted across Ensembl release 116 coding transcripts (GRCh38.116 and GRCm39.116) as the maximum 1-based closed interval length downstream of a terminal-exon stop codon (unavailable for 637 human and 694 mouse genes lacking such a transcript). Fifth, single-terminal-3′-UTR axis containment was the fraction of usable study–gene primary axes ($\geq$ 2 primary PASs on one chromosome

and strand) with a qualifying terminal-UTR annotation whose primary PAS retained-nucleotide positions all fell within one annotated terminal 3′ UTR. Continuous features were summarized by linear-interpolated quartiles (Q1, median, Q3) and the standardized mean difference SMD $= (\bar{x}_{\text{retained}} - \bar{x}_{\text{excluded}}) / \sqrt{(s^2_{\text{retained}} + s^2_{\text{excluded}})/2}$ using sample standard deviations s on $\log_2(1 + \text{CPM})$ for expression and native units otherwise.

S1.11.2. Candidate-level retention and descriptive prioritization

Recurrence, structural and expression records were compiled descriptively in Table S10c for 44 unique ortholog–contrast entries (43 unique one-to-one ortholog pairs), comprising the 27 shared proximal P–M pairs (Table S4g), the 14 shared distal P–S pairs (Table S4f) and three additional focal entries (*PDLIM7*/*Pdlim7* in P–S, *FGFR1OP2*/*Fgfr1op2* in P–M and *RIOK3*/*Riok3* in P–M, with shared example roles noted on the merged row). Each entry was evaluated at $|\Delta\text{DWUI}| \geq 0.02$ and ≥ 0.05 across three separately checked conditions: (i) the primary polyApipe v0.1.0 workflow with cluster-defined M, including the number of thresholds (of nine from 0.010 to 0.050, Table S4g; not applicable for *RIOK3*/*Riok3*) with same-direction sharing, (ii) the alternative PAS-calling workflow (apaDetect v0.4.1, Section S1.10, Table S9a) with cluster-defined M, and (iii) marker-defined human M (human M*, Section S1.4, Table S10b, on the 728-pair common P–M background; not applicable for P–S). Under each condition and threshold, each species was coded as proximal recurrent, distal recurrent, measurable in ≥ 2 studies but nonrecurrent, measurable in < 2 studies, outside the fixed background, or not applicable.

Entries were ranked descriptively by five criteria (Table S10c). Criterion 1 required same-direction cross-species recurrence at $|\Delta\text{DWUI}| \geq 0.02$ in the primary workflow (leaving non-shared focal examples unranked). Criterion 2 required retention of same-direction recurrence in both species at 0.02 across all applicable sensitivity conditions (alternative PAS calling and human M* for P–M; alternative PAS calling for P–S). Criterion 3 recorded an annotated or sequence-predicted structural consequence (alternative last exon in Table S4g, coding truncation in Table S4d, bilateral tandem-3′ UTR shortening in Table S4g, exact cross-study partial recurrence of a canonical miRNA seed site in a remodeled interval in Table S5f, or a reciprocal 25-nt homologous PAS switch in Table S4h). Criterion 4 recorded design-wide expression (CPM and percentile within the 1,656 P–S or 751 P–M retained background, flagging pairs $\geq$ 25th percentile in both species), and Criterion 5 recorded the number of primary thresholds (of nine, 0.010–0.050) with same-direction sharing alongside all-condition retention at $|\Delta\text{DWUI}| \geq 0.05$. Entries passing Criteria 1–3 formed Tier 1, those passing Criteria 1–2 without Criterion 3 formed Tier 2, and those passing Criterion 1 but not Criterion 2 formed Tier 3 (ranking losses of evaluability due to background or study-count requirements ahead of lost recurrence). Within tiers, entries were ordered by all-condition retention at 0.05, Criterion 5, and the lower species expression percentile (Criterion 4). Lower-cycle-half P recurrence at 0.02 and within-P difference D (Section S1.7) were appended to P–M entries for reference.

S1.12. Route, sampling-date and state-reference sensitivities

S1.12.1. Restriction to the latest eligible P sampling date

Endpoint-date sensitivity (Table 1 of the main text) was evaluated by restricting each documented-source P–S route from the primary polyApipe v0.1.0 workflow to its latest eligible pluripotency-acquisition (P) sampling date (Figure S22b–d). In Guo2019–CIP, D32 (13 P metacells, 360 cells) and D36 (31 P metacells, 1,635 cells) were excluded, retaining only the D40 P library (GSM3619581, 41 P metacells, 1,480 cells) paired with the D0 documented-source S library (GSM3619570, 79 S metacells, 3,919 cells). In Schiebinger2019–2i, 12 earlier sampling dates (D12–D17.5, 22 libraries across 44 physical target–source pairs) were

excluded, retaining only the two D18 P libraries (GSM3195766 with 29 P metacells and 1,566 cells; GSM3195767 with 23 P metacells and 1,241 cells) paired with the two D0 documented-source S libraries (GSM3195648 with 64 S metacells and 3,160 cells; GSM3195649 with 20 S metacells and 987 cells) across four physical target–source pairs. Each of the three human series had a single P sampling date in the primary design (D16 in Xing2020 with two P libraries of 6 and 40 metacells against one D0 S library of 130 metacells; one endpoint P library each in Guan2022–0618 and Guan2022–0809 with 145 and 81 P metacells against two and one documented-source S libraries), so human library pairs and gene-level ΔDWUI values were unchanged. Because human series had one P date whereas mouse P spanned 3 dates in Guo2019–CIP and 13 in Schiebinger2019–2i, no per-gene latest-date rule or kinetic window matching was applied, and paired P–M was not date-restricted.

Route-level target and reference DWUI, ΔDWUI (P minus S), pooled gene expression (CPM), APA coverage and gene-level eligibility were reconstructed from the date-restricted library pairs using the hierarchical weights and the 16 combinations of four measurement settings and four gene backgrounds defined in Section S1.4. Both gene backgrounds recomputed on the date-restricted data and the original gene backgrounds (intersected with genes measurable in the restricted route and setting) were evaluated. For each of the six human–mouse series pairs, the human-minus-mouse difference in route mean ΔDWUI ($\bar{\Delta}_{hc} - \bar{\Delta}_{mc}$) was classified as strictly preserved when all 16 setting-by-background differences were finite and positive.

Within-species mouse P–S recurrence after date restriction was tested at $|\Delta\text{DWUI}| \geq 0.02$ and ≥ 0.05 on the primary setting (3,736 genes measurable in ≥ 1 mouse study, 2,077 in both) against 10,000 permutations of the L3 conditional null reconstructed from the date-restricted covariates (Section S1.6; base seed 20261104 fixed before computing restricted statistics; BH q_2). The 604 (at 0.02) and 265 (at 0.05) unrestricted mouse P–S recurrent genes were classified into retained same-direction recurrence, measurable in both studies but nonrecurrent, measurable in fewer than two studies, or opposite-direction recurrent. Cross-species P–S direction pairing at $|\Delta\text{DWUI}| \geq 0.02$ crossed the unchanged human labels with the date-restricted mouse labels on the 1,410 one-to-one ortholog pairs measurable in ≥ 2 studies per species under the full-assay conditional permutation null (10,000 permutations with quantile strata recomputed on the 1,410-pair inventory; BH q_4).

S1.12.2. Fibroblast-derived series

A subset analysis evaluated whether the relative ordering of human and mouse route means held when restricted to fibroblast-derived series across the 16 combinations of four measurement settings and four original gene backgrounds (Section S1.4, kept without recomputation; Figure S22a). In paired P–M, all five series derived from fibroblasts (Xing2020 BJ neonatal foreskin fibroblasts, Liu2020 fibroblasts and Panariello2023 fibroblasts in human; Guo2019–CIP and Schiebinger2019–2i mouse embryonic fibroblasts in mouse), forming six human–mouse series pairs (96 matched scenario comparisons). In documented-source P–S, excluding adipose-derived Guan2022 and chemically induced Guo2019–CIP left one fibroblast-derived, transcription-factor-induced human–mouse pair (Xing2020 vs Schiebinger2019–2i, 16 matched scenario comparisons), which was summarized descriptively without multi-series inference by each series' 16-scenario equal-weight mean, minimum and maximum, the matched differences $\bar{\Delta}_{hc} - \bar{\Delta}_{mc}$, and whether the human 16-scenario minimum exceeded the mouse 16-scenario maximum.

S1.12.3. Naive-related endpoint reference check

Unfiltered (252 metacells) and quality-selected (213 metacells) state annotations of all four Liu2020 libraries, namely S5 (GSM4546545), N6 (GSM4546546), P7 (GSM4546547),

and N8 (GSM4546548), were inspected across the four measurement settings and four gene backgrounds (32 planned contrasts for N6 and N8; Figure S22e). Because N6 and N8 contained zero M metacells in the unfiltered metadata, same-library hN–M contrasts were recorded as unavailable without borrowing M from S5 or P7 or substituting S for M. Existing Liu2020 naive-versus-primed ΔDWUI estimates were retrieved from the primary tables alongside their distinct estimands and gene backgrounds: cross-library N6 hN minus P7 P and N8 hN minus P7 P on available genes, and same-library hN–P within RSeT library N8 (GSM4546548) on genes measurable across all three edges of the hN–P–S triangle (Section S1.4).

S1.12.4. Response correspondence across R, E and M states

Because Guo2019–OSK and the two day-3 captures of Jaber2022 lack a sampled P state and cannot enter P–S or P–M endpoint comparisons, gene-level response correspondence was evaluated descriptively across sampled R, E and M states (Figure S23a–e) using the primary observed-S estimator of Section S1.4 ($\geq$ 20 PAS UMIs per metacell, 30-cell group gate and $\geq$ 20 measurable genes per pair). For each route r, state family $s \in \{\mathrm{R}, \mathrm{E}, \mathrm{M}\}$ and gene g, the state effect $d(r, s, g)$ was the equal-weight library mean DWUI in state s minus that of the route's observed source-like (S) reference. Across the three multi-day mouse routes (Guo2019–OSK, Guo2019–CIP and Schiebinger2019–2i), pairwise Spearman rank correlations (ρ, Pearson correlation of midranks) and directional threshold counts at $|\Delta\mathrm{DWUI}| \geq 0.02$ (same-direction $|A_+ \cap B_+| + |A_- \cap B_-|$ and opposite-direction $|A_+ \cap B_-| + |A_- \cap B_+|$ alongside marginal expectations $E_{\mathrm{same}} = (n_{a+}n_{b+} + n_{a-}n_{b-})/N_{ab}$ and $E_{\mathrm{opp}} = (n_{a+}n_{b-} + n_{a-}n_{b+})/N_{ab}$ over the N_{ab} jointly measurable genes) were recorded without prefiltering. Within-study cross-protocol versus cross-study transcription-factor correspondence was summarized on each state's three-route measurable intersection (3,576 genes in R, 3,327 in E and 1,288 in M) by $\Delta\rho = \rho(\mathrm{Guo2019–OSK}, \mathrm{Guo2019–CIP}) - \rho(\mathrm{Guo2019–OSK}, \mathrm{Schiebinger2019–2i})$ with conditional 95% intervals (2.5th and 97.5th percentiles) from 2,000 gene-bootstrap draws (PCG64 seed 20261106) resampled simultaneously across all three routes. In Jaber2022, day-3 GETM (GSM6071749) and OSKM (GSM6071750) M–S ΔDWUI vectors were compared descriptively across their 882 jointly measurable genes by Spearman ρ and $|\Delta\mathrm{DWUI}| \geq 0.02$ directional counts.

S1.13. Statistical conventions, display summaries and reproducibility

S1.13.1. Statistical conventions

The hierarchy of primary, secondary, and post hoc analyses, the unit-of-inference rules, and the catalog of revision sensitivity analyses (marked † in the Supplementary Tables and detailed in Sections S1.7, S1.11, and S1.12) follow Main Materials and Methods Section 4.10 and Table 1. Across the supplement, upper-tail empirical permutation P values were computed as

$$P_{\mathrm{emp}} = \frac{1 + \sum_{b=1}^{B} \mathbf{1}(T_b \geq T_{\mathrm{obs}})}{B + 1},$$

with the inequality reversed for depletion and two-sided forms stated where used ($1/10{,}001 \approx 1.0 \times 10^{-4}$ for $B = 10{,}000$). Benjamini–Hochberg (BH) adjusted P values [30] are denoted q with subscripts indicating family size (q_2, q_4, q_8, q_{16}, q_{20}, q_{24}, q_{72}), and separate families are not directly comparable. Across Supplementary Tables S1–S10, columns `ci_low` and `ci_high` report the lower and upper bounds of the stated bootstrap, permutation, or exact interval for each row's estimator. Within-study resampling intervals over cells, metacells, libraries, sites, or cross-validation repeats quantify measurement resolution rather than study-level biological replication. Undefined, infeasible, or insufficient-denominator

quantities are recorded as `unavailable` rather than recoded as zero or $P = 1$ (except where single-study positions enter a fixed-size multiple-testing family as $P = 1$, Section S1.6).

S1.13.2. Display summaries

Ranges across measurement settings, source choices and libraries describe sensitivity rather than sampling confidence. Bootstrap intervals specify the resampled unit (genes, metacells or wells), and central permutation ranges show null variation. The *PDLIM7/Pdlim7* panels use matched contributors with panel-specific PAS representations, whereas for *Eif4ebp2*, *Snx30* and *SH3PXD2A* (Figure S16b; Table S5f) plots display separate-state library-equal means while paired P–M estimates use common libraries.

S1.13.3. Source data and reproducibility

Stochastic analyses used deterministic seeds derived from the test key (base seed 20261003, or 20261104–20261106 for revision analyses, plus the first 12 hexadecimal digits of the SHA-256 hash of the test identity) so each test can be rerun independently. Supplementary Tables S1–S10 are provided as one workbook (Section S4, where `WPP` columns denote DWUI) whose Sources sheet records the source file, row filter and SHA-256 hash of every block, while the Zenodo releases (v12-r1 and v11f, main-text Data Availability Statement) supply the pair-effect and PAS-axis tables, revision source tables, analysis code, configurations and seeds, with native per-study PAS count matrices and frozen gene-expression matrices retained by the authors as cataloged in `Revision_Inputs.tsv`.

S2. Supplementary results

S2.1. Expression states, PAS measurement and the global APA direction

State framework. Most local expression states were stable across neighboring resolutions and seeds, with three boundary states retained with qualifications (Figures S1, S2 and S3, Table S1a). Best-match Jaccard index J fell below 0.80 for 23/62 human and 8/49 mouse states, and display-family compatibility F fell below 0.80 for nine and four. Small Guan2022, Liu2020 and Panariello2023 states were least stable (lowest $J = 0.205$, Guan2022 C011), whereas Guo2019–CIP states had $J \geq 0.975$ except for keratin-related C005 ($J = 0.902$). Median unit-level ARIs spanned 0.465 (Panariello2023) to 0.916 (Guan2022) in human and 0.606 (Guo2019–OSK) to 0.992 (Guo2019–CIP) in mouse. Among the three boundary states, Schiebinger2019–2i L00 scored above other R states for G2/M in 24/29 libraries but for matrix in only one (a cycling-enriched remodeling state), whereas Guo2019–CIP C012 (all four eligible libraries) and Xing2020 C005 (its sole eligible library) retained stronger matrix and weaker pluripotency programs than neighboring E states (Table S1a).

Cross-species alignment. Cross-species links in the joint display touched 26.7% of cells and 1,463/3,038 human–mouse state pairs, with held-out expression support exceeding its null in 10/12 route pairs under the primary fit and 115/144 refits (Figure S3e,f). Support was complete for every Xing2020 and Panariello2023 pair but weak for Guan2022–0605 and Guan2022–0618 against Guo2019–OSK (three and four of 12 refits), aligning broad expression programs rather than identical states.

PAS measurement. Reference-supported primary PASs carried an AATAAA or ATTAAA motif in 62.2%–71.7% of sites (peaking at −20 bp in every study), versus 6.8%–19.1% of unsupported sites and 2.5%–5.2% of matched genomic positions, with mean downstream A fractions of 0.20–0.23, 0.30–0.34 and 0.27–0.30 (Figure S4, Table S2a). Support varied little from 25- to 100-bp matching (60.8%, 64.0% and 67.5% of Guan2022 sites and 90.2%, 93.4% and 95.0% of UMIs), whereas raising the depth threshold from 20 to 40 and 80 PAS UMIs per metacell reduced complete S–R–E–P coverage in Xing2020 from 4,378 to 2,761 and 1,600 genes, with comparable mouse losses.

Route means and source choice. Across all 16 measurement settings, documented-source P–S route means preserved the human–mouse ordering reported in the main text (Figure S5b,c, Table S2b). In Guan2022–0809, the only series whose 16-setting range (-0.0046 to $+0.0066$) crossed zero, the expanded layer lowered the mean by 0.0092, comprising 0.0059 from re-estimation on 5,826 common genes and 0.0033 from 1,077 added genes. Single-source P–S means spanned -0.0070 to $+0.0182$ in Guan2022–0618 and -0.0392 to -0.0243 in Schiebinger2019–2i, moving a human route across zero without reversing the route order.

Tandem genes and the naive-related state. Tandem-3′ UTR genes (1,565/4,339 in Xing2020, 686–891 in Guan2022, 1,341 in Guo2019–CIP and 949 in Schiebinger2019–2i) preserved the route order, with mean shifts of $+70.2$, $+0.5$ and $+51.0$ nt in human versus -49.7 and -94.5 nt in mouse (Figure S5d–f, Tables S2c and S2e). In Liu2020 RSeT, naive-related hN was proximal to P across 459 primary-setting genes (mean -0.0092, 95% bootstrap interval -0.0117 to -0.0069, 78 proximal and 21 distal genes at 0.02, versus $+0.0015$ for P–S) and across 307–515 genes under other settings, while same-library hN–M contrasts were unavailable (Section S2.9, Figure S22e).

Observed-source references. Contrasts against observed source-like cells were small in routes without a documented-source design, spanning $+0.0062$ to $+0.0087$ in Guo2019–OSK R, E and M, -0.0142 to -0.0048 in Liu2020 E, P and M, and -0.0014 and $+0.0101$ in Panariello2023 P and M, and retained their signs across fixed common backgrounds of 1,120–6,452 genes (Figure S5a, Table S2e).

S2.2. Within-species recurrence

Null models and measurement controls. Same-direction gene-level APA recurrence exceeded matched expectations across all four nested null levels L0–L3 (five models including the two L2 ordering variants, Figure S6a,e, Table S3b). From L0 to L3, observed/null ratios at $|\Delta\mathrm{DWUI}| \geq 0.02$ moved from 2.05 to 1.77 in human P–S, 1.70 to 1.61 in mouse P–S, 2.12 to 1.80 in human P–M and 2.09 to 1.93 in mouse P–M, and ranged from 2.20 to 3.99 at 0.05 ($q < 0.001$ across all 40 tests). In human P–M, one-, two- and three-study support occurred in 1,914, 231 and 37 genes versus null medians of 2,144, 143 and 6. Across measurement controls (Figure S6c,d, Table S3d), split-half pseudo-contrasts yielded medians of 10–45 genes versus 93–515 observed across 100 splits. Across human P–S, human P–M, mouse P–S and mouse P–M, bootstrap intervals retained 386/483, 175/268, 513/604 and 372/420 recurrent directions and 20-UMI thinning retained 435/483, 211/268, 540/604 and 373/420 (while 40-UMI thinning reduced membership to 79–247 genes). Together with P–S cycle-matching (367/483 human, 260/604 mouse) and common-axis (413/483, 537/604) controls, these variants preserved P–S observed/null ratios of 1.56–1.84 in human and 1.34–1.68 in mouse ($q < 0.001$ at every tested position of the 112-position family). Leaving one study out of human P–M gave 79, 166 and 97 recurrent genes versus null 95% ranges of 29–50, 49–74 and 46–69, and separating the Guan2022 series gave 1,277 human P–S genes versus 860–931 expected (1.43-fold).

Direction-specific recurrence. Both proximal and distal recurrence exceeded the L3 null in all four sets at 0.02 ($q_8 = 0.0001$ each, Figure 2a, Figure S6b, Tables S3c and S3g), while the distal fraction was closer to one half than expected in human P–S (70.2% versus null mean 78.7%, 95% range 74.7%–82.6%), mouse P–S (15.4% versus 9.4%) and mouse P–M (11.4% versus 5.3%, $q_4 = 0.00027$ each, with 166 excess proximal versus 36 excess distal genes), but not in human P–M (46.3% versus 49.5%, $q_4 = 0.27$). At 0.05, proximal and distal enrichments remained significant in every set, with folds of 3.63 and 2.05 in human P–S, 2.03 and 4.27 in mouse P–S, 3.27 and 2.49 in human P–M and 2.58 and 6.90 in mouse

P–M, and the distal-share differences persisted in human P–S, mouse P–S and mouse P–M ($q_4 = 0.015$, 0.010 and 0.015, versus $q_4 = 0.37$ in human P–M).

Strict tandem-3′ UTR genes. Among genes whose entire primary PAS axis lay in one shared terminal 3′ UTR (580 human and 670 mouse P–S genes, and 389 and 390 P–M genes, Table S3h), recurrent P–S shifts were 78.6% lengthening in human (92/117) and 12.2% in mouse (33/270). In P–M at 0.02, shortening and lengthening both exceeded expectation in human (45 versus 31.0 and 38 versus 28.4) and mouse (162 versus 111.3 and 9 versus 3.2, $q_8 = 0.00013$ for shortening and $q_8 = 0.0014$ for lengthening). At 0.05, human P–S lengthening (47 versus 29.1), mouse P–S shortening and lengthening (122 versus 77.8 and 13 versus 2.3), human P–M shortening (18 versus 9.7) and mouse P–M shortening (100 versus 57.1) remained enriched ($q_8 = 0.00016$ each), whereas the three smallest sets (human P–S shortening with 4 genes, human P–M lengthening with 11 and mouse P–M lengthening with 2) did not pass correction ($q_8 = 0.14$–0.17).

Independent wells. Across independent Schiebinger2019–2i wells (614 eligible genes with 8–22 wells over 4–11 dates, Figure S6f,g, Table S3d), joint $q < 0.05$ supported 370 genes for DWUI, 373 for RWUI, 381 for MPRO, 318 for PDUI, and 288 for PPUI (351 shared between DWUI and MPRO and 222 supported across all five metrics). Among the 143 eligible recurrent mouse P–M genes, 134 were supported in the recurrent direction for DWUI, alongside 134, 132, 119, and 107 for MPRO, RWUI, PDUI, and PPUI.

External PAS-seq. In external bulk PAS-seq (GSE99922, Figure S6h, Table S3d), 276 of 604 mouse P–S candidates were measurable and 245 (88.8%) were matched under the primary 1:3 matching setting, which narrowly missed the $|\text{SMD}| \leq 0.20$ balance acceptance criterion (maximum $|\text{SMD}| = 0.2019$, marked fail in Figure S6h and treated as descriptive). By contrast, both the 50-count sensitivity setting (203/252 candidates, 80.6% retention, maximum $|\text{SMD}| = 0.169$) and the 1:2-control sensitivity setting (263/276 candidates, 95.3% retention, maximum $|\text{SMD}| = 0.136$) met both balance criteria, whereas 100-count matching retained 131/201 candidates (65.2%, below the 80% retention criterion despite maximum $|\text{SMD}| = 0.112$). Under the primary setting, candidate total variation distance exceeded controls by 0.0123 (0.0051–0.0143 across nine library weightings, and 0.0137, range 0.0074–0.0166, under 1:2 matching; descriptive across six whole-library assignments).

Recurrence across opposing expression responses. Among genes responding at 0.02 in both studies (Figure S8, Table S3e), the APA-same/GEX-opposite class held 83 human and 92 mouse genes (identity enrichments 1.44 and 1.41, alongside 245 and 393 APA-same/GEX-same genes at 1.48 and 1.43), while APA-opposite classes were depleted (75 and 28 human and 95 and 31 mouse genes, 0.65–0.76). At 0.05, the APA-same/GEX-opposite class retained 38 human and 49 mouse genes (identity enrichments 1.72 and 1.79, $q = 0.0002$, direction enrichments 1.20 and 1.23, $q = 0.022$ and 0.0008, and $q \leq 0.0105$ across all three-bin tests), exemplified by human *AP1S2* (ΔDWUI $= -0.25$ to -0.29, GEX -1.15 in Xing2020 versus $+2.56$ in Guan2022) and mouse *Rtf2* (ΔDWUI $= -0.13$ and -0.22, GEX $+0.38$ and -0.33).

Functional backgrounds. Across GO-annotated expressed (G0, 13,636–14,769 genes), APA-testable (G1, 1,357–3,666) and recurrent (G2, 252–564) backgrounds (Figure S7a,b,d,e, Table S3f), all 14 L3-matched discoveries compared G1 with G0 (12 GO terms led by cytoplasmic translation in human P–M at 98 versus 64.0 expected, $q = 0.0003$, plus two KEGG pathways), whereas unmatched L0 testing gave 179 GO terms for G2 versus G0 and single-analysis L3 testing supported only arginine and proline metabolism in human distal P–S versus G1 ($q = 0.031$, 28-analysis grid $q = 0.18$). Median nominal-0.05 G2 power at odds ratios 2, 4 and 8 was 0.18, 0.53 and 0.89 for GO (0.15, 0.51 and 0.90 for KEGG) and lower after multiple-testing correction, leaving moderate functional enrichment unresolved.

S2.3. Composition of the global direction

Proximal and distal contributions by route. On the 1,306 shared one-to-one orthologs, decomposing each route's P–S mean into positive (distal) and negative (proximal) components gave distal contributions of $+0.025$ in Xing2020 and $+0.014$ and $+0.019$ in the two Guan2022 series versus $+0.007$ and $+0.009$ in Guo2019–CIP and Schiebinger2019–2i, and proximal contributions of -0.007, -0.009 and -0.012 in human versus -0.023 and -0.037 in mouse (Table S2f). Equal-study weighting yields the descriptive human–mouse difference reported in the main text ($0.034 = 0.021$ proximal $+0.013$ distal).

Marker-defined mesenchymal reference. Redefining M by expression markers, with P fixed, left the proximal composition of mouse P–M nearly unchanged (36.98% versus 36.50% of 3,310 Guo2019–CIP genes and 33.85% versus 33.59% of 1,551 Schiebinger2019–2i genes at $\Delta\text{DWUI} \leq -0.02$) and shifted Xing2020 from 15.46% to 13.33% (1,831 genes) and Panariello2023 from 18.85% to 20.02% (5,081 genes), but reversed the global direction of Liu2020 (Table S10a). In Liu2020 (902 genes), proximal responders rose from 11.86% to 20.62% and mean P–M ΔDWUI shifted from $+0.0089$ to -0.0035 because 12 of the 18 marker-defined M metacells came from cluster-defined source-like states and only four from mesenchymal states, whereas Guan2022 lacked a same-library P–M design.

S2.4. Cross-species comparisons

Sharing sensitivity and continuous correspondence. Across the threshold and layer grid, paired P–M shared proximal candidates exceeded the joint null after 16-test correction at 0.03 in both layers ($q_{16} = 0.037$ and 0.041), reached $q_{16} = 0.051$ at the primary 0.02 setting (versus $q = 0.032$ in the two-contrast family) and gave $q_{16} = 0.060$–0.20 elsewhere, whereas observed-S P–S passed only at 0.01 in the supported layer (62 versus null range 36–55, $q_{16} = 0.013$, Figure S9, Tables S4a and S4b). Under proximal-sharing injection, L3 rejected at 3.4% under no enrichment for both P–S and P–M (versus 7.1% and 5.9% under L1), with power of 0.84 and 0.47 at odds ratio 2 and 1.00 and 0.94 at odds ratio 4. In study-pair tests across jointly measurable orthologs without requiring within-species recurrence, only the two Guan2022 P–S pairs exceeded the Q5 null range (164 versus 120–157 and 116 versus 78–106), no MPRO sharing test ($q_{24} \geq 0.053$) or direction-difference test ($q \geq 0.65$) passed correction, and 12 of 24 per-pair correlations had positive 95% intervals excluding zero, led by M–S (mean 0.069, maximum 0.182 in Xing2020 with Guo2019–CIP).

Expression- and coverage-matched sharing. Adding expression and APA-coverage terciles to the Quintile and Range models preserved P–M proximal sharing (20 observed versus 10.6 and 12.1 expected, 1.89- and 1.66-fold, $q_4 = 0.0056$ each) while P–S remained unenriched (23 versus 23.5 and 24.5, $q_4 = 0.68$, Table S4b). For P–M, movable labels remained for 97.4% of human and 96.7% of mouse candidates under Quintile matching (zero fixed overlaps) versus 59.1% and 81.5% under Range matching (three fixed overlaps), with post-matching maximum standardized differences of 0.189 (raw) and 0.194 ($\log_2(1 + x)$), null rejection rates of 1.2% and 1.8% at $\alpha = 0.025$, and power of 0.28 and 0.20 at odds ratio 2 (0.83 and 0.69 at odds ratio 4).

Direction pairing. Under the coarser measurement and PAS-capacity model at $|\Delta\text{DWUI}| \geq 0.02$ across 1,656 P–S and 751 P–M orthologs, shared distal P–S and shared proximal P–M pairs also remained enriched ($q_8 = 0.0016$ and 0.0036; primary full-assay tests in Figure 3a,b and complete 3×3 counts in Table S4f), whereas opposite-direction cells remained unenriched under both models (31 versus 28.9 in P–S and 19 versus 20.7 in P–M, $q_8 \geq 0.42$). At $|\Delta\text{DWUI}| \geq 0.05$, shared proximal P–M pairs remained enriched under both models (7 versus 2.11, $q_8 = 0.013$), whereas shared distal P–S pairs (4 versus 1.45) passed only under the coarser model ($q_8 = 0.044$ versus 0.14 under the full model, in

which 38.3% and 55.9% of human and 23.3% and 26.4% of mouse P–S and P–M labels were fixed within their strata, limiting power in non-enriched cells).

Event classes. Partitioning the 751 P–M orthologs into 315 tandem-3′ UTR, 52 ALE-compatible, and 384 other/mixed pairs allocated 17, 4, and 6 of the 27 shared proximal pairs (Figure S10a,b,c, Table S4g). Tandem enrichment passed under both the coarser and full models (17 versus 7.64 and 8.98 expected, $q_4 = 0.00016$ and 0.00024), across nine and eight of nine thresholds ($q_{36} < 0.05$) and at 0.05 (6 pairs, $q_4 = 0.0040$), whereas the four ALE-compatible pairs (*PCMT1*, *KLC1*, *POLR1D*, and *PDLIM7*) were nominal only under the coarser model (4 versus 1.68, $q_4 = 0.052$, and 4 versus 2.80, $q_4 = 0.18$ under the full model). Among the 67 pairs whose entire primary PAS axis lay in a single terminal 3′ UTR in both species, eight shifted proximally in both species against 4.5 and 5.3 expected, and within-species class splits remained strongly proximal in mouse (120/122 tandem and 47/57 ALE responders) versus balanced in human (28/59 and 14/27).

Corresponding PAS switches. Of the 48 same-direction orthologs (Table S4j), nine had a strict tandem-3′ UTR axis in both species (Figure S10d,e, Table S4h). Across the five homologous-PAS filtering steps (at least two matched PASs in conserved order, $\geq 80\%$ usage on matched sites in every study and state, and judgeable, corresponding and reference-supported gain and loss PASs), 25-nt matching retained 7, 2, 1, 1 and 1 gene (*DYNLL2* in P–S), while 50-nt matching retained 8, 4, 3, 2 and 2 genes (*DYNLL2* in P–S and *LRRC59* in P–M), where step failures leave genes unevaluable rather than estimating how often shared responses use homologous PASs. In *DYNLL2*, the segment between the matched proximal and distal PASs (1,773 nt in human and 1,731 nt in mouse) gained inclusion from S to P and contained 13 reciprocally mapped predicted miRNA seed matches.

Homologous PAS correspondence. On 25-nt homologous PASs across the Xing2020 pairs with Guo2019–CIP and Schiebinger2019–2i (189 and 158 genes, 216 in their union) and Liu2020 with Guo2019–CIP (116 genes), P–M rank correspondence matched M–S without exceeding it (pair-mean $\rho = 0.220$ versus 0.215, difference 0.005, 95% interval -0.145 to $+0.144$, distance-axis P–M $\rho = 0.221$, Figure S11, Tables S4c and S4d). At 50 nt (251 and 126 genes), P–M ($\rho = 0.243$, $q_8 = 0.0016$) exceeded P–S ($q_8 = 0.0044$) but not M–S ($q_8 = 0.27$). Conversely, in the 126-gene P/E/M cohort E–M corresponded across species ($\rho = 0.252$, $q_8 = 0.0044$) while P–M did not ($q_8 = 0.095$), and full native axes including unmatched PASs weakened P–M correspondence ($\rho = 0.106$, -0.032 to $+0.241$). In *PDLIM7*/*Pdlim7*, P used the matched proximal PAS more than M in both species (human 0.310 versus 0.223, mouse 0.704 versus 0.271 in Guo2019–CIP, ≥ 0.886 matched-site usage), where the shorter Ensembl 116 coding isoform shares codons 1–190 with the 457-codon form before a 32-codon alternative last exon, retaining the UniProtKB PDZ domain (residues 1–85) while omitting all three LIM domains (residues 280–457, Q9NR12 v204 and Q3TJD7 v152) [53].

Naive specificity. In the equal-weight N6–P7 and N8–P7 naive-related contrast in Liu2020 (662 proximal and 422 distal genes at 0.02 among 2,575, Figure S12, Table S4i), 79 of 191 human proximal genes on the 784-ortholog P–M background overlapped the 218 mouse proximal recurrent genes (56.8 expected, 1.39-fold), and 46 of 181 on the 745-ortholog background overlapped the 120 mouse genes also proximal in P–S (31.4 expected). Across all 14 direct comparisons against human control contrasts, however, naive-minus-control enrichment differences ranged from -0.48 to $+0.23$ and did not pass correction under any of the four null models ($q_{14} \geq 0.35$ at 0.02 and $q_{14} \geq 0.055$ at 0.05, with 1.40- versus 1.24-fold, $P = 0.10$, on the largest 749-ortholog cross-library P7–S block and 356–369 orthologs in same-library controls).

Shared proximal set under a marker-defined reference. On the 728 P–M orthologs qualifying under all three M definitions, shared proximal enrichment held for cluster-defined M (25 versus 14.5 expected, $q_{72} = 0.0087$), marker-defined human M (31 versus 18.8, 95%

null range 13–25, 1.65-fold, $q_{72} = 0.0079$, passing at eight of nine thresholds) and marker-defined M in both species (31 versus 18.3, $q_{72} = 0.0022$, seven thresholds), with no reversal enrichment and 23 of the 27 primary shared pairs retained (individual gene retention and additions in Section S2.11, Tables S10b and S10c).

S2.5. Interval inclusion and predicted sites

Recurrent interval cohorts. Across the union candidate pool (878 human P–S, 396 human P–M, 1,210 mouse P–S and 1,020 mouse P–M genes measurable in both studies), matched terminal-UTR interval pairs changing strictly in both studies occurred in 77, 23, 179 and 246 genes (170, 40, 385 and 660 pairs), of which 129, 33, 376 and 660 pairs changed in the same direction (strict recurrent intervals, Figure S13a,b,c, Tables S5a, S5b and S9b). Mouse pairs were predominantly losses in both studies (P–M 654/660, P–S 343/385), whereas human P–S pairs were mostly gains (106/170, with 41 discordant), and the between-study correlation of inclusion changes in human P–M rose from 0.32 at 20 UMIs to 0.74 at 50 UMIs (0.52 for the two-layer mean).

Local direction and whole-gene net displacement. Among the 246 strict-interval mouse P–M genes (236 entering via DWUI and 10 via MPRO alone; two-study native P–M partition in the main text, Figure 6b and Table S6a), 105 of the 124 genes without a comparable two-study native estimate lacked a same-library Schiebinger2019–2i estimate. In Table S6a, mouse P–S compares observed-S local inclusion with documented-source DWUI across different references, whereas human P–S lacked a comparable documented-source estimate for its interval-study pair.

Low net displacement. Among the 51 mouse P–M genes passing the low-net-displacement screen ($|\Delta\text{DWUI}| < 0.02$, MPRO ≥ 0.10, Figure S14, Table S6b), 36 had a multi-PAS terminal-family estimate in both studies (median native span 16.6–17.7 kb) and 15 in neither (25–27 kb, overall median 19.1 and 18.5 kb, up to 311 kb). Across the 36 evaluable genes, terminal-family shifts were proximal in both studies for 27 genes and distal for 6 ($\rho = 0.79$, median magnitudes 74 and 76 nt, and 113 and 107 nt across the seven strict-interval genes, where only *Prpf38b* shifted distally while outside-family and within-family terms combined or opposed per study as detailed in Table S6b). Requiring $|\Delta\text{DWUI}| < 0.01$ in both studies retained *Trip12*, *Rhoa*, *Capzb* and *Rad23b* (five interval pairs, Figure S14b,e).

Component terms and 50-UMI sensitivity in Riok3. In *Riok3* (main-text 20-UMI interval loss and native ΔDWUI summary in Figure 6c and Table S6d), the 20-UMI comparison of the shared 889-nt (within the 1,204-nt strict) interval spanned 3 Guo2019–CIP and 23 Schiebinger2019–2i library pairs, and at the stricter 50-UMI cutoff inclusion of this interval fell by 17.1 percentage points (pp) across 17 Schiebinger2019–2i libraries. On the native axis (3 and 6 paired libraries), declining outside-family usage in Guo2019–CIP (7.34% to 3.46%) contributed $+0.0341$ and family-mass change contributed $+0.0014$ against a -0.0108 within-family proximal term (net $+0.0247$), whereas in Schiebinger2019–2i the within-family, outside-family, and mass terms were -0.0062, -0.0068 and -0.0002 (net -0.0132).

Component terms and 50-UMI sensitivity in Fgfr1op2. In *Fgfr1op2* (human ortholog *FGFR1OP2*; main-text summary in Figure 6d and Table S6a), the native P–M decomposition spanned 3 Guo2019–CIP and 8 Schiebinger2019–2i library pairs. Reduced usage of the upstream ALE PAS (51.8% to 43.1% in Guo2019–CIP and 56.0% to 46.3% in Schiebinger2019–2i) yielded outside-family terms of $+0.0432$ and $+0.0330$ and family-mass terms of $+0.0112$ and $+0.0066$ against within-family proximal terms of -0.0209 and -0.0157 (three-PAS terminal-family shifts of -365 and -428 nt). Alongside the 970-nt interval, inclusion of a second 492-nt strict interval fell by 23.5 pp in Guo2019–CIP (3 libraries at both cutoffs) and

by 30.6 pp at 20 UMIs in Schiebinger2019–2i (21 libraries), and at 50 UMIs inclusion of both the 970- and 492-nt intervals fell by 34.0 pp across 8 Schiebinger2019–2i libraries.

Weighted predicted-site content. Because predicted-site retention follows interval inclusion by construction (Figure S13d,e, Table S5c), median per-gene miRNA W_{20} was -17.7, -8.9, $+5.2$ and -2.5 site equivalents in mouse P–M, mouse P–S, human P–S and human P–M (14 losses and 6 gains among 20 human P–M genes), and RBP sites showed the same pattern (193 losses among 194 site-bearing mouse P–M genes, with 52 carrying none and a zero median 50-minus-20-UMI difference, 5%–95% range -2.15 to $+1.96$).

Predicted-site density. Equal-length stable-window matching succeeded for only 29/661 strict mouse P–M atomic density windows (formed from the union of study boundaries across the 660 matched interval pairs of Table S5b plus one *Ttl* boundary window without a joint position match; 25 genes), 8/376 mouse P–S, 9/129 human P–S and 5/33 human P–M windows (Figure S16a,d, Table S5d). In mouse P–M, changed-minus-stable density differences were $+1.13$ miRNA sites/kb (95% interval -10.5 to $+14.6$, $P = 0.88$) and $+0.20$ RBP sites/kb (-0.60 to $+1.05$, $P = 0.67$, both $q = 1$, and $q \geq 0.43$ across all 48 background and 12 grid tests, with power of 1.0 at $+2$ RBP sites/kb versus 0.38–0.83 at $+10$–20 miRNA sites/kb). External miRNA seed-group comparisons likewise covered only 2.18% of lost mouse P–M bases (28 windows in 24 genes, 11,094/509,854 bp) and 1.41% in mouse P–S (8 genes, alongside 2 human P–S and 4 human P–M genes, all < 10 genes and thus descriptive), showing no seed-density difference in mouse P–M between somatic- and PSC-expressed miRNAs (-0.003, -0.043 to $+0.035$, $P = 0.88$) or between barrier and ESCC seeds ($+0.061$, -0.45 to $+0.61$, $P = 0.82$, both $q_8 = 1$, and $q_{30} = 1$ across all 30 control positions, Figure S17a,b,d–f, Table S5d).

Partial retention. Exact cross-study partial site retention (a changed site coexisting with an unchanged site of the same factor) occurred in 976 miRNA and 704 RBP gene–factor pairs in mouse (234 and 222 genes) and 235 and 231 in human (55 and 50 genes), occurring more frequently for RBP than miRNA sites in every cohort (Figure S16b,c,e–g, Table S5f). Examples with an unchanged companion site included CARHSP1 in mouse *Snx30* (-28.3 and -31.8 pp across 3 and 11 library pairs), BOLL in human *SH3PXD2A* (-25.5 and -19.5 pp) and the distal miR-34/449 site in *Eif4ebp2* (leave-one-library-out -33.3 to -29.8 pp in Guo2019–CIP, -39.1 pp at 50 UMIs across 16 Schiebinger2019–2i libraries, with orthologous human losses in Xing2020 and Liu2020).

Trip12 across libraries. In *Trip12* (Figure S15a–d, Table S6c), P–M inclusion at 20 UMIs fell from 48.6% to 33.6% in Guo2019–CIP and from 50.0% to 32.2% in Schiebinger2019–2i for the 842-nt interval, and from 36.7% to 21.9% and 39.7% to 19.7% for the 706-nt interval (with 20-UMI leave-one-library-out shifts spanning -18.7 to -10.4 pp across the two intervals in Guo2019–CIP and -20.7 to -17.4 pp in Schiebinger2019–2i, and 50-UMI shifts of -18.5 pp for the 842-nt interval and -19.9 pp for the 706-nt interval across 20 qualified Schiebinger2019–2i libraries). Within the 3,108-nt terminal family (spanning four of the six native PASs in Guo2019–CIP and four of the seven in Schiebinger2019–2i), usage of the most proximal PAS rose from 0.51 and 0.46 to 0.66 while usage of the most distal PAS fell from 0.17 and 0.20 to 0.07 and 0.05.

External records for Trip12. Among 76 filtered external long-read isoforms for *Trip12* (Figure S15e, Table S6c), one isoform pair (detected separately in 7 and 3 samples) strictly excluded the 706-nt interval while retaining two nucleotides of the 842-nt interval. Neither interval overlapped an individual wild-type AGO2 peak (merged wild-type tracks overlapped the 706- and 842-nt intervals by 132 and 3 bp, and merged Dicer-knockout tracks overlapped the 706-nt interval by 80 bp), while expression filtering retained 16 PSC-expressed miRNA seed matches, 2 direct RBP motifs and 29 transferred RBP motifs (excluding 52 miRNA and 4 RBP annotations).

Factor-expression context. Across candidate RBPs, 241 of 260 reached ≥ 2 CPM in at least one qualified library–state (128/143 human and 113/117 mouse, Table S5e). In P of both mouse studies, 25 of 27 RBPs with transferred motifs in the two *Trip12* intervals (all except CELF3 and RBM24, Figure S17c) and 12 of 14 in the *Riok3* interval (all except KHDRBS2 and SAMD4) reached ≥ 2 CPM. Among the predefined display RBPs (Figure S17g,h), ELAVL2 reached ≥ 2 CPM only in Liu2020 P, whereas HNRNPC and PCBP1 were highly expressed across all states.

S2.6. Candidate explanations of the shared proximal response

Cell cycle and CPA-factor expression. Across all five paired P–M series (Xing2020, Liu2020, Panariello2023, Guo2019–CIP and Schiebinger2019–2i), P had higher cell-cycle scores ($+0.26$ to $+0.47$, reported in the main text) and higher expression of 9–11 of the 11 core CPA factors than co-captured M, including *NUDT21* (Δmean $\log_2(\mathrm{CPM}+1)$ of $+0.60$ to $+1.69$, Figure S18a,b,g, Tables S7a and S7b). From documented S to P, however, the cell-cycle score rose more in distally shifting Guan2022–0618 ($+0.27$, mean $\Delta\mathrm{DWUI} = +0.0057$) than in proximally shifting Guo2019–CIP ($+0.13$, -0.0139), while *NUDT21* rose in all five documented-source routes and *CPSF6* fell only in Guo2019–CIP. Within P, the partial correlation between cell-cycle score and mean PAS position was -0.04 and -0.08 in the two mouse routes (library-bootstrap intervals spanning zero) and -0.52 to $+0.43$ across the human series.

Cycle adjustment of P–M. Although P had higher S-phase and G2/M marker scores than M in Xing2020, Guo2019–CIP, and Schiebinger2019–2i (corrected support in Schiebinger2019–2i only), common-support diagnostics yielded no estimable cycle-adjusted P–M APA comparison (Table S7g). Of 36 physical-library P/M contexts across five studies and 53 P/M/S contexts across three documented-source studies, 28 and 50 lacked a nonnegative common marker-mean target due to nonoverlapping marker ranges, and the remaining eight P/M and three P/M/S contexts (as well as all 60 fixed 2×2-bin contexts) failed the predefined distribution-balance, variance, or effective-sample-size criteria before gene-level depth filtering, leaving all 16 planned cycle-adjusted APA test positions unavailable. Within-library cell-cycle stratification of P and the human common-support window are detailed in Section S2.7.

Upstream UGUA. On the 52 one-to-one orthologs eligible in both species and on each species' strict tandem-3′ UTR background, distal-minus-proximal UGUA counts in $[-100, -40)$ nt exceeded matched expectations by 0.25 and 0.18 for mouse P–M proximal responders relative to nonrecurrent genes ($q_8 = 0.083$ each) and by 0.02 and 0.09 in human ($q_8 = 0.47$ and 0.32, with the six common-background human genes fixed within their strata), while all comparisons against distal responders ($q_8 \geq 0.32$) and all 208 exploratory window, null, and control-motif tests ($q \geq 0.80$) were non-significant (Figure S18d, Table S7c).

S–M contrast and within-date well differences. On the 27 shared proximal orthologs, route-level S–M means were negative in five of six evaluable series (-0.045 to -0.021 across 26–27 measurable genes with S–M cycle-score differences of $+0.03$ to $+0.30$, versus $+0.035$ on 16 genes in Liu2020 with $+0.04$, Figure S19a, Table S7d). Across the seven prespecified two-well dates in Schiebinger2019–2i (14 wells, 5–22 measurable shared genes per date, Figure S19b, Table S7e), leave-one-date-out correlations ranged from $+0.16$ to $+0.80$ around $r = +0.66$ for the cell-cycle score (two-sided exact $P = 0.36$, $q_2 = 0.72$ over $2^7 = 128$ within-date label flips) and from -0.44 to $+0.32$ around $r = +0.03$ for the 11-gene CPA-factor score ($P = 0.97$, $q_2 = 0.97$). Across all 11 two-well dates (22 wells), a fixed control panel of 85 high-coverage non-shared genes measurable in all 24 libraries had $r = -0.12$ (leave-

one-date-out -0.57 to $+0.33$), and its 45-ortholog and 8-gene mouse proximal recurrent subpanels had $r = -0.23$ and -0.15.

Candidate mechanisms. Sequence, perturbation, and functional checks identified no single driver of the shared set (Figure S19c–e, Table S7f). None of the eight shared orthologs among 67 with complete distal regions in both species carried a conserved AAGUGCU ESCC seed (0.64 expected, $q_{18} = 1$), and PAS anchor architecture did not differ from expectation ($q_{12} \geq 0.074$). External QKI-knockdown proximal targets (2/25 versus 0.87 expected, $q_{36} = 0.66$), EMT distal targets (3/25 versus 0.55, $P = 0.0074$, $q_{36} = 0.12$), and reciprocal U1 perturbation responses (5/10 shared versus 96/176 background genes) were likewise unenriched, as were the four membrane-system GO categories (1–5 shared genes versus 0.9–3.1 expected, $q_{16} \geq 0.59$) and the three RNA-regulation categories among the 48 same-direction orthologs (such as 10 RNA-binding genes versus 14.0 expected, $q_6 = 0.97$, Table S4j).

Cis-feature prediction. Across the four primary cohorts (995 human P–S, 335 human P–M, 969 mouse P–S and 356 mouse P–M discovery genes, with 223, 99, 123 and 49 same-direction orthologs in the other species, Figure S19f–i, Table S4e), All-cis versus M1 likelihood-ratio statistics were 10.65, 13.83, 2.63 and 2.69 (bootstrap $P = 0.053$, 0.017, 0.745 and 0.749, minimum $q_4 = 0.069$, and $q \geq 0.19$ across all 32 grid settings). No feature expansion yielded an out-of-fold AUC gain with a 95% bootstrap interval above zero (Sequence in mouse P–S changed AUC by -0.012, interval -0.025 to -0.0007, adding recurrence to M0 gave -0.0125, and human P–M All-cis repeat gains of $+0.010$ to $+0.044$ had gene-bootstrap and coefficient intervals spanning zero), while strong collinearity among homology features ($\rho = 0.84$–0.94 versus ≤ 0.30 with sequence features) precluded separating their individual contributions.

S2.7. Cell-cycle stratification within P

Library eligibility and global direction in the lower-cycle half of P. Under the within-library median cell-cycle split of purity-$\geq$ 0.8 P metacells (Figure 5a, Figure S18e, Table S10e), group-level eligibility held in 8/9 human P–M libraries (all except two-metacell Panariello2023 D9A_rep2_GSM6894037) and 22/27 mouse libraries (3/3 in Guo2019–CIP and 19/24 in Schiebinger2019–2i for the lower-cycle half, 21/24 for the higher-cycle half and 19/24 jointly). Lower-cycle-half-minus-M cycle-score differences were positive in all 9/9 human and 27/27 mouse libraries before filtering, with eligible-library medians of $+0.338$ in human and $+0.219$ in mouse (library-level ranges in the main text). Across the 80 single-route and 96 route-pair scenarios, human route means exceeded mouse route means in all 38/38 estimable recomputed-background and 88/88 original-background comparisons (minimum difference $+0.0119$, Panariello2023 versus Guo2019–CIP, with Xing2020 lacking an eligible five-metacell library). Primary-setting means spanned -0.0083 to $+0.0102$ across the three human series (1,054–5,258 genes, 16-scenario range -0.0084 to $+0.0104$) versus -0.0233 in Guo2019–CIP (2,562 genes, -0.0250 to -0.0194) and -0.0306 in Schiebinger2019–2i (1,206 genes, -0.0358 to -0.0289).

Directional splits, null ranges and candidate retention in the lower-cycle half of P. Beyond the total lower-cycle P–M recurrence counts reported in the main text (Figure 5b,c, Tables S10c and S10e), the 258 and 89 recurrent human genes at $|\Delta\text{DWUI}| \geq 0.02$ and 0.05 (1,860 measurable genes; 95% null ranges 137–173 and 22–41, 1.66- and 2.83-fold) split into 143 proximal and 115 distal genes at 0.02 and 51 and 38 at 0.05. In mouse (1,089 measurable genes; 95% null ranges 149–180 and 51–73, 1.89- and 2.84-fold), the 311 and 176 recurrent genes split into 275 proximal and 36 distal genes at 0.02 and 162 and 14 at 0.05 (descriptive higher-cycle-half counts of 279 and 92 human and 385 and 209 mouse genes in Table S10e). Across the 608 lower-cycle orthologs (Figure 5c; shared proximal cell in the main text),

shared distal pairs numbered 4 versus 0.98 expected (95% range 0–3, 4.10-fold, $P = 0.0091$, $q_4 = 0.036$) and reversal cells remained unenriched (1 versus 1.05 and 16 versus 13.53, $q_4 \geq 0.31$). The 27 original shared proximal pairs partitioned into 14 retained pairs, 6 evaluable pairs losing recurrence in one species (3 human, 3 mouse) and 7 mouse-unevaluable pairs measurable in only one mouse study (*Eif4ebp2*, *Ctdsp2*, *Klc1*, *Ddx6*, *Slc38a2* and *Gnpnat1*) or neither (*Reep3*), while the 19 lower-cycle shared proximal pairs comprised those 14 retained pairs plus 5 newly shared pairs.

Within-P high-minus-low permutation details and the human common cycle-score support window. In the within-P high-minus-low comparison (main-text set means in Figure 5d; Table S10e), the 26 evaluable mouse shared-proximal genes (*Reep3* unavailable) had $D_g < 0$ in 20 genes and $D_g > 0$ in 6 ($T = -0.0107$ versus null median -0.0003, 95% range -0.0090 to $+0.0091$). By route, mean D was -0.0233 (25 genes) in Guo2019–CIP and $+0.0024$ (21 genes) in Schiebinger2019–2i (-0.0219 and -0.0037 across the 20 jointly evaluable genes). Across the three non-significant sets, namely the human shared set (27 genes, $T = -0.0048$, $q_2 = 0.48$), the human complete P–M proximal set (144 genes, $T = -0.0025$, $q_2 = 0.50$) and the mouse complete P–M proximal set (360/372 evaluable genes, $T = -0.0024$, $q_2 = 0.23$), permutation null medians spanned -0.0003 to $+0.00001$ with 95% ranges within -0.0079 to $+0.0076$. Within the common cycle-score support window $[\max(\min P, \min M),\ \min(\max P, \max M)]$ (5/9 human and 0/27 mouse libraries eligible, Figure S18c,f and Table S10e), the 76 recurrent human genes at 0.02 (955 measurable genes; 95% null range 41–61, 1.48-fold, $P = 1.0 \times 10^{-4}$, $q_2 = 0.0002$) split into 22 proximal and 54 distal genes, and at 0.05 recurrence also persisted (14 observed, 3 proximal and 11 distal, versus 5.7 expected, 95% range 2–10, 2.45-fold, $P = 5.0 \times 10^{-4}$, $q_2 = 0.0005$).

S2.8. State-resolved profiles

Resolution. Fitted jointly on 902 human (Xing2020) and 796 mouse (Guo2019–CIP and Schiebinger2019–2i) candidates with complete S–R–E–P profiles, three descriptive profile classes separated progressive proximal, distal-then-proximal, and distal paths (Figure S20a,c, Table S8a). Although $k = 2$ maximized silhouette width (0.534, versus 0.398, 0.346, 0.326 and 0.328 for $k = 3$–6), $k = 3$ retained at least 129 mouse and 145 human genes in every species-specific class.

Path structure. In the reversal class C2, endpoint displacement retained only part of the path and the E–P step carried a median 0.67, 0.40 and 0.54 of path length L in Schiebinger2019–2i, Guo2019–CIP and Xing2020, with median $T = 1 - D/L$ of 0.34, 0.63 and 0.67 (Figure S20b,d,e, Table S8d). Median endpoint retention D/L in C2 (0.37 and 0.33) was lowest of the three classes in Guo2019–CIP and Xing2020 (0.94 and 0.64 in C1, 0.56 and 0.67 in C3), but not in Schiebinger2019–2i (0.66 in C2 versus 1.00 in C1 and 0.57 in C3), and because noise also lengthens L, T is not a calibrated fraction of transient regulation.

Class identity across species. Across the 139 candidate orthologs selected in both species (human C1–C3 counts of 22, 32 and 85 versus mouse counts of 61, 56 and 22, following each species' dominant direction), same-class pairs did not exceed either corrected expectation (46 observed versus 36.0 under the composition null, $P = 0.039$, $q_{20} = 0.262$, and 37.8 under the measurement-matched null, $P = 0.064$, $q_{20} = 0.316$, Table S8b). No cell of the 3×3 class table passed correction, with the largest excess occurring in shared C3 (19 versus 13.5 expected, $q_{20} = 0.124$).

Ranked-set tests. Across 7,780 GO and KEGG tests per layer in the three routes, ranked-set tests of profile amplitude identified 19 APA-associated terms in the supported layer (all in Xing2020) and 41 in the expanded layer (39 in Xing2020 and two in Guo2019–CIP), compared with 1,190 and 1,197 GEX-associated terms (Figure S7c, Table S8c). Although

term effects correlated between layers ($r = 0.886$), the significant APA calls depended on the measurement layer rather than defining a stable functional program.

S2.9. Route, sampling-date and state-reference sensitivities

Global direction and within-species recurrence at the latest eligible P sampling date. Restricting each documented-source P–S route to its latest eligible P sampling date (D40 in Guo2019–CIP and D18 in Schiebinger2019–2i, with single-date human series unchanged, Figure S22c,d, Table S10d) preserved both the human–mouse global direction ordering and within-species mouse P–S recurrence. Across all 160 estimable route-by-setting-by-background combinations, all 96 human-minus-mouse matched-scenario differences on recomputed backgrounds and all 96 on original backgrounds were positive (minimum $+0.0078$, Guan2022–0809 versus Guo2019–CIP). Primary-setting mouse P–S mean ΔDWUI moved from -0.0139 (4,103 genes) to -0.0103 (3,477 genes) in Guo2019–CIP (16-scenario range -0.0160 to -0.0102) and from -0.0312 (2,780 genes) to -0.0485 (2,336 genes) in Schiebinger2019–2i (-0.0514 to -0.0461), versus $+0.0159$, $+0.0057$ and $+0.0046$ in the three human series ($+0.0035$ to $+0.0169$), reflecting the date-restricted measurable gene subsets rather than a pure longitudinal shift on fixed genes. Across the 2,077 genes measurable in both mouse studies after date restriction (2,521 originally), 497 recurred at $|\Delta\text{DWUI}| \geq 0.02$ (430 proximal and 67 distal versus 342.0 expected, 95% null range 320–365, 1.45-fold) and 236 recurred at 0.05 (205 and 31 versus 120.8 expected, range 105–137, 1.95-fold, both $P = 1.0 \times 10^{-4}$, $q_2 = 1.0 \times 10^{-4}$). Of the 604 original recurrent genes at 0.02, 392 (64.9%) retained same-direction recurrence, 105 were measurable in both studies but nonrecurrent, 107 were measurable in fewer than two studies, and 0 reversed two-study recurrence, alongside 105 newly recurrent genes and single-study sign flips in 40/604 genes (13 reaching the opposite threshold in one study, such as *Gabpa* in Table S10d). At 0.05, of the 265 original recurrent genes, 178 (67.2%) retained same-direction recurrence, 36 were measurable in both studies but nonrecurrent, 51 were measurable in fewer than two studies, and 0 reversed two-study recurrence, alongside 58 newly recurrent genes and single-study sign flips in 7/265 genes (1 reaching the opposite threshold in one study).

Cross-species direction pairing at the latest eligible P sampling date. On the 1,410 one-to-one orthologs measurable in at least two studies per species after mouse latest-date restriction at $|\Delta\text{DWUI}| \geq 0.02$ (complete 3×3 counts in Figure S22b and Table S10d), shared distal P–S pairs retained 11 of the 14 unrestricted pairs (12 observed versus 4.74 expected, 95% full-assay null range 1–9, 2.53-fold, $P = 0.0016$, $q_4 = 0.0064$), whereas shared proximal pairs (6 versus 4.64, range 1–9, 1.29-fold, $P = 0.31$, $q_4 = 0.62$) and reversal cells (22 versus 26.02 and 0 versus 0.83, $q_4 = 1$) remained unenriched.

Fibroblast-derived series. Restricting global comparisons to fibroblast-derived series preserved the human–mouse ordering in every scenario (Figure S22a, Table S10d). Across the five fibroblast-derived paired P–M series (Xing2020, Liu2020 and Panariello2023 in human, with 16-scenario means of -0.0007, $+0.0074$ and -0.0053, versus Guo2019–CIP and Schiebinger2019–2i in mouse at -0.0260 and -0.0279), all 96 matched-scenario human-minus-mouse differences across the six series pairs and 16 settings were positive (overall range $+0.0150$ to $+0.0410$). Likewise, all 16 scenarios were positive in the single fibroblast-derived, transcription-factor-induced documented-source P–S pair (Xing2020 mean $+0.0167$ versus Schiebinger2019–2i mean -0.0312, difference range $+0.0448$ to $+0.0497$). Induction cocktail, delivery, culture medium, developmental stage, and laboratory still differ across these routes and remain confounded with species.

Naive-related endpoint reference check. In the Liu2020 state-composition check (Figure S22e, Table S10d), M metacells were present only in S5 (5 metacells, 69 cells) and primed P7 (where 10 of 12 metacells met the purity ≥ 0.8 criterion, spanning 392 of 464 cells) and

were absent in both naive-related libraries, N6 (GSM4546546, 0 M and 14 qualified hN metacells, 1,552 cells) and N8 (GSM4546548, 0 M and 21 qualified hN metacells, 1,912 cells), leaving all 32 planned same-library hN–M scenarios unestimable. The estimable cross-library Liu2020 naive comparisons instead showed modest proximal shifts of hN relative to P in N6–P7 (-0.0099 on 2,620 genes) and N8–P7 (-0.0041 on 2,675 genes), consistent with the within-library N8 hN–P shift reported in Section S2.1.

Response correspondence across R, E and M states in mouse routes. Spearman rank correlations between gene-level ΔDWUI vectors relative to each route's observed S reference across the R, E and M state families were higher on the three-route common gene set for Guo2019–OSK with Guo2019–CIP than for Guo2019–OSK with Schiebinger2019–2i (Figure S23a–e, Table S10f). Specifically, correlations were 0.021 versus -0.059 in R (3,576 genes, $\Delta\rho = +0.080$, conditional 95% bootstrap interval $+0.033$ to $+0.130$), 0.204 versus $+0.063$ in E (3,327 genes, $\Delta\rho = +0.142$, $+0.089$ to $+0.194$) and 0.341 versus -0.028 in M (1,288 genes, $\Delta\rho = +0.369$, $+0.290$ to $+0.451$). Pairwise correlations on each pair's jointly measurable gene set (1,289–4,576 genes, Table S10f) followed the same pattern across R, E and M (0.004, 0.191 and 0.326 for Guo2019–OSK with Guo2019–CIP, -0.055, $+0.072$ and -0.027 with Schiebinger2019–2i, and $+0.164$, $+0.149$ and $+0.227$ for Guo2019–CIP with Schiebinger2019–2i, with both same- and opposite-direction counts at 0.02 exceeding marginal independence in R by 1.61–2.00-fold and 1.18–1.98-fold). In Jaber2022, day-3 GETM and OSKM M–S vectors correlated at $\rho = 0.465$ across 882 genes (137 same-direction versus 36.2 expected and 20 opposite versus 23.4 expected at 0.02). Because study-level PAS catalogs (shared by Guo2019–OSK and Guo2019–CIP, separate in Schiebinger2019–2i), sampling schedules, qualified S, R, E and M library counts (Table S10f) and state composition differ across routes, these correlations cannot separate laboratory, source-cell, and induction-protocol effects.

S2.10. Alternative PAS calling

Route order and gene-level recurrence. Alternative PAS calls retained the route order and supported recurrence against their own nulls, with smaller effects and candidate sets (Figure S21a–c, Table S9a). Every human route remained above every mouse route across all 16 P–S and P–M settings. Mouse means were 30%–41% smaller, including Schiebinger2019–2i P–S at -0.0183 against -0.0312 with polyApipe, narrowing the smallest human–mouse P–S gap from 0.0104 to 0.0044. Effects on common genes correlated at $\rho = 0.61$–0.78 (median 0.71, 811–4,732 genes), and 91.5%–98.3% of genes responding at 0.02 in both workflows shared their direction. Within-species recurrence exceeded its null for both inputs (observed/null ratios 1.62–1.93 with polyApipe and 1.91–2.28 with alternative calls, despite smaller sets such as 277 versus 604 mouse P–S genes), and APA–GEX identity (1.45–1.50) and direction (1.18–1.24, $q \leq 0.013$) tests remained supported.

Cross-species relationships. When called directly from the alternative workflow across all 16,092 ortholog pairs, the 12 shared proximal P–M candidates exceeded the two reference-capacity nulls (12 versus 4.91 and 4.85 expected, 95% null ranges 1–9, 2.44- and 2.48-fold, $q_2 = 0.0058$ and 0.0037) and their expression- and coverage-matched extensions (4.96 and 5.24 expected, ranges 1–9 and 2–9, 2.42- and 2.29-fold, $q_4 = 0.0040$ each), whereas under the joint measurement–PAS null the 12 candidates against 8.38 expected (range 5–12, 1.43-fold, $q_2 = 0.054$) fell just above the multiple-testing threshold and P–S passed none of the nulls (Figure S21c–e, Table S9a). Individual retention of the 27 primary P–M (12/27) and 14 P–S (5/14) pairs is detailed in Section S2.11 (Table S10c). On 25-nt homologous PASs (143 genes), P–M rank correspondence ($\rho = 0.39$, $q_8 = 0.0008$) exceeded M–S ($\rho = 0.08$, $q_8 = 0.26$, difference $q_8 = 0.0027$), whereas in the P/E/M cohort both P–M and E–M corresponded without a P–M advantage, and cis-feature increments remained unsupported

($q_4 = 0.066$–0.449). Because both workflows shared identical expression inputs, the cell-cycle common-support diagnostics were unchanged and neither supplied a balanced P–M context (Table S7g).

Class membership and local coverage. Profile classes agreed more strongly than candidate lists across workflows (Figure S21g,h, Table S9a). Among jointly selected candidates (403/902 human and 277/796 mouse), 91.3% and 89.9% retained their class (ARI 0.81 and 0.69), compared with Jaccard indices of 0.42–0.51 for recurrent genes, 0.12–0.19 for site-retention genes and 0.06–0.13 for exact predicted sites. In the alternative mouse P–M strict-interval pool (39 genes, 19 with comparable two-study whole-gene estimates and 20 unavailable), 13 exceeded 0.02 in the local direction in both studies, five had the local sign below threshold and one had the opposite sign (Table S6a).

Local examples across workflows. In the low-net-shift screen (Figure S21f, Table S9a), alternative calls selected 60 genes (17 shared with the 51 polyApipe genes), of which four had strict intervals (two shared) and two (*Fxr1* and *Riok3*) passed $|\Delta\text{DWUI}| < 0.01$ in both studies. *Trip12* passed the first step under both workflows, with alternative-call losses of 8.6 and 7.0 pp in Guo2019–CIP and 13.2 and 13.2 pp in Schiebinger2019–2i on the 842- and 706-nt intervals at 20 UMIs (3 and 23 paired libraries, meeting the strict criterion in the latter study only). *Riok3* had $|\Delta\text{DWUI}| < 0.01$ under alternative calls ($+0.0001$ and -0.0066), while its 889-nt interval lost 14.8 and 15.8 pp at 20 UMIs (16.5 pp at 50 UMIs in Schiebinger2019–2i) and its terminal family shifted proximally by 160 and 241 nt across four and five native family PASs (Table S6d). For *Fgfr1op2*, alternative native effects were $+0.0237$ and $+0.0154$, and no evaluable alternative interval model was available (Table S6a).

Strict interval pairs across workflows. Across the nine species-by-contrast cohorts, 351 of 1,737 polyApipe strict recurrent interval pairs were evaluable in both studies under alternative calls, and 327 (93.2%) changed in the primary direction in both studies (148 reproducing strict recurrence and 179 remaining below criterion in at least one study, including 119 strict in one), while the remaining 24 changed oppositely in at least one study (Table S9b). Of the 1,386 unevaluable pairs, 1,197 belonged to genes without an alternative interval model and 189 lay outside the alternative terminal family or lacked an eligible effect (in mouse P–M, 131/660 pairs were evaluable, with 51 strict in both, 74 below criterion and 6 conflicting). Non-reproduction therefore primarily reflected pool and model evaluability rather than sign reversal (Table S9a).

S2.11. Ortholog attrition and candidate-level retention

Stage-by-stage attrition of one-to-one orthologs. Tracing all 16,092 high-confidence one-to-one Ensembl release 116 ortholog pairs through the primary-setting measurability requirements retained 1,656 pairs (10.3%) and excluded 14,436 in documented-source P–S (685 insufficient in human only, 1,945 in mouse only and 11,806 in both), and retained 751 pairs (4.7%) and excluded 15,341 in paired P–M (573 in human only, 971 in mouse only and 13,797 in both, Figure S24a,b, Table S10g). Within each species, 3,601 human and 2,341 mouse orthologs were measurable in at least two studies in P–S (12,491 and 13,751 excluded), and 1,722 and 1,324 in P–M (14,370 and 14,768 excluded). Categorizing each excluded gene by the furthest sequential step reached showed that library-pair measurement eligibility (39.1% and 38.6% in P–S, 33.2% and 41.7% in P–M) together with the two-study requirement (17.5% and 12.5% in P–S, 23.2% and 12.7% in P–M) accounted for 51.0%–56.6% of excluded genes across the four species-by-contrast groups, versus 43.4%–49.0% for absence of a primary PAS catalog (1,385–1,873 genes) or failure of usable-axis and reference-supported retained-PAS requirements (4,035–5,139 genes). Because genes are assigned to the furthest sequential step reached, these shares describe the staged filter within each species rather than independent single-factor causes.

Expression and PAS-architecture differences between retained and excluded orthologs. Across all four species-by-contrast groups, pair-retained orthologs (1,656 in P–S and 751 in P–M) had higher expression, more PASs, and slightly longer terminal 3′ UTRs than excluded orthologs (14,436 and 15,341), alongside a slightly lower share of single-terminal-3′-UTR full PAS axes (Figure S24c–f, Table S10g). Design-wide endpoint expression medians were 54.3–92.8 versus 5.0–6.5 CPM (SMD = 1.70–2.14 on $\log_2(1 + \text{CPM})$, with overlapping distributions, no uniform cutoff, and 401 human and 425 mouse excluded genes lacking a feature in at least one study). Study-median primary-catalog PAS counts were 4.0–5.5 versus 1.5–2.5 (SMD = 0.97–1.11), reference-supported retained PAS counts were 3.5–4.0 versus 1.0–1.5 (SMD = 1.14–1.28), and Ensembl release 116 longest annotated terminal 3′ UTR medians were 2,062–2,497 versus 1,621–1,880.5 nt (SMD = 0.16–0.30, with 637 human and 694 mouse genes lacking an annotated coding terminal UTR). Conversely, single-terminal-3′-UTR containment of evaluable full primary PAS axes was 3.0–7.8 pp lower in retained orthologs (26.2%–35.9% versus 31.5%–38.8%, with 0.24%–0.53% versus 27.9%–40.9% lacking an evaluable annotated full axis). Because full-axis containment is stricter than the switching-pair tandem definition in Figure 3c (315/751 P–M pairs), this difference does not alter the tandem enrichment in Figure 3c. Cross-species conclusions nevertheless remain restricted to the jointly measurable backgrounds.

Candidate-level retention and descriptive prioritization. Among the 27 shared proximal P–M pairs at $|\Delta\text{DWUI}| \geq 0.02$, 11 retained cross-species recurrence under both marker-defined human M and alternative PAS calling. At the stricter $|\Delta\text{DWUI}| \geq 0.05$ threshold, 2 of the 7 shared proximal P–M pairs (*PDLIM7/Pdlim7* and *EIF4EBP2/Eif4ebp2*) and 1 of the 4 shared distal P–S pairs (*ZNF655/Zfp655*) held across all applicable sensitivity checks. Across all 43 unique ortholog pairs (44 ortholog–contrast entries and 1,900 candidate-by-threshold evaluations in Table S10c), no candidate switched to opposite-direction recurrence under any condition. By the five-criterion ranking (Section S1.11), 10 entries (9 pairs, led by *PDLIM7/Pdlim7* and *EIF4EBP2/Eif4ebp2*) fell in Tier 1, 7 fell in Tier 2 and 26 fell in Tier 3 (9 unevaluable only and 17 losing recurrence in at least one condition), alongside the unranked local-interval example *RIOK3/Riok3* (per-candidate thresholds, structural features, expression percentiles and lower-cycle-half P metrics in Table S10c).

S3. Supplementary figures

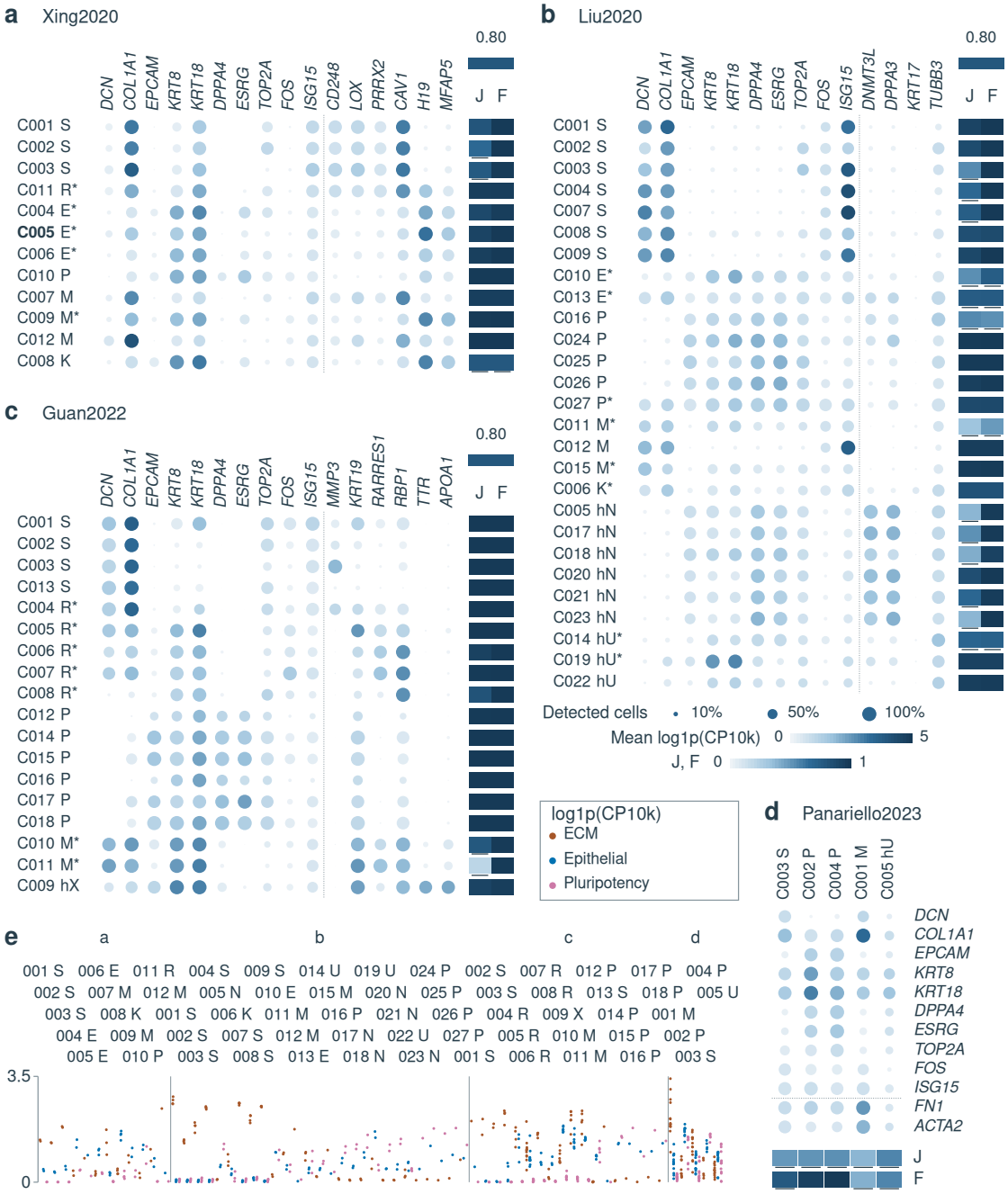

Figure S1. Human study-local expression states: native marker evidence, partition stability and program scores.

State-code meanings (S, source-like or fibroblast; R, source-exit or remodeling; E, epithelial or mixed-transition; P, pluripotency-acquisition; M, mesenchymal or ECM-retaining; K, keratin-related candidate; hN, human naive-related candidate; hX, human endoderm-secretory; hU, human mixed or unresolved) denote display families rather than matched cell identities or a mandatory state sequence.

a–d, Xing2020, Liu2020, Guan2022 and Panariello2023. Ten core markers shared across panels precede the dotted rule, followed by study-local markers. States are rows in a–c and columns in d, and the shared area and color keys below b apply to a–d. Dot area encodes the detected-cell fraction and color encodes mean per-cell log1p(CP10K) (where CP10K is counts per 10,000) from native counts, with equal library weights across libraries containing ≥ 20 cells in the state (or all libraries otherwise).

Value bands (paired columns in a–c with a 0.80 reference swatch above each pair, and upper and lower bands in d) encode the median best-cluster Jaccard overlap (J) and median display-family compatibility (F) across nine fixed-graph partitions (three neighboring resolutions $\times$ three seeds) on a common 0–1 color scale, with dark underlines marking values below 0.80. Bold state labels mark boundary states, and asterisks mark candidate or mixed states.

e, Native extracellular-matrix (ECM, brown, left slot), epithelial (blue, middle slot), and pluripotency (pink, right slot) program scores (mean log1p(CP10K) on a shared 0–3.5 axis) for all 206 qualified library $\times$ state observations ($\geq$ 20 cells), with small horizontal offsets separating libraries within each program slot. Columns show the human study-local states from a–d grouped by study, and five interleaved label rows pair each three-digit native state ID (common C prefix omitted) with its display-family code (N, X and U denote hN, hX and hU). State identities and the expression framework were fixed before the PAS analysis. See Supplementary Methods Section S1.2, Supplementary Results Section S2.1 and Supplementary Table S1a for full numerical summaries.



Figure S2. Mouse study-local expression states: native marker evidence, partition stability, program scores and within-library contrasts of three boundary states.

State-code meanings (S, source-like or fibroblast; R, source-exit or remodeling; E, epithelial or mixed-transition; P, pluripotency-acquisition; M, mesenchymal or ECM-retaining; K, keratin-related candidate; mB, trophoblast-like; mN, neural or neurokeratin; mI, interferon-high transition; mY, myeloid-local; mU, unresolved) denote display families rather than matched cell identities or a mandatory state sequence.

a–d, Schiebinger2019–2i (**a**), Guo2019–OSK (**b**), Jaber2022 (**c**, where G3 and O3 denote day-3 GETM and OSKM, and D6 and D12 denote pooled sampling days) and Guo2019–CIP (**d**). Ten core markers precede the dotted rule, followed by study-local markers (shared key at bottom right). Dot area encodes the detected-cell fraction and color encodes mean log1p(CP10K) (where CP10K is counts per 10,000) from native counts with equal library weights ($\geq$ 20 cells per state, else all libraries). Aligned stability axes (0.5–1.0, dotted reference at 0.80) show nine-partition medians of J (filled circles) and

F (open circles, or a filled center in an open circle when coincident). Bold labels identify boundary states, asterisks identify candidate or mixed states, and the dagger identifies L11 (< 20 cells in every library).

e, Within-library target-minus-reference program scores for Schiebinger2019–2i L00 against L03 and L06 (upper, AUCell, $n = 29$ libraries) and Xing2020 C005 against C004 and C006 (lower, fixed human modules from Figure S1e, mean log1p(CP10K), $n = 1$ eligible library), each with its own zero reference (open circles, individual libraries; horizontal dark ticks, medians; blank columns, programs not in that contrast).

f, Native ECM (left), epithelial (middle), and pluripotency (right) scores (log1p(CP10K)) across all 353 qualified library $\times$ state units (≥ 20 cells) in 48 mouse states (2i, Schiebinger2019–2i; OSK, Guo2019–OSK; CIP, Guo2019–CIP; D6/D12, two day-6 followed by two day-12 columns; L11 dagger retained without marks). Short lines connect the three scores of the same library, and colors and the aligned strip encode display family.

g, Within-library AUCell differences for Guo2019–CIP C012 against C008, C009 and C011 across all four eligible libraries (open circles, libraries; vertical dark ticks, medians; Source/ECM, fibroblast and extracellular-matrix retention). See Supplementary Methods Section S1.2, Supplementary Results Section S2.1 and Supplementary Tables S1a and S1h for full numerical summaries.

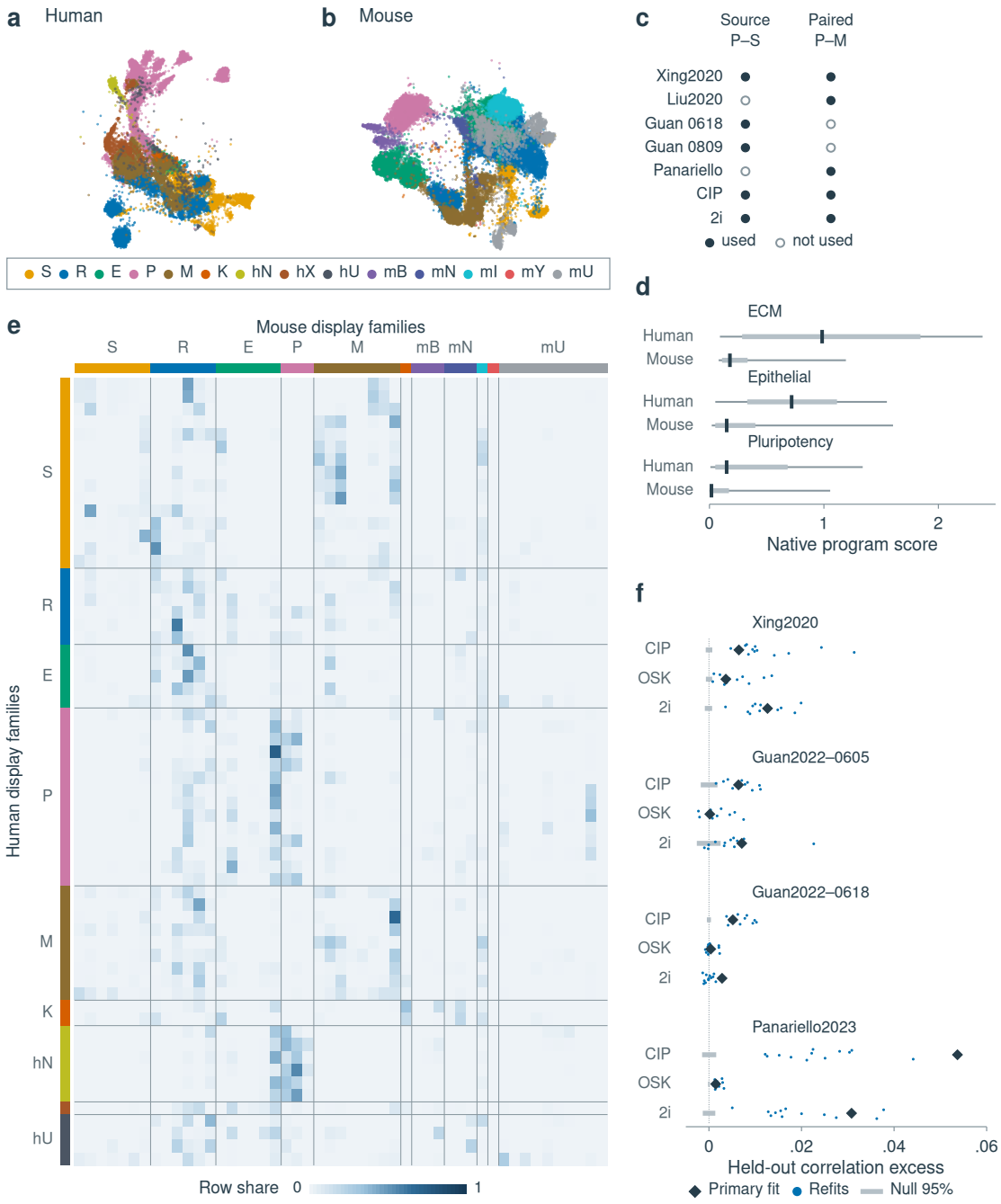

Figure S3. Expression-state framework and comparison availability.

State-code meanings (S, source-like or fibroblast; R, source-exit or remodeling; E, epithelial or mixed-transition; P, pluripotency-acquisition; M, mesenchymal or ECM-retaining; K, keratin-related candidate; hN, human naive-related candidate; hX, human endoderm-secretory; hU, human mixed or unresolved; mB, mouse trophoblast-like; mN, mouse neural or neurokeratin; mI, mouse interferon-high transition; mY, mouse myeloid-local; mU, mouse unresolved) denote display families, and the common family key below a and b also applies to the strips in e.

a, b, Joint expression embeddings of the human (23,246 cells) and mouse (36,754 cells) parts of the 60,000-cell display subsample, colored by display family without recomputing embeddings or annotations.

c, Studies and series available for documented-source P–S and paired P–M designs (Guan 0618 and 0809, Guan2022 donor-specific series; Panariello, Panariello2023; CIP, Guo2019–CIP; 2i, Schiebinger2019–2i).

d, Native program scores per species and program across qualified library × state observations ($\geq$ 20 cells; vertical ticks, medians; thick segments, interquartile ranges; thin segments, 10–90% ranges).

e, Row-normalized cross-species edge weights across all 62 × 49 human–mouse state-pair combinations (human states in rows, mouse states in columns, ordered by display family with zero weights retained).

f, Held-out expression correlation excess (observed correlation minus its null mean) across the 12 human × mouse route pairs for primary fits (diamonds), full refit variants (blue dots, 142 evaluable refits shown and two zero-variation refits retained in the denominator of 12 refits per route pair) and primary-fit null 2.5th–97.5th percentile ranges relative to the null mean (gray segments; CIP and OSK, Guo2019; 2i, Schiebinger2019). See Supplementary Methods Sections S1.1 and S1.2, Supplementary Results Section S2.1 and Supplementary Tables S1a and S3a for full numerical summaries.

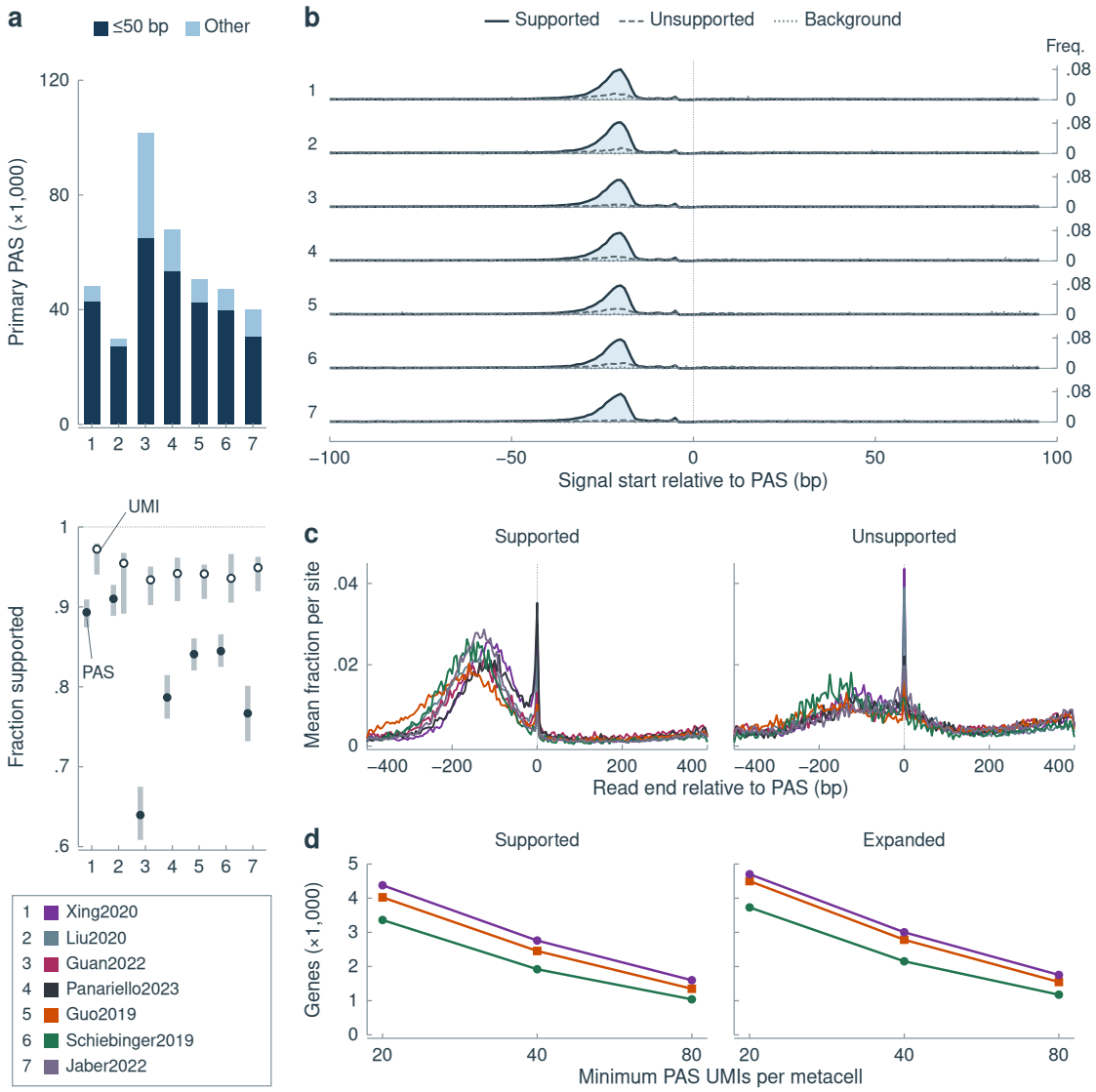

Figure S4. PAS measurement support relative to the integrated reference.

State codes follow Figures S1–S3. The integrated reference combines PolyASite v2.0, PolyA_DB v4.1 and GENCODE (Section S1.3).

a, Primary PAS counts per study (top; Table S2a), split into sites supported within 50 bp and other primary PASs, with PAS (filled circles) and UMI (open circles) support fractions at ±50 bp and matching-window sensitivity bars spanning ±25 to ±100 bp on the lower axis (dotted line at 1; shared study key).

b, Canonical polyadenylation-signal start frequencies in transcript orientation by study row on shared position and frequency axes for supported primary PASs (solid lines and shaded areas), unsupported primary PASs (dashed lines) and matched genomic backgrounds (dotted lines; vertical dotted line marks the PAS).

c, Mean per-site read-end fractions around supported and unsupported primary PASs, colored by study.

d, Genes with complete S–R–E–P profiles in Schiebinger2019–2i, Guo2019–CIP and Xing2020 at minimum gene-level PAS thresholds of 20, 40 and 80 UMIs per metacell in the supported and expanded layers. See Supplementary Methods Section S1.3, Supplementary Results Section S2.1 and Supplementary Table S2a for full numerical summaries.

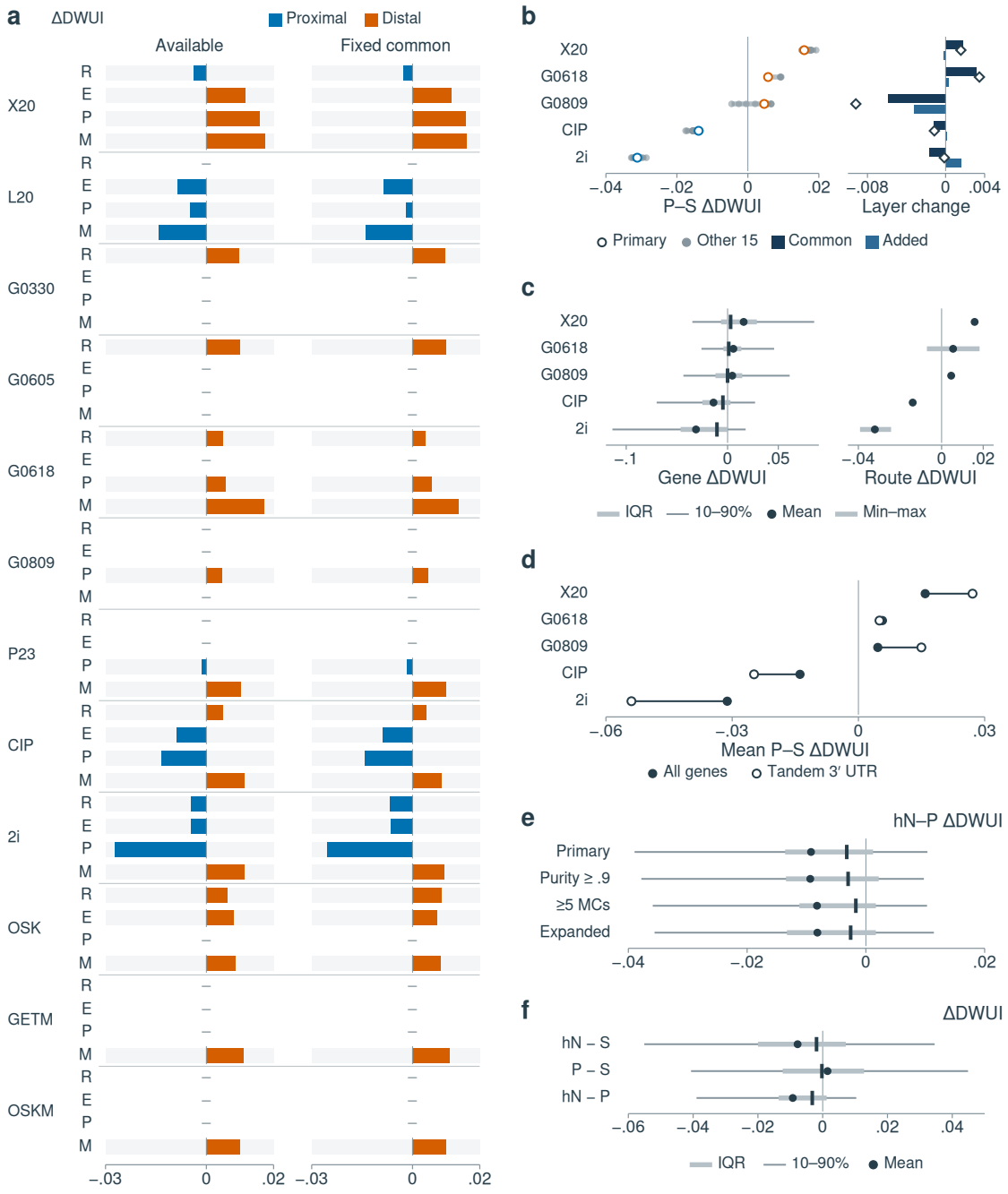

Figure S5. Route means, tandem-3′ UTR restriction and state-reference sensitivity.

State codes follow Figures S1–S3. Here and in subsequent figures, ΔDWUI is the target-minus-reference change in distance-weighted PAS usage index (negative, proximal shift; Section S1.4). Route abbreviations are X20 (Xing2020), L20 (Liu2020), G0330 (Guan2022–0330), G0605 (Guan2022–0605), G0618 (Guan2022–0618), G0809 (Guan2022–0809), P23 (Panariello2023), CIP (Guo2019–CIP), 2i (Schiebinger2019–2i), OSK (Guo2019–OSK), GETM (Jaber2022–GETM D3) and OSKM (Jaber2022–OSKM D3).

a, Route mean ΔDWUI of R, E, P and M relative to observed S for all available genes (left) and the route-specific fixed common background (right, $n = 898$–$6,452$ genes across the 12 routes; bars from zero, means; blue, proximal; orange, distal; dash, unobserved state or unavailable S reference).

b, Left, documented-source P–S route mean ΔDWUI across the five routes under 16 settings (four PAS settings × four gene backgrounds; open circles, primary setting in orange for distal and blue for proximal; gray points and bars, other 15 settings and full min–max range). Right, supported-to-

expanded change in each route mean split into re-estimation on common genes (upper dark-blue bar), newly admitted expanded-layer genes (lower light-blue bar) and their sum (open diamond). Routes follow the same order in b–d.

c, Left, gene-level P–S ΔDWUI at the primary setting (points, means; dark ticks, medians; thick bars, interquartile ranges, IQR; thin bars, 10–90% ranges). Right, route means across 3–6 source-library and gene-background configurations per route (circles, medians of configuration means; bars, min–max ranges).

d, Mean P–S ΔDWUI for all eligible genes (filled circles, $n = 2,780$–$5,826$) and strict tandem-3′ UTR genes (open circles, $n = 686$–$1,565$).

e, f, Within-library ΔDWUI in the Liu2020 RSeT library (GSM4546548) across four settings for hN–P (**e**; primary setting, purity ≥ 0.9, ≥ 5 metacells per group (MCs), and expanded layer; $n = 459$, 454, 307 and 515 genes measurable across all three edges) and across all three edges ($\mathrm{hN} - \mathrm{S} = (\mathrm{hN} - \mathrm{P}) + (\mathrm{P} - \mathrm{S})$) at the primary setting on the same 459 genes (**f**; symbols as in c, shared key below f). See Supplementary Methods Section S1.4, Supplementary Results Section S2.1 and Supplementary Tables S2b, S2c and S2e for full numerical summaries.

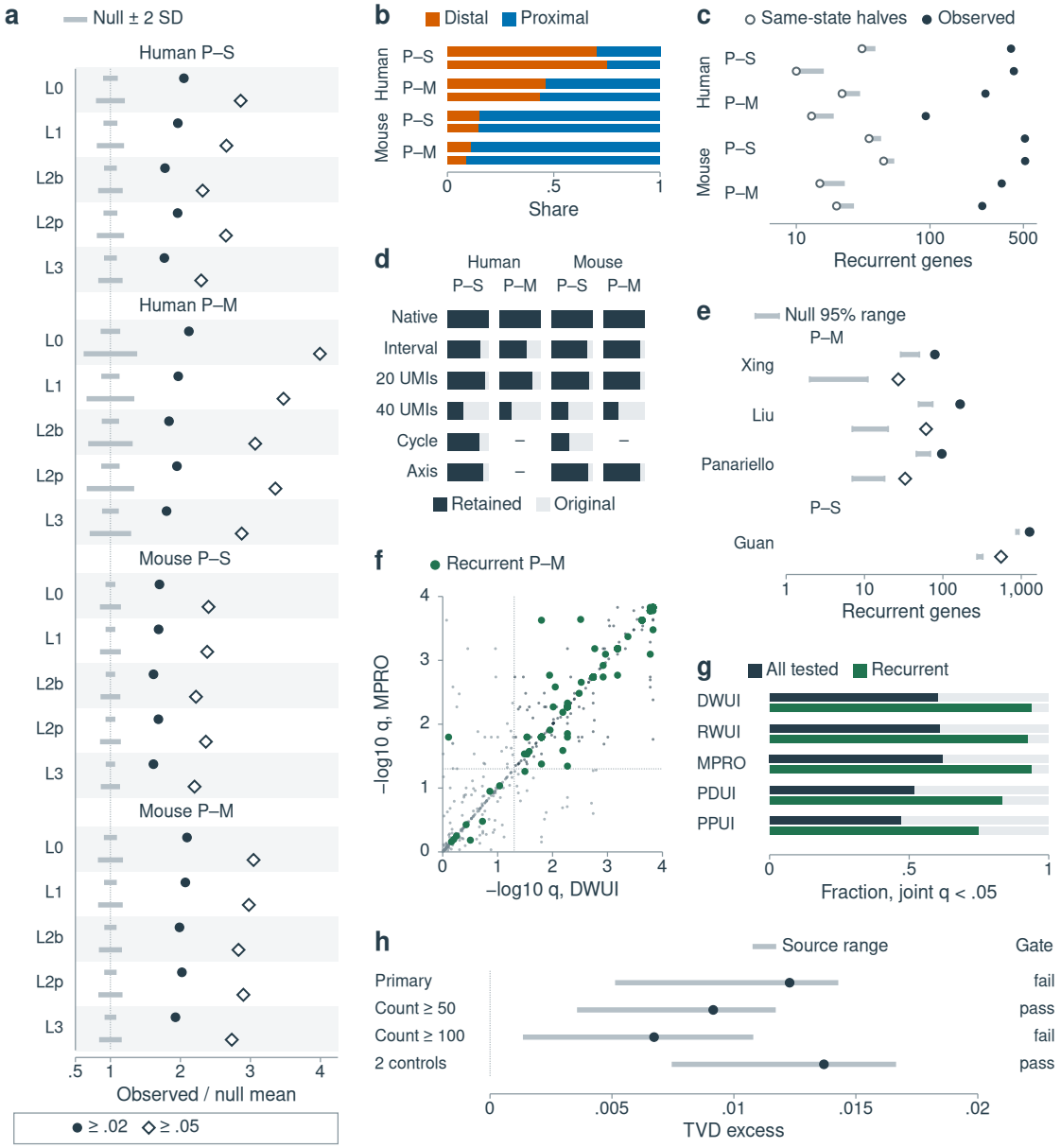

Figure S6. Within-species recurrence, its robustness, and well-level and external checks.

State codes follow Figures S1–S3. Panels a–e use ΔDWUI (negative, proximal; labeled WPP in source tables; Section S1.6), and MPRO is the unsigned range of PAS-proportion changes. Filled circles and open diamonds in a and e denote $|\Delta\text{DWUI}| \geq 0.02$ and ≥ 0.05 (shared key in a).

a, Recurrence enrichment (observed/null-mean count, ±2 standard deviations [SD]) under five nested nulls (L0, feasible series; L1, plus expression and coverage; L2b, plus reference position; L2p, plus PAS number; L3, full matched null) at $|\Delta\text{DWUI}| \geq 0.02$ and ≥ 0.05 (dotted line at 1; all 40 tests $q < 0.001$).

b, Distal and proximal shares of recurrent genes at $|\Delta\text{DWUI}| \geq 0.02$ (upper thick bars; $n = 483$, 268, 604 and 420 for human P–S, human P–M, mouse P–S and mouse P–M) and ≥ 0.05 (lower thin bars; $n = 201$, 89, 265 and 225).

c, Observed recurrence (filled circles, log scale) versus split-half within-state pseudo-recurrence (open circles, medians; gray segments, median to 95th percentile) for target (upper) and reference (lower) states.

d, Same-direction retention of the $|\Delta\text{DWUI}| \geq 0.02$ recurrent sets (gray tracks, original sets; dark bars, retained genes; dash, < 2 studies) across six variants: Native, Interval (bootstrap interval excluding zero), 20 UMIs, 40 UMIs, Cycle and Axis.

e, Observed recurrent counts (log scale) versus 95% null ranges for leave-one-study-out human P–M (upper six rows, named by omitted study) and human P–S splitting Guan2022 series (lower two rows).

f, g, Well-level sign-flip inference across $n = 614$ genes in Schiebinger2019–2i (BH-corrected over five metrics $\times$ 614 genes; dotted lines at $q = 0.05$), showing $-\log_{10} q$ for DWUI versus MPRO (**f**; green, $n = 143$ tested recurrent mouse P–M members; dark non-green, other genes passing both thresholds, $n = 351$ total; pale, remaining genes) and fractions passing $q < 0.05$ across all 614 and 143 recurrent genes for DWUI, rank-weighted usage index (RWUI), MPRO, and distal or proximal PAS usage (PDUI and PPUI; gray tracks include non-passing genes; **g**).

h, External PAS-seq iPSC–MEF contrasts across four matching settings ($n = 245/276$, $203/252$, $131/201$ and $263/276$ matched/measurable candidates for Primary, Count ≥ 50, Count ≥ 100 and 2 controls), showing median total-variation-distance (TVD) excess over controls, source-choice ranges, and balance gate outcomes (pass or fail; $\geq$ 80% retention, $|\text{SMD}| \leq 0.20$). See Supplementary Methods Section S1.6, Supplementary Results Section S2.2 and Supplementary Tables S3a–S3d for full numerical summaries.

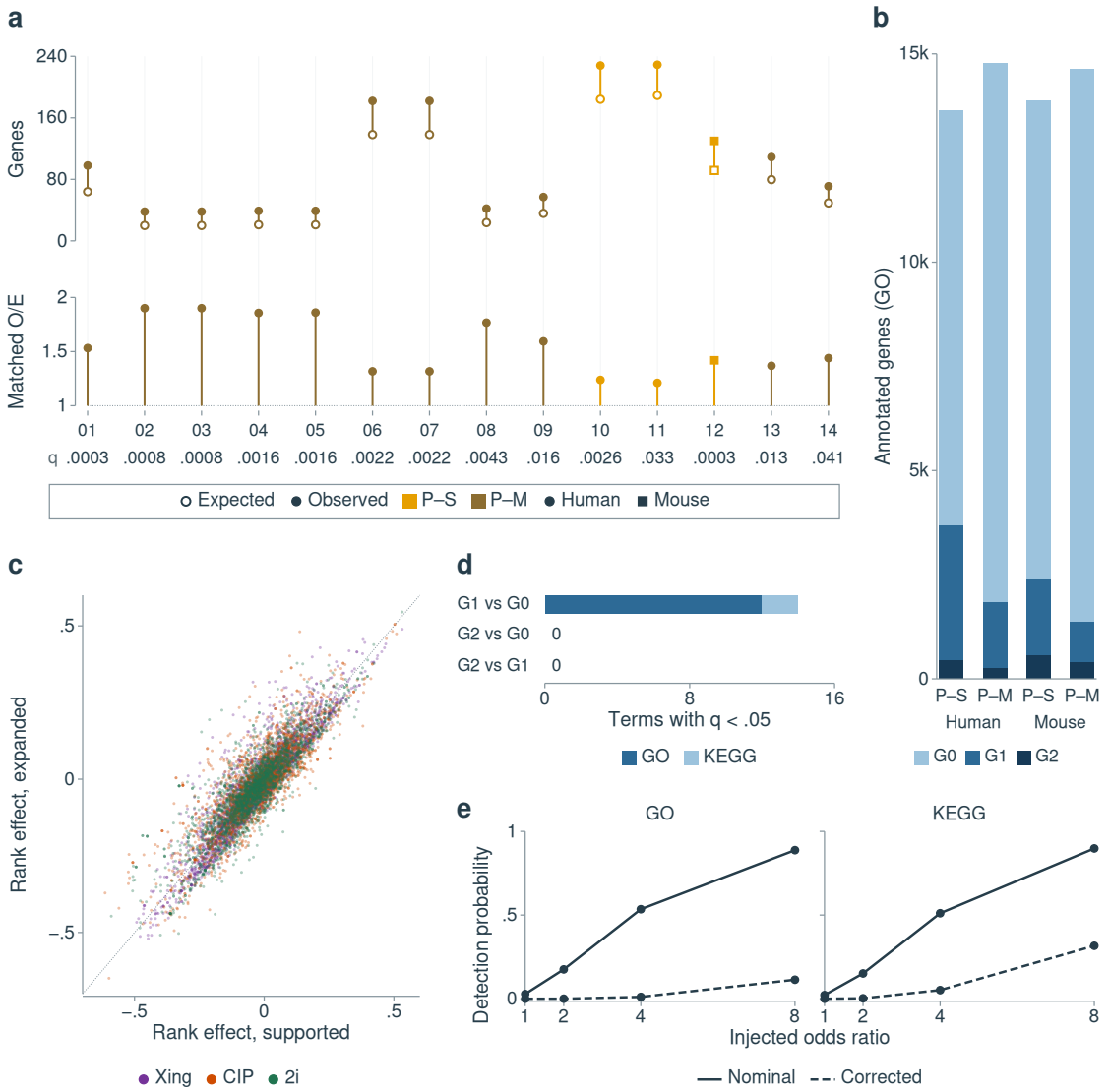

Figure S7. Functional enrichment of the recurrence sets.

State codes follow Figures S1–S3. ΔDWUI is target minus reference (negative, proximal; Sections S1.5 and S1.6).

a, The 14 significant APA-testable (G1) versus expressed (G0) terms ($q < 0.05$), colored by contrast (P–S, P–M) with circles for human and squares for mouse: expected (open) and observed (filled) gene counts (upper), matched observed/expected ratios relative to 1 (lower), and q values beneath column numbers 01–14. Term identities are 01, cytoplasmic translation (GO:0002181), 02, negative regulation of syncytium formation by plasma membrane fusion (GO:0034242), 03, negative regulation of myoblast fusion (GO:1901740), 04, regulation of syncytium formation by plasma membrane fusion (GO:0060142), 05, regulation of myoblast fusion (GO:1901739), 06, translation (GO:0006412), 07, protein biosynthetic process (GO:0160307), 08, striated muscle contraction (GO:0006941), 09, muscle system process (GO:0003012), 10, intracellular protein transport (GO:0006886), 11, mitotic cell cycle process (GO:1903047), 12, regulation of mRNA metabolic process (GO:1903311), 13, Ribosome (hsa03010), and 14, Coronavirus disease (hsa05171).

b, Nested GO-annotated gene backgrounds per species and contrast sharing a zero baseline: expressed genes (G0), APA-testable genes (G1), and recurrent genes (G2).

c, Rank-biserial correlation comparing the S–R–E–P DWUI range of term members with that of other complete-profile genes in the supported versus expanded layer across all $n = 7,780$ tested GO and KEGG terms ($r = 0.89$, unclipped, dotted line of equality).

d, Number of BH-corrected discoveries ($q < 0.05$) under the L3 stratified null for G1 against G0 (22,728 tests, 14 discoveries: 12 GO terms and 2 KEGG pathways), G2 against G0 (68,184 tests, 0 discoveries) and G2 against G1 (24,354 tests, 0 discoveries).

e, Conditional-injection detection probability of the L3 G2 tests (median over GO and KEGG terms; solid lines, nominal; dashed lines, Bonferroni-corrected) against injected odds ratio (Xing, Xing2020; CIP, Guo2019–CIP; 2i, Schiebinger2019–2i). See Supplementary Methods Sections S1.5 and S1.6, Supplementary Results Sections S2.2 and S2.8, and Supplementary Tables S3f and S8c for full numerical summaries.

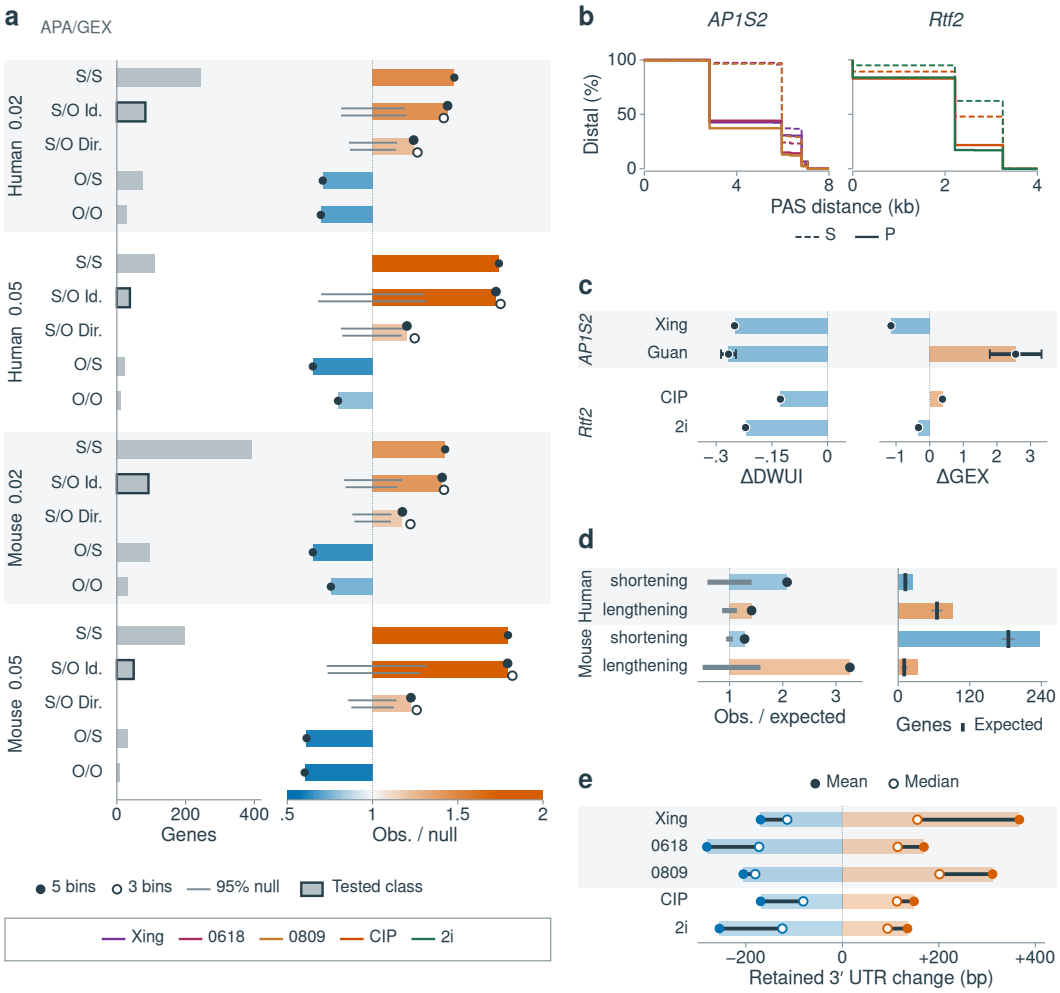

Figure S8. APA–GEX response identity and direction, and strict tandem-3′ UTR length changes. State codes follow Figures S1–S3. ΔDWUI is P minus S (negative, proximal; Section S1.6), and ΔGEX is the difference in mean $\log_2(\mathrm{CPM}+1)$ (CPM, counts per million).

a, Cross-study APA–GEX relation classes (first code APA, second code GEX: S, same direction across all series of both studies; O, opposite directions; requiring $|\Delta\mathrm{GEX}| \geq 0.25$ and $|\Delta\mathrm{DWUI}| \geq 0.02$ or 0.05) across $n = 3{,}606$ human and $2{,}312$ mouse co-measured genes. Left, four-class gene counts (outlined bars mark the tested SO class, APA same and GEX opposite). Right, observed/null-mean enrichment ratios relative to 1 (bar and axis-strip colors encode $\log_2$(observed/null mean) clipped at ± 0.8, point positions unclipped) under the response-identity (Id.) and direction-specific (Dir.) nulls using five (filled circles) or three (open circles) baseline bins, with gray bars showing the two single-study shuffled 2.5–97.5% five-bin null ranges (all eight prespecified tests $q_8 < 0.05$).

b, c, Distal PAS usage (%) in S (dashed) and P (solid) versus distance from the proximal PAS (**b**) and matched ΔDWUI and ΔGEX (**c**; blue, negative; orange, positive) for human *AP1S2* (Xing, Xing2020; Guan, Guan2022 study value with 0618–0809 series range bar) and mouse *Rtf2* (CIP, Guo2019–CIP; 2i, Schiebinger2019–2i).

d, Documented-source P–S recurrence ($|\Delta\mathrm{DWUI}| \geq 0.02$) on strict tandem-3′ UTR genes ($n =$ 580 human and 670 mouse measurable genes) for shortening (proximal) and lengthening (distal) against the stratified measurement-matched null (10,000 permutations, all four tests $q_8 = 0.00013$): observed/expected ratios (circles) with 95% permutation ranges (gray bars, left), and observed recurrent gene counts (bars), analytic expected counts (vertical ticks) and 95% permutation ranges (gray bars, right).

e, Usage-weighted change in retained 3′ UTR length (bp; filled circles, means; open circles, medians; blue, shortening; orange, lengthening) in each documented-source series (Xing, Xing2020; 0618 and 0809, Guan2022–0618 and –0809; CIP, Guo2019–CIP; 2i, Schiebinger2019–2i). See Supplementary Methods Section S1.6, Supplementary Results Section S2.2 and Supplementary Tables S3e, S3g and S3h for full numerical summaries.

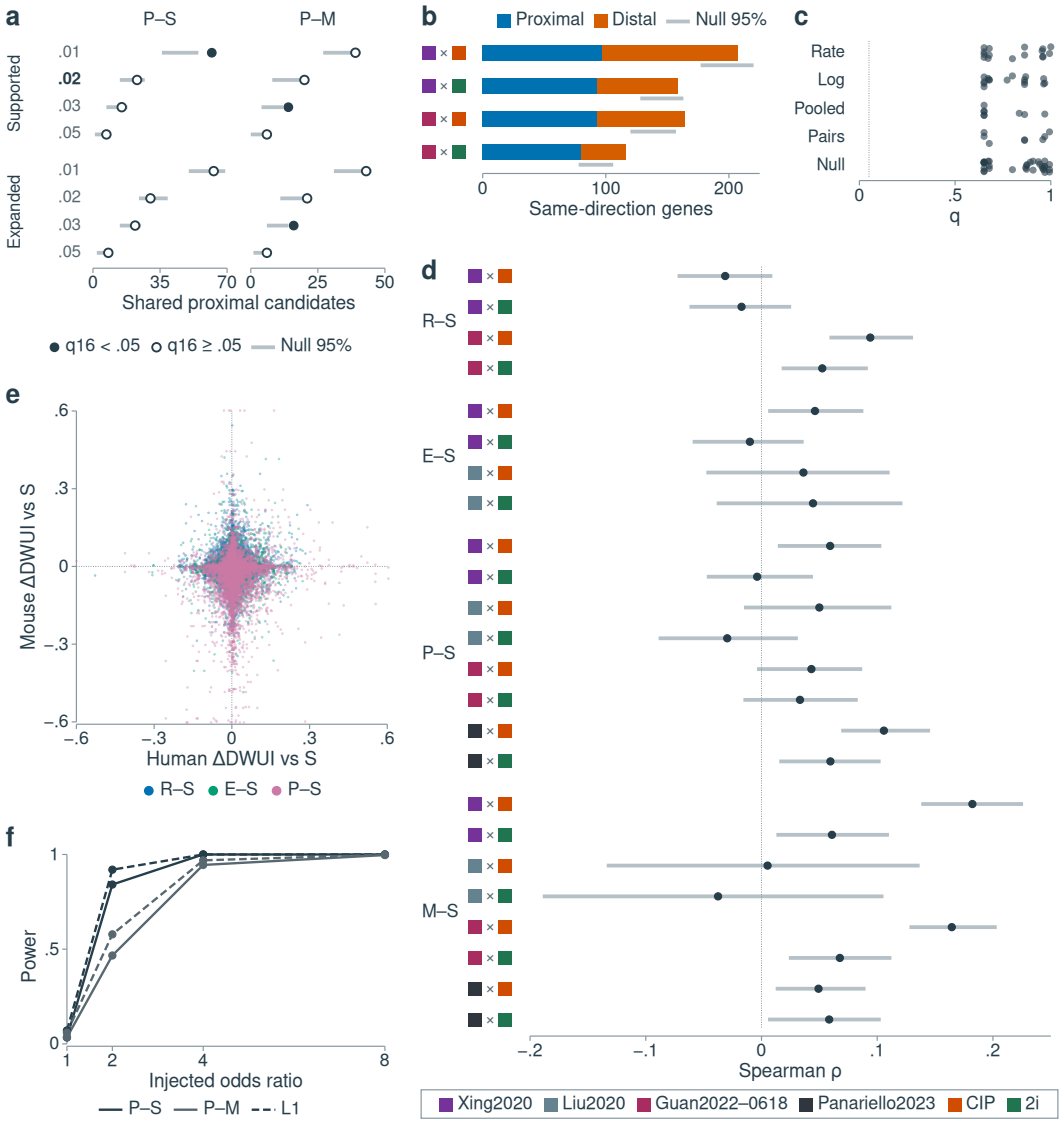

Figure S9. Cross-species sharing: threshold and layer sensitivity, direction, and continuous correspondence.

State codes follow Figures S1–S3. ΔDWUI is target minus reference (negative, proximal; Section S1.9).

a, Shared proximal candidates for observed-S P–S and paired P–M against the joint measurement–PAS null (95% range) across four $|\Delta\text{DWUI}|$ thresholds (bold 0.02, primary threshold) in the supported and expanded layers, with BH q_{16} over the 16 settings.

b, Same-direction gene counts ($|\Delta\text{DWUI}| \geq 0.02$, split into shared proximal and shared distal) for the four human × mouse study pairs (Guan2022 requiring agreement across series) against the 95% range of the primary five-quintile source-DWUI sharing null (labeled Q5).

c, Complete-family BH q values across all 80 direction-difference tests: excess-rate (Rate), log-enrichment (Log), pooled-gene (Pooled), between-pair (Pairs), and pair-specific null (Null) tests (minimum $q = 0.65$).

d, Cross-species Spearman ρ with ortholog-block bootstrap 95% intervals across all 24 study-pair × contrast combinations (R–S, E–S, P–S and M–S; Guan2022 represented by Guan2022–0618 in d and e).

e, Human versus mouse ΔDWUI relative to observed S across all $n = 30,614$ measurable gene pairs of R–S, E–S and P–S (supported layer, colored by state, values beyond ± 0.6 drawn at the limit).

f, Conditional-injection power of the cross-species sharing test against injected odds ratio for P–S and P–M under the full L3 stratified null (solid lines) and coarser L1 null (dashed lines; CIP, Guo2019–CIP; 2i, Schiebinger2019–2i). See Supplementary Methods Section S1.9, Supplementary Results Section S2.4 and Supplementary Tables S4a and S4b for full numerical summaries.

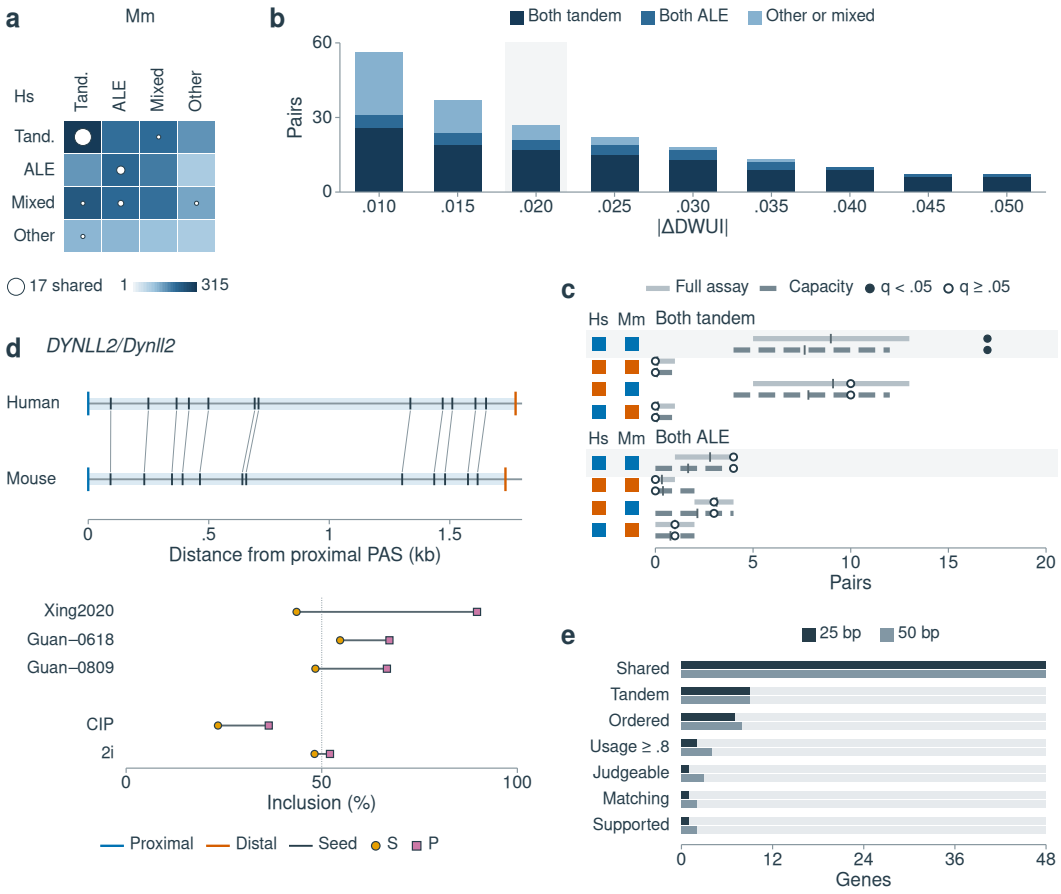

Figure S10. Event classes of the shared P–M proximal response and corresponding PAS switches. State codes follow Figures S1–S3 (Hs, human; Mm, mouse). ΔDWUI is target minus reference (negative, proximal; Section S1.9). On the background of $n = 751$ one-to-one orthologs measurable in ≥ 2 studies per species for P–M, each species was classed as tandem (Tand., switching gain/loss PAS pair in one annotated terminal 3′ UTR across all evaluable routes), alternative last exon (ALE) or other/mixed.

a, Human class against mouse class across the 751 background pairs (tile shading, log-scale background count) and the $n = 27$ shared P–M proximal orthologs at $|\Delta\text{DWUI}| \geq 0.02$ (white-circle area, largest circle = 17 pairs).

b, Event-class composition of the shared P–M proximal set across nine $|\Delta\text{DWUI}|$ thresholds from 0.010 to 0.050 ($n = 56$ down to 7 pairs; 0.020 column shaded; Both tandem, Both ALE, and other/mixed).

c, Cross-species direction pairing (squares: Hs left, Mm right; blue, proximal; orange, distal) at $|\Delta\text{DWUI}| \geq 0.02$ for Both tandem ($n = 315$ pairs) and Both ALE ($n = 52$ pairs) under the full-assay null (upper light-gray solid 95% range) and the measurement and PAS-capacity null (lower darker dashed 95% range; 100,000 permutations each; circles, observed counts, filled for $q < 0.05$; vertical ticks, expected counts).

d, *DYNLL2*/*Dynll2* P–S switch. Top, segment between the reciprocally matched (≤ 25 bp) proximal and distal PASs (1,773 bp in human, 1,731 bp in mouse) in transcript orientation showing 13 reciprocally mapped predicted miRNA seed matches across 12 position pairs. Bottom, segment inclusion in S (circles) and P (squares) across human (Xing2020, Guan–0618 and Guan–0809 for Guan2022–0618 and –0809) and mouse (CIP, Guo2019–CIP; 2i, Schiebinger2019–2i) series.

e, Filtering of the $n = 48$ same-direction shared orthologs to corresponding PAS switches at 25 bp (dark bars, retaining *DYNLL2*) and 50 bp (gray bars, retaining *DYNLL2* and *LRRC59*; stage counts in Section S2.4 and Table S4h) tolerances across successive stages: Tandem, Ordered (≥ 2 matched PASs), Usage $\geq .8$, Judgeable, Matching and Supported (≥ 2 studies per species; pale gray tracks retain the 48-gene denominator). See Supplementary Methods Section S1.9, Supplementary Results Section S2.4 and Supplementary Tables S4g and S4h for full numerical summaries.

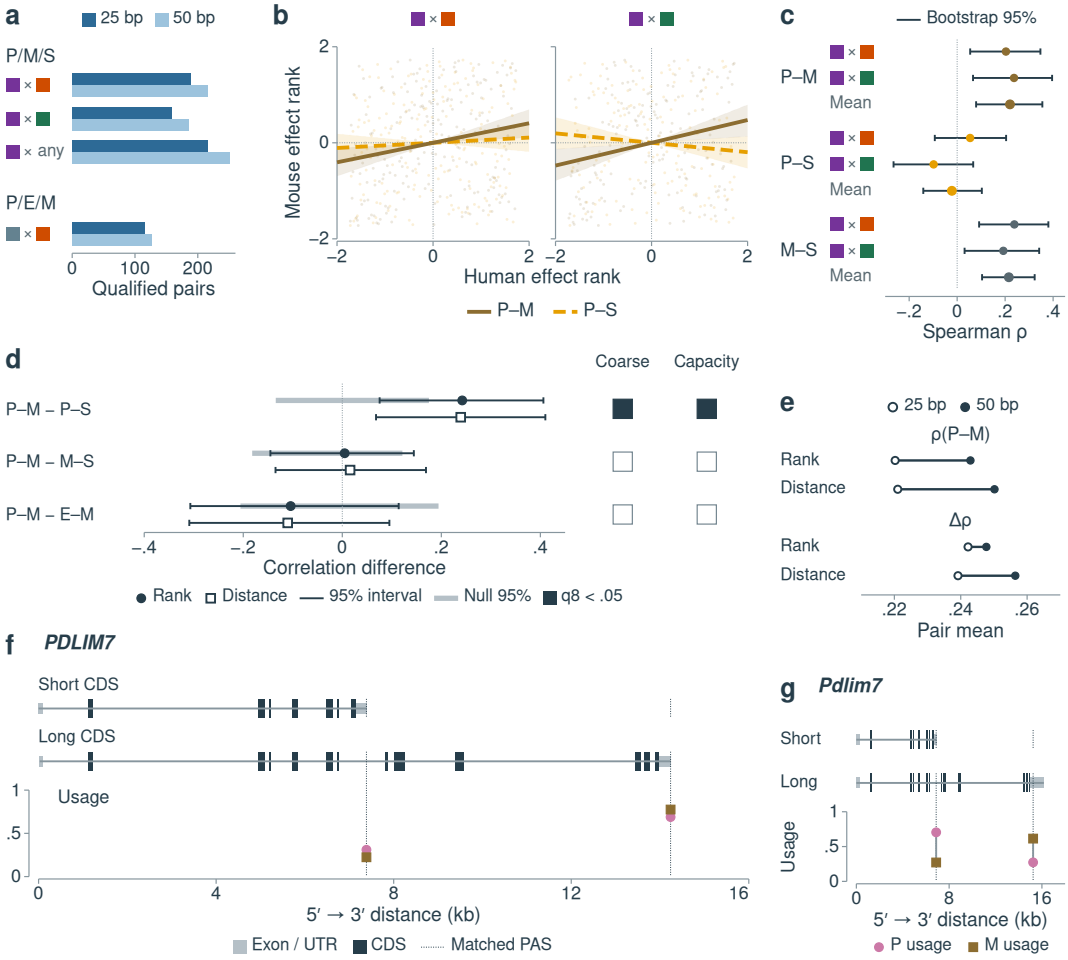

Figure S11. Same-PAS cross-species comparison on homologous PASs.

State codes follow Figures S1–S3. Homologous PASs were matched reciprocally within 25 or 50 bp with matched-site usage share ≥ 0.8 in every state (Section S1.9).

a, Qualified gene pairs at 25/50 bp tolerance for the P–M–S design (Xing2020 × Guo2019–CIP, 189/215; Xing2020 × Schiebinger2019–2i, 158/185; union for pair mean, 216/251) and the P–E–M control (Liu2020 × Guo2019–CIP, 116/126).

b, Standardized midranks of human and mouse matched-rank ΔPAS position at 25 bp ($n = 189$ and 158 genes) for P–M (solid slope line) and P–S (dashed slope line), with shaded ortholog-block bootstrap 95% intervals.

c, Per-pair and arithmetic pair-mean Spearman ρ on the rank axis (25 bp) for P–M, P–S, and M–S with ortholog-block bootstrap 95% intervals.

d, Paired correlation differences on the rank and distance axes (25 bp) with 95% bootstrap intervals and matched-null 95% ranges for the P/M/S pair-mean summaries (upper two rows) and the Liu2020 × Guo2019–CIP P/E/M control (bottom row), alongside coarse and capacity-conditioned BH q_8 tiles on the rank axis (filled, $q < 0.05$; open, $q \geq 0.05$).

e, Pair-mean ρ(P–M) and $\Delta\rho = \rho$(P–M) $- \rho$(P–S) at 25 bp (open circles, $n = 216$) and 50 bp (filled circles, $n = 251$) on the rank and distance axes (horizontal axis spanning 0.21–0.27).

f, g, Human *PDLIM7* (chr5, minus strand; ENST00000355572 and ENST00000355841) and mouse *Pdlim7* (chr13, minus strand; ENSMUST00000069968 and ENSMUST00000046246) Ensembl 116 short- and long-CDS transcript models, the two matched PASs (6.85 and 8.36 kb apart), and raw P and M usage fractions in Xing2020 × Guo2019–CIP (shared structure and usage keys below f and g). See Supplementary Methods Section S1.9, Supplementary Results Section S2.4 and Supplementary Tables S4c and S4d for full numerical summaries.

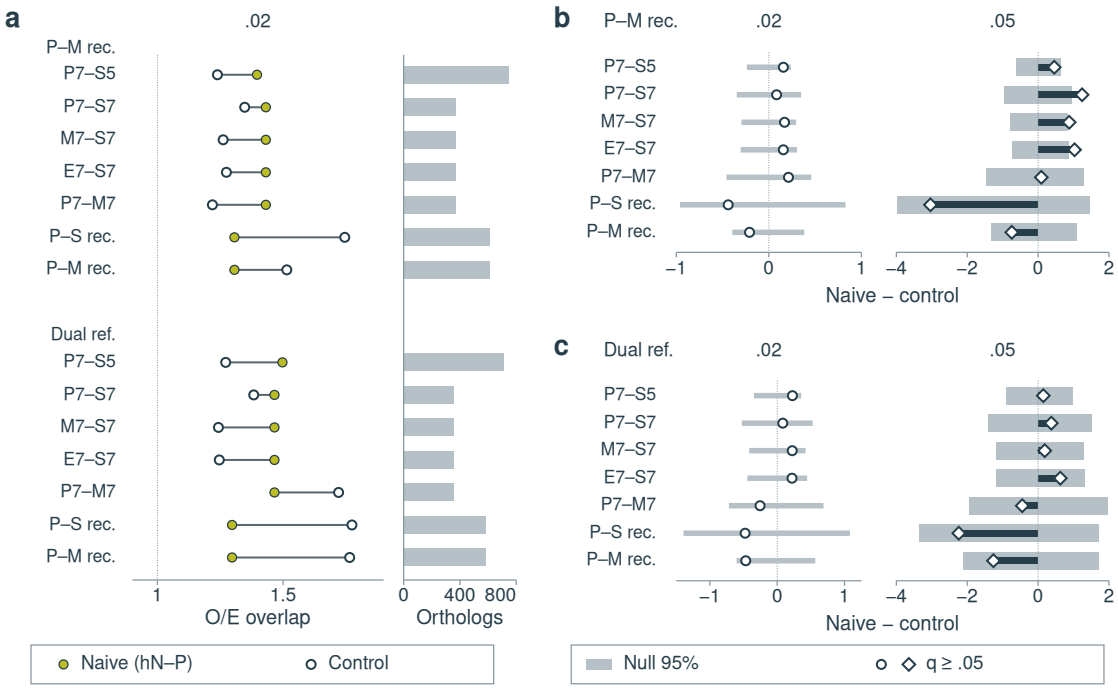

Figure S12. Specificity of the shared proximal response to naive pluripotency.

State codes follow Figures S1–S3. ΔDWUI is target minus reference (negative, proximal; Section S1.9). Each row compares proximal genes of the human naive-related contrast (equal-weight mean of N6–P7 and N8–P7 in Liu2020) against one human control (primed P7–S5 across libraries, primed P7–S7, M7–S7, E7–S7 and primed P7–M7 within P7, and the human P–S and P–M recurrent proximal sets, P–S rec. and P–M rec.) for overlap with the mouse P–M recurrent proximal set (P–M rec.) or its dual-reference subset (Dual ref., also proximal in mouse P–S) under the expression-stratified joint assay null (20,000 permutations).

a, Observed/expected overlap at $|\Delta\text{DWUI}| \geq 0.02$ for naive (filled circles) and control (open circles; vertical reference at 1), with background bars encoding eligible one-to-one ortholog counts ($n = 369$–749 for P–M rec. and 356–713 for Dual ref.).

b, c, Naive-minus-control observed/expected overlap differences at $|\Delta\text{DWUI}| \geq 0.02$ (left, open circles with gray 2.5th–97.5th percentile paired-permutation null intervals) and ≥ 0.05 (right, open diamonds with thin dark bars from zero and gray 2.5th–97.5th percentile null bands) for the mouse P–M recurrent set (**b**) and the dual-reference set (**c**; shared key below c; open symbols indicate BH $q_{14} \geq 0.05$ across all comparisons). See Supplementary Methods Section S1.9, Supplementary Results Section S2.4 and Supplementary Table S4i for full numerical summaries and row-specific q values.

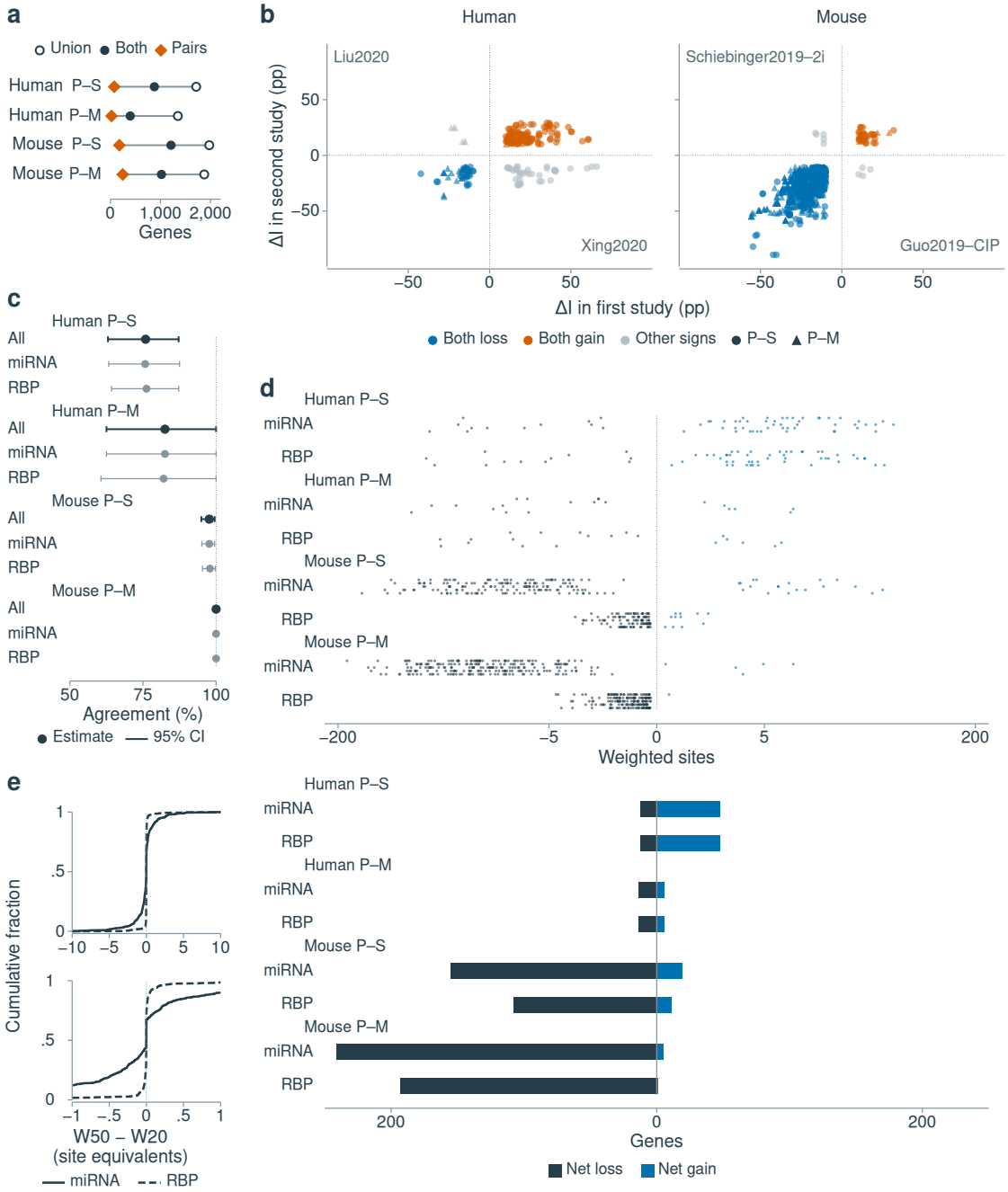

Figure S13. Recurrent interval changes and weighted predicted-site content.

State codes follow Figures S1–S3. ΔDWUI is target minus reference (negative, proximal), P–S is relative to observed S, and MPRO is the unsigned range of PAS-proportion changes (Section S1.8).

a, Gene denominators on one shared horizontal axis across human P–S, human P–M, mouse P–S and mouse P–M: union-pool genes (Union, open circles; $n = 1,713$, $1,347$, $1,974$ and $1,874$), genes measurable in both studies (Both, filled circles; $n = 878$, 396, $1,210$ and $1,020$), and genes with matched interval pairs in both studies (Pairs, diamonds; $n = 77$, 23, 179 and 246 genes contributing 170, 40, 385 and 660 pairs; Table S5a).

b, Matched-interval inclusion change (ΔI, percentage points, pp; mean of 20- and 50-UMI effects) in the two studies per species for P–S (circles) and P–M (triangles; blue, loss in both; orange, gain in both; gray, other sign combinations).

c, Fraction of matched interval pairs with the same ΔI sign in both studies at 20 UMIs, with gene-block bootstrap 95% confidence intervals for All, miRNA, and RBP categories ($n = 168$–170, 39–40, 380–385 and 657–660 pairs across the four cohorts).

d, Inclusion-weighted predicted-site change per gene, $W_{g,20} = \sum_{i \in g} n_i \Delta I_{i,20}$ (site-retention equivalents at 20 UMIs), plotted on a $\mathrm{sign}(W) \log_{10}(1 + |W|)$ axis for genes with complete sites in strictly changed intervals (upper), and counts of net-loss (ink) and net-gain (blue) genes (lower).

e, Empirical cumulative distributions of $W_{g,50} - W_{g,20}$ across $n = 500$ gene–cohort records per category for miRNA (solid) and RBP (dashed) sites over $[-10, +10]$ (upper) and zoomed to $[-1, +1]$ on the same cumulative scale (lower). See Supplementary Methods Section S1.8, Supplementary Results Section S2.5 and Supplementary Tables S5a–S5c and S6b for full numerical summaries.

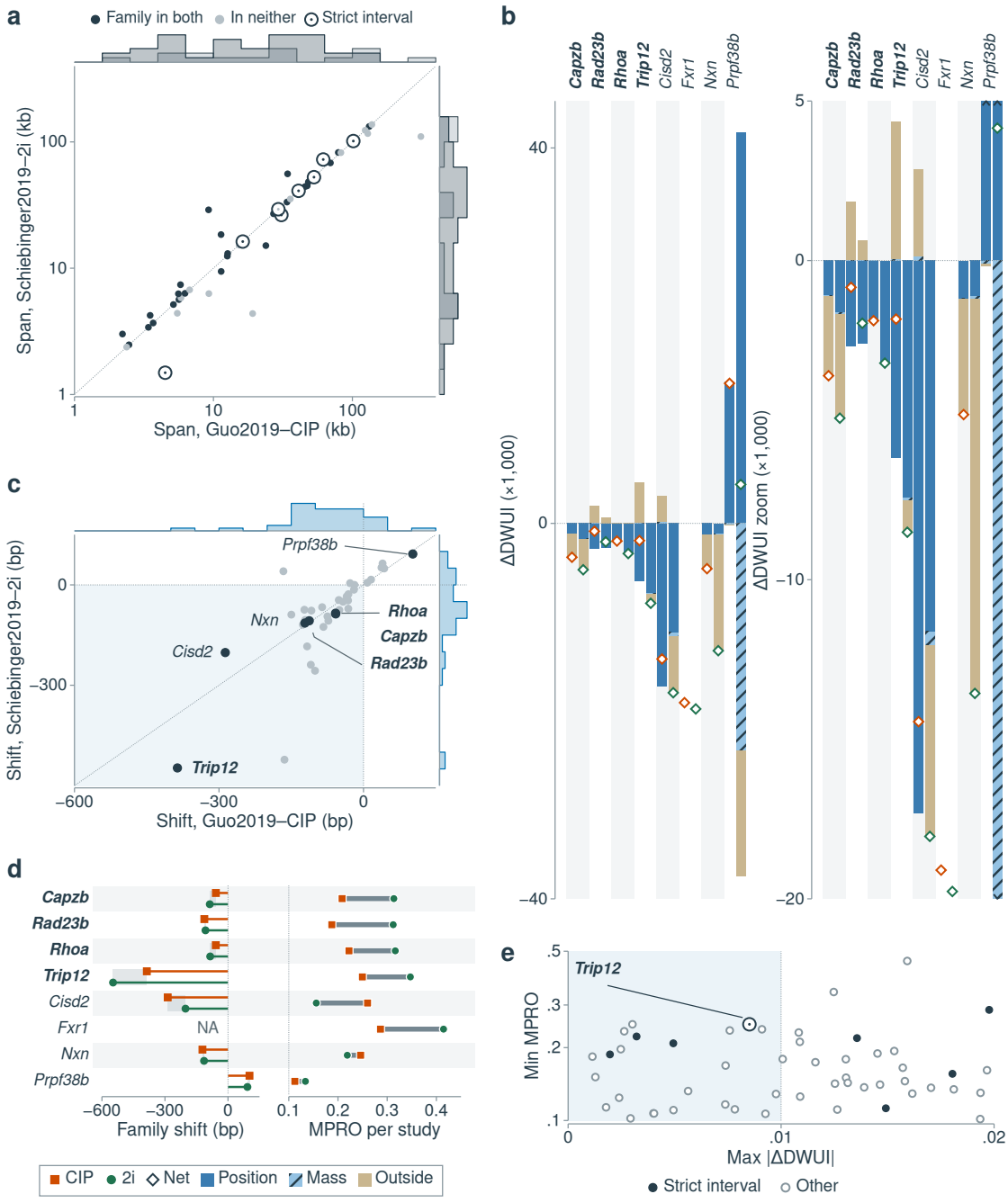

Figure S14. Axis scale, local terminal-family change and MPRO screen of the 51 low-net-shift genes.

State codes follow Figures S1–S3. ΔDWUI is P minus M (negative, proximal), and MPRO is the unsigned range of PAS-proportion changes (Section S1.8).

a, PAS-axis span of native DWUI (kb) in Guo2019–CIP and Schiebinger2019–2i across all $n = 51$ low-net-shift mouse P–M genes, with marginal step histograms, colored by terminal-family measurability in both studies (36 genes) or neither (15 genes; rings mark the 8 strict-interval genes).

b, Exact decomposition of native ΔDWUI (hollow diamonds, Net) for the 8 strict-interval genes in Guo2019–CIP (CIP, left bar) and Schiebinger2019–2i (2i, right bar) into within-family position (Position), terminal-family usage-share change (Mass, hatched), and outside-family (Outside) terms across the full range (left axis) and zoomed to $[-20, 5] \times 10^{-3}$ (right axis; arrowheads mark bars continuing beyond the zoom; bold labels mark the four genes with $|\Delta\text{DWUI}| < 0.01$ in both studies).

c, Terminal-family shift (P − M, bp) in the two studies for the $n = 36$ genes with both estimates, with marginal step histograms and strict-interval gene labels.

d, Left, per-study terminal-family shift (bp; upper and lower lollipops, CIP and 2i; gray bars, two-study range; NA for *Fxr1*, which lacks a measurable terminal family). Right, per-study MPRO (squares, CIP; circles, 2i; gray lines, two-study range; dotted line at the 0.10 threshold; shared key at bottom left).

e, Maximum $|\Delta\text{DWUI}|$ against minimum MPRO (log axis) across the two studies for all $n = 51$ genes ($|\Delta\text{DWUI}| < 0.02$ and MPRO ≥ 0.10; filled circles, 8 strict-interval genes; open circles, 43 other genes; shaded area, $|\Delta\text{DWUI}| < 0.01$ in both studies; outer ring highlights *Trip12*). See Supplementary Methods Section S1.8, Supplementary Results Section S2.5 and Supplementary Table S6b for full numerical summaries.

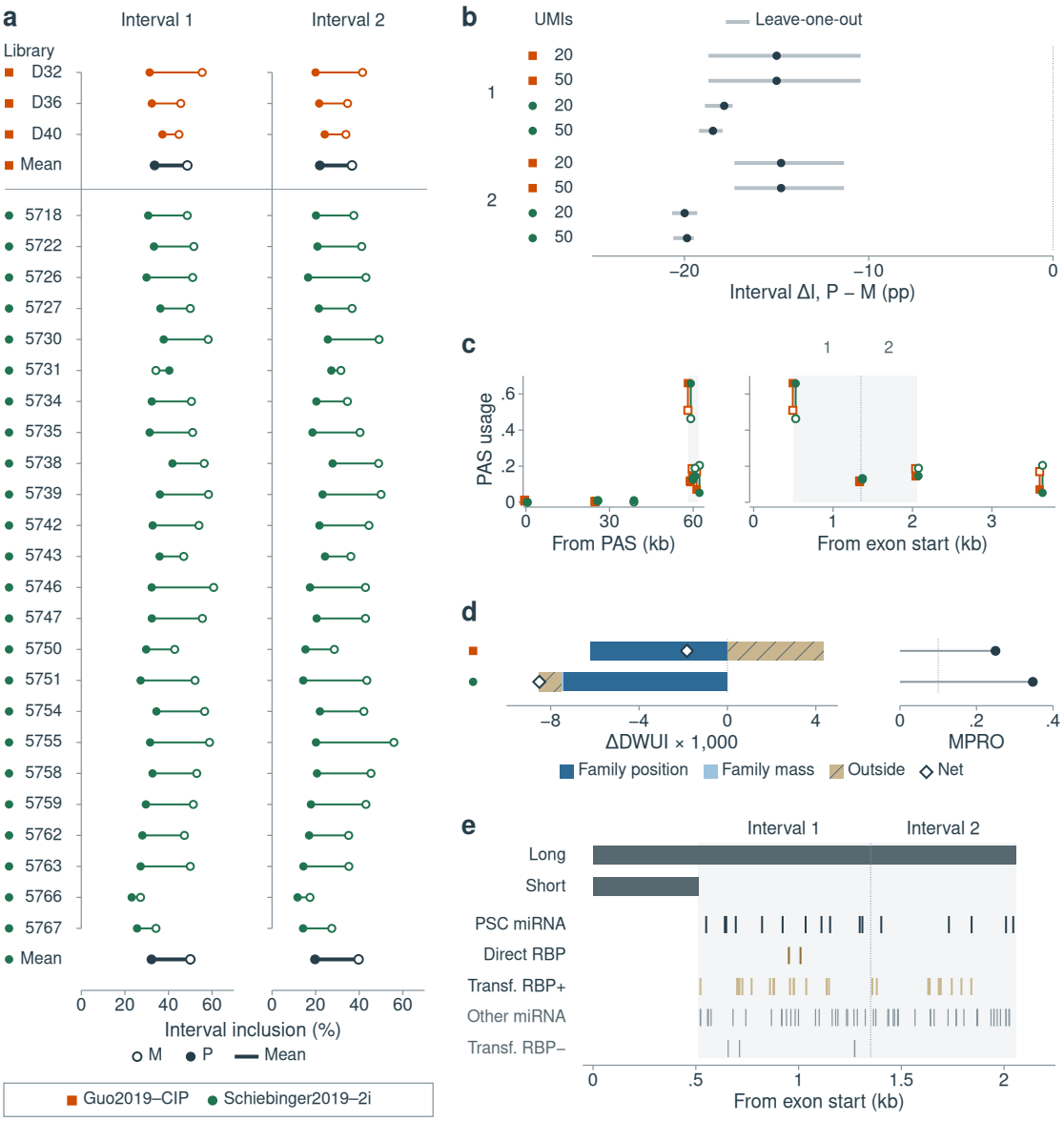

Figure S15. *Trip12*, a low-net-shift gene of Figure S14e with two strict intervals.

State codes follow Figures S1–S3 (filled and open markers in a and c indicate P and M; shared study key). ΔDWUI is P minus M (negative, proximal), MPRO is the unsigned range of PAS-proportion changes, and the two shared strict intervals are numbered from the proximal PAS (1 = 842 nt and 2 = 706 nt; Section S1.8).

a, Inclusion of strict intervals 1 and 2 in M and P of every paired library at 20 UMIs (Guo2019–CIP, $n = 3$ pairs labeled by sampling day; Schiebinger2019–2i, $n = 24$ pairs labeled by GSM319xxxx suffix; thin lines connect states within each library; bold bottom rows show study means).

b, Equal-library interval ΔI (P − M, percentage points; points) and leave-one-library-out ranges (gray bars) at 20 and 50 UMIs ($n = 3$ libraries at both thresholds in Guo2019–CIP; $n = 24$ and 20 in Schiebinger2019–2i).

c, Native PAS usage in P and M across the whole PAS axis (left, distance from the proximal PAS; shaded terminal family; 6 PASs in Guo2019–CIP and 7 in Schiebinger2019–2i) and zoomed to the terminal family (right, distance from the terminal-exon start; shaded strict intervals 1 and 2).

d, Exact decomposition of native ΔDWUI × 1,000 (open diamonds, Net) into within-family position, terminal-family mass (Family mass), and outside-family (hatched) terms ($n = 3$ and 5 contributing pairs in Guo2019–CIP and Schiebinger2019–2i), alongside MPRO at right (dotted line at 0.10).

e, External long-read terminal-exon models (Long, Trip12.G1389.16; Short, Trip12.G1389.149; GSE282319) and five predicted-site tiers on chr1 minus-strand coordinates relative to the terminal-exon start: pluripotent stem cell (PSC)-expressed miRNA seeds (PSC miRNA, 16/16 annotations/positions; Figure S17a), direct mouse RBP matrices (Direct RBP, 2/2), human-transferred matrices for RBPs with $\geq$ 2 CPM in P of both mouse studies (Transf. RBP+, 29/28; Figure S17c), and in gray, other miRNA seeds (Other miRNA, 52/51) and non-expressed transferred RBPs (Transf. RBP−, 4/4). See Supplementary Methods Section S1.8, Supplementary Results Section S2.5 and Supplementary Table S6c for full numerical summaries.

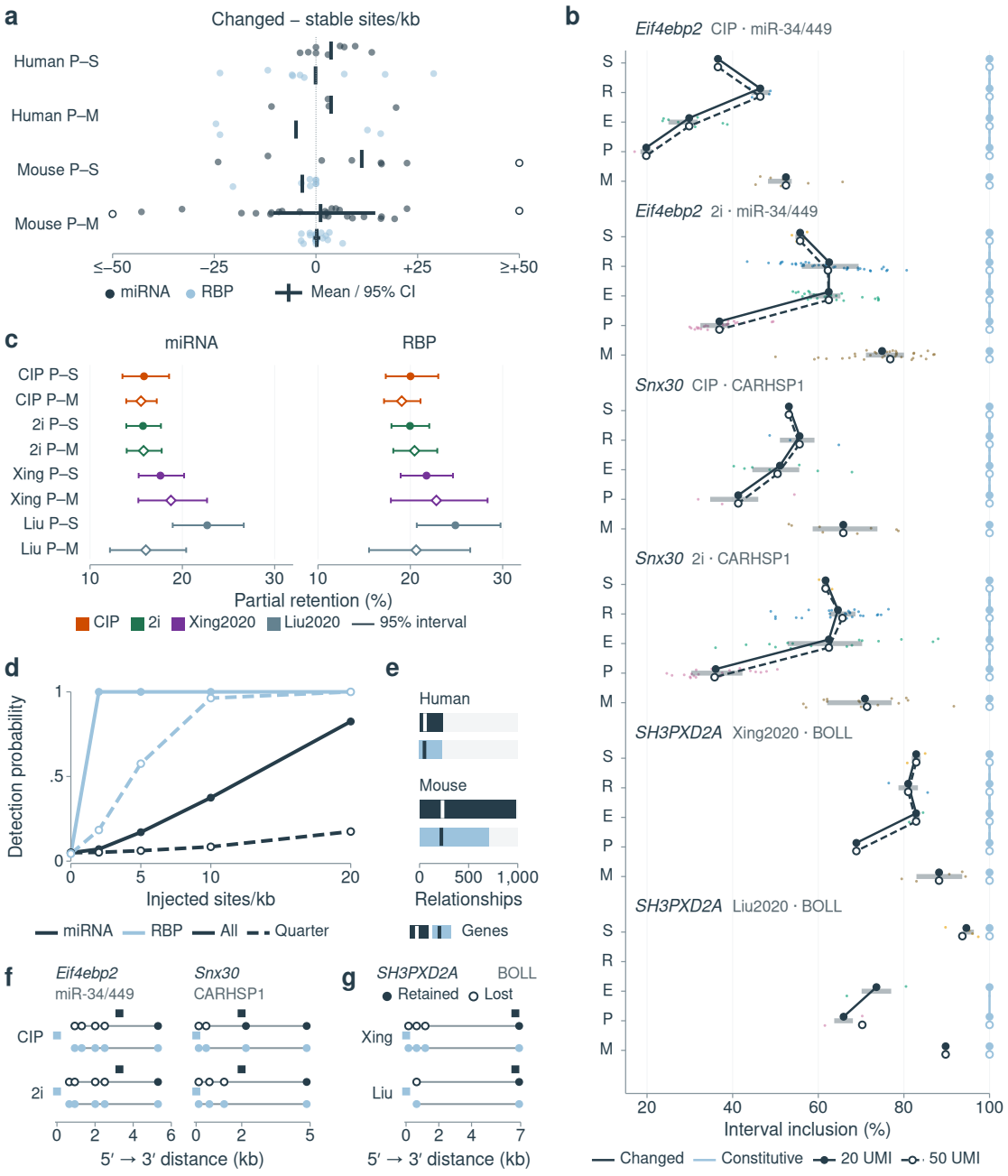

Figure S16. Predicted-site density of changed 3′ UTR windows, and partial retention of exact predicted sites.

State codes follow Figures S1–S3 (Section S1.8).

a, Per-gene predicted-site density difference between changed and matched stable 3′ UTR windows (sites/kb; points, genes, open at axis ends beyond ±50; vertical ticks, equal-gene means; horizontal bars, gene-bootstrap 95% confidence intervals where $n \geq 10$) for miRNA (upper) and RBP (lower) sites across human P–S ($n = 9$), human P–M ($n = 4$), mouse P–S ($n = 8$) and mouse P–M ($n = 25$ genes; both mouse P–M tests $q_8 = 1$).

b, State-specific interval inclusion for the three predefined P–M partial-retention examples, predicted miR-34/449 (GGCAGTG) seed sites in mouse *Eif4ebp2* (chr10, minus strand), CARHSP1 sites in mouse *Snx30* (chr4, plus strand) and BOLL sites in human *SH3PXD2A* (chr10, minus strand), at 20 UMIs (small state-colored points, libraries; horizontal bars, empirical interquartile ranges; filled markers and solid lines, equal-library means across S–R–E–P; M plotted separately) and 50 UMIs (open markers and dashed lines, vertically offset).

c, Partial retention (% of changed multisite gene–factor relationships also retaining a constitutive site of the same factor) with gene-block bootstrap 95% intervals for P–S (filled circles) and P–M (open diamonds) across studies and site categories ($n = 85$–421 denominator genes; CIP, Guo2019–CIP; 2i, Schiebinger2019–2i; Xing, Xing2020; Liu, Liu2020).

d, Simulated detection power ($\alpha = 0.05$, 1,000 simulations per point) of the mouse P–M matched-gene test against injected site density in all (All, solid lines and filled circles) or one quarter (Quarter, dashed lines and open circles) of genes.

e, Exact cross-study partial-retention recurrence by species and site category, pooling P–S and P–M (bars, relationships: 235, 231, 976 and 704; interior vertical ticks, genes: 55, 50, 234 and 222).

f, g, Native PASs (5′-to-3′ genomic distance) and complete-site retention (filled circles, retained; open circles, lost; squares, predicted-site positions; shared key in g) on the changed (upper track) and constitutive (lower track) sites for the three examples in b (**f**, mouse *Eif4ebp2* and *Snx30*; **g**, human *SH3PXD2A*). See Supplementary Methods Section S1.8, Supplementary Results Section S2.5 and Supplementary Tables S5d and S5f for full numerical summaries.

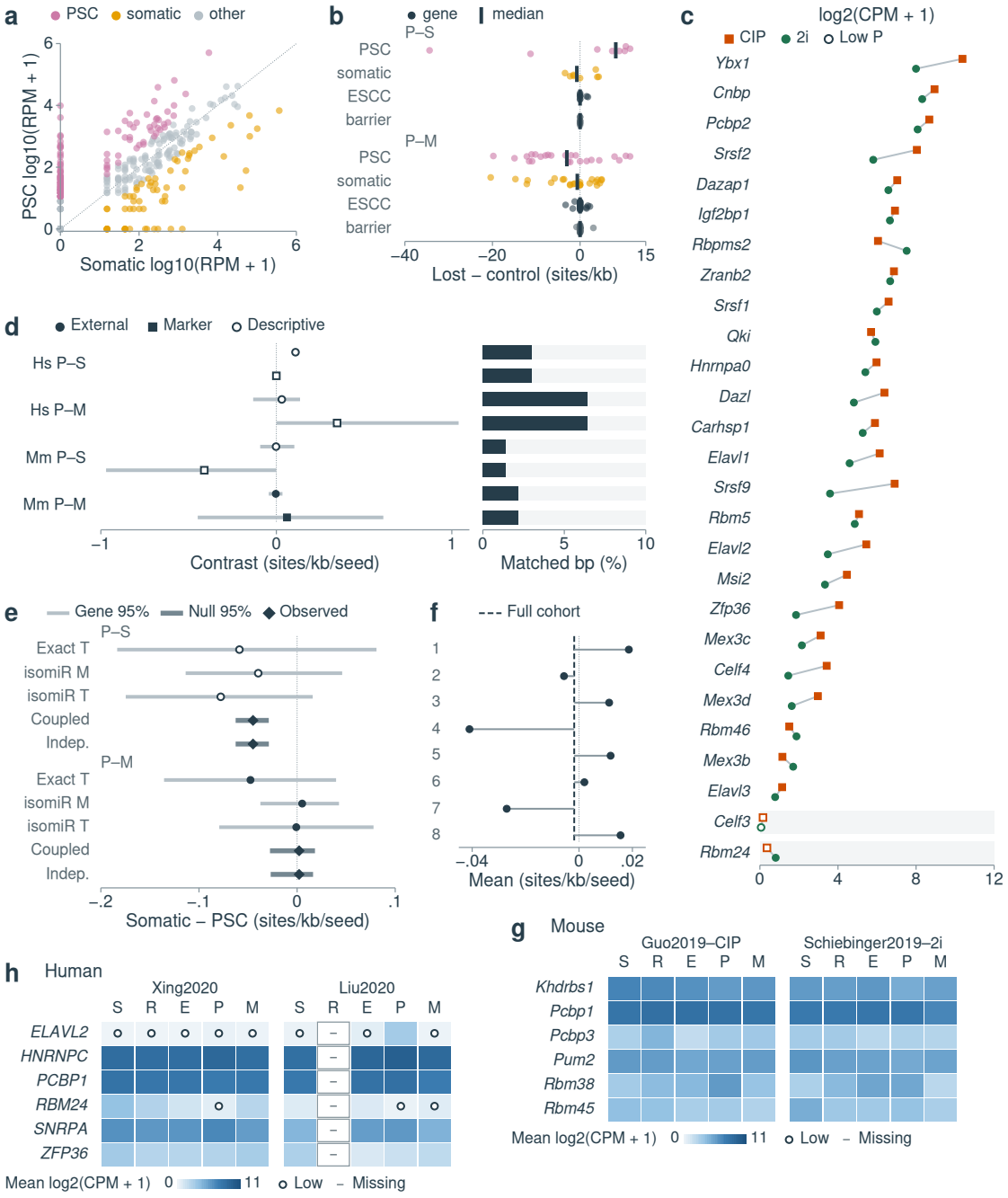

Figure S17. Expression context of the predicted miRNA and RBP sites.

State codes follow Figures S1–S3 (Hs, human; Mm, mouse; Section S1.8).

a, External small-RNA expression ($\log_{10}(\mathrm{RPM}+1)$, reads per million; GSE11724: GSM307156 and GSM307157) of all $n = 394$ mouse seeds in pluripotent stem cell (PSC) and somatic samples, classifying seeds as PSC-expressed (≥ 10 RPM and ≥ 4-fold over somatic, $n = 105$), somatic ($n = 63$) or other ($n = 226$; dotted line of equality).

b, Unnormalized per-gene seed-site density difference (lost minus matched control windows, sites/kb; points, genes; vertical ticks, medians) in mouse P–S ($n = 8$ genes) and P–M ($n = 24$ genes) for PSC, somatic, barrier (miR-34/449 seed GGCAGTG) and embryonic stem cell-specific cell cycle-regulating (ESCC, miR-290/302 seed AAGTGCT) seed groups.

c, P-state expression of RBPs named by transferred motifs in the two *Trip12* strict intervals (Figure S15e) in Guo2019–CIP (CIP, squares) and Schiebinger2019–2i (2i, circles; open symbols, Low P, < 2 CPM in every P library; 25 RBPs retained at ≥ 2 CPM in both studies, shaded CELF3 and RBM24 removed).

d, Seed-count-normalized lost-minus-control density contrasts (sites/kb per seed; lines, gene-bootstrap 95% intervals) for somatic minus PSC (External, circles) and barrier minus ESCC (Marker, squares) across human P–S ($n = 2$), human P–M ($n = 4$), mouse P–S ($n = 8$, open descriptive symbols) and mouse P–M ($n = 24$ genes, filled symbols, both $q_8 = 1$), alongside the percentage of lost 3′ UTR bases covered by matched control windows (right bars, 1.41%–6.45%).

e, Mouse somatic-minus-PSC contrasts under alternative small-RNA mappings (Exact T, exact total RPM; isomiR M and T, mapped and total isomiR RPM; circles and light lines, bootstrap 95% intervals) and coupled or independent (Indep.) position-randomization nulls (diamonds and dark 95% null ranges; all 30 planned positions $q_{30} = 1$).

f, Leave-one-gene-out means for the mouse P–S somatic-minus-PSC contrast ($n = 8$ genes; dashed line, full-cohort mean; dotted line, zero).

g, h, State-resolved expression (mean $\log_2(\mathrm{CPM} + 1)$) of the six predefined display RBPs in mouse (**g**) and human (**h**) studies (open circles, Low, < 2 CPM in all libraries of that state; dashes, Missing state). See Supplementary Methods Section S1.8, Supplementary Results Section S2.5 and Supplementary Tables S5d and S5e for full numerical summaries.

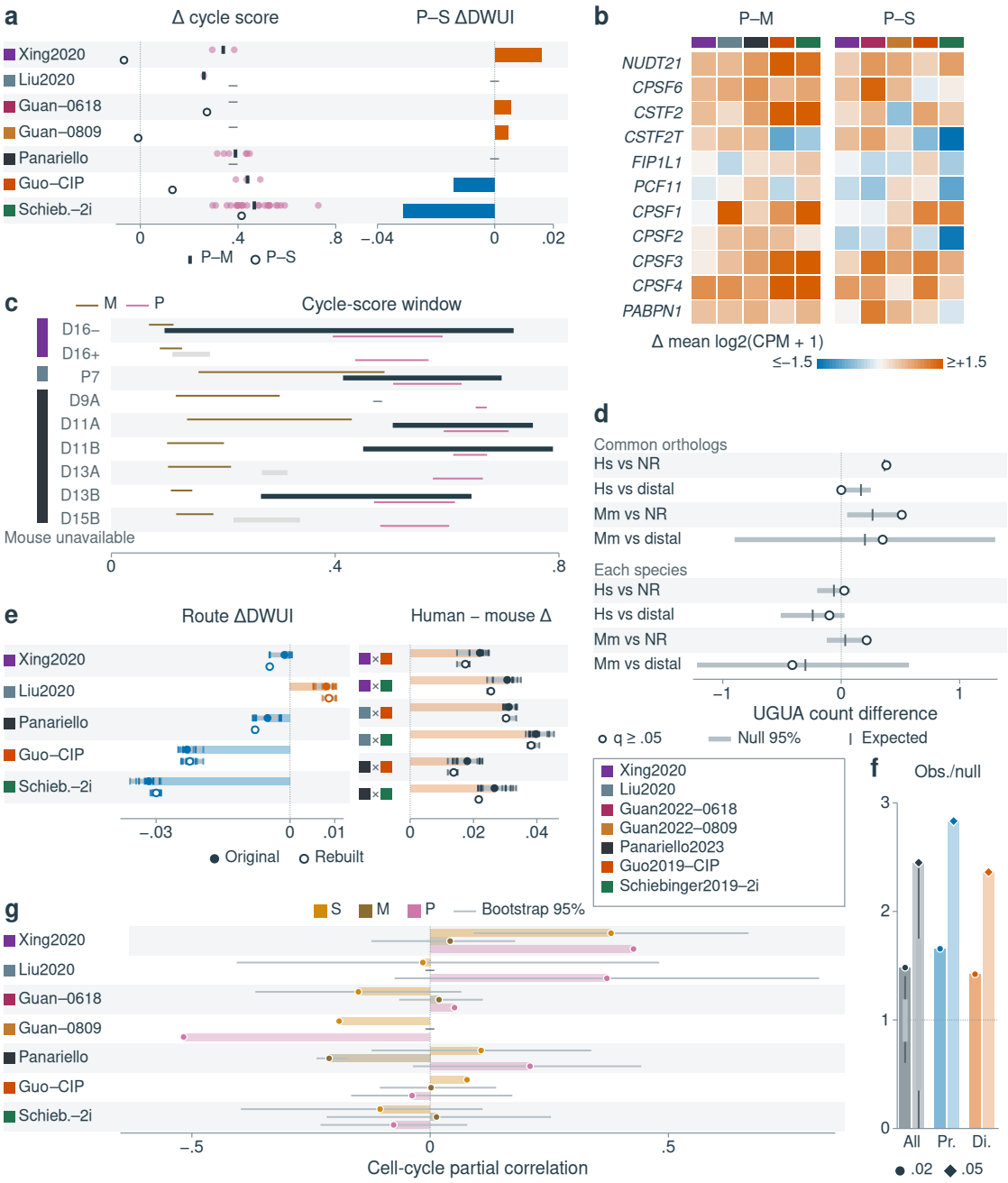

Figure S18. Cell-cycle and CPA-factor expression context of P, the upstream UGUA test, and common-window and lower-cycle-half P–M sensitivity analyses.

State codes follow Figures S1–S3. ΔDWUI is target minus reference (negative, proximal). Cell-cycle scores average the 10-gene S-phase and 8-gene G2/M-phase $\ln(1 + \text{CP10K})$ module means across eligible libraries (Sections S1.6 and S1.7).

a, Left, cell-cycle score differences for paired P–M (upper track: pink points, libraries; bold ticks, route means) and unpaired documented-source P–S (lower track: open circles, route means; dash, unavailable P–M contrast in Guan2022 or unavailable documented-source P–S contrast in Liu2020 and Panariello2023). Right, documented-source P–S route mean ΔDWUI ($n = 2,780$–$5,826$ genes).

b, Expression differences (Δmean $\log_2(\text{CPM} + 1)$) of 11 core cleavage and polyadenylation (CPA) factors for paired P–M and documented-source P–S (gray, unavailable; blue, lower in P; colors saturate at ± 1.5 on the colorbar).

c, Library-specific common cycle-score windows $[\max(\min P, \min M),\ \min(\max P, \max M)]$ across 36 paired P–M libraries (5/9 human and 0/27 mouse eligible at ≥ 3 metacells and ≥ 30 cells per state: dark bars, eligible windows in Xing2020 D16 negative, Liu2020, and Panariello2023 D11A, D11B and D13B; light gray bars, < 3 metacells; dash, no overlap in Panariello2023 D9A; brown and pink lines, M and P interquartile ranges).

d, Distal-minus-proximal upstream UGUA (TGTA) counts (-100 to -40 bp) comparing proximal responders against non-recurrent (NR) or distal responders in human (Hs) and mouse (Mm) on $n = 52$ common orthologs and each species' strict tandem-3′ UTR background (open circles, observed, all $q_8 \geq 0.05$; vertical ticks, expected; horizontal bars, 95% stratified-null ranges; Section S1.8).

e, Lower-cycle-half P ($\lfloor n/2 \rfloor$ lowest-cycle P metacells per library, purity ≥ 0.8) versus M across five paired P–M series and 16 scenarios: route mean ΔDWUI (left; ticks, scenarios; gray bars, min–max) on intersected original (filled circles, 76/80 estimable) and recomputed (open circles, 43/80 estimable) backgrounds, and human-minus-mouse pair differences (right; 88/88 and 38/38 positive).

f, Observed/expected ratios (bars) for within-species human P–M recurrence within the five eligible cycle windows of **c** ($n = 955$ genes; Table 1 of the main text) across total (All, $q_2 \leq 0.0005$), proximal (Pr.) and distal (Di.) genes at $|\Delta\text{DWUI}| \geq 0.02$ (circles) and ≥ 0.05 (diamonds), with thick gray segments and whiskers marking 95% and min–max null ranges.

g, Within-state partial correlation between metacell cycle score and mean DWUI across S, M and P (points and short bars, route means; horizontal bars, library-bootstrap 95% ranges; dash, unestimable). See Supplementary Methods Sections S1.6–S1.8, Supplementary Results Sections S2.6 and S2.7, and Supplementary Tables S7a–S7c and S10e for full numerical summaries.

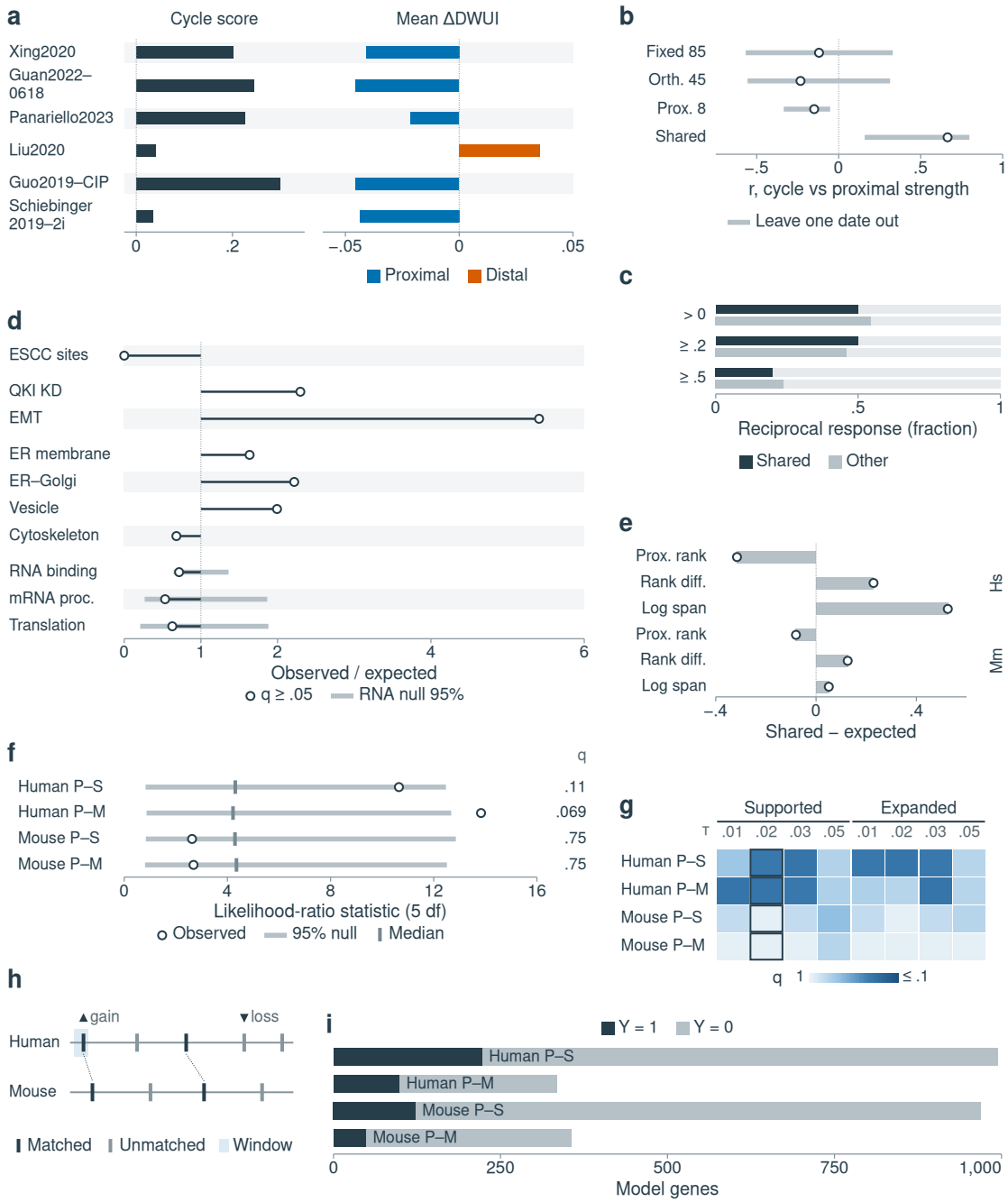

Figure S19. Explanations tested for the shared P–M proximal set, and cis-feature prediction of cross-species sharing.

State codes follow Figures S1–S3. ΔDWUI is target minus reference (negative, proximal; Sections S1.6 and S1.9). Panels a–e examine the $n = 27$ shared P–M proximal orthologs ($|\Delta\text{DWUI}| \geq 0.02$, 751-pair background), and panels f–i test cis-feature prediction of cross-species sharing.

a, Cell-cycle score difference and mean ΔDWUI in S–M (S minus M) across measurable shared proximal orthologs ($n = 16$–27 genes) in Xing2020, Guan2022–0618, Panariello2023, Liu2020, Guo2019–CIP and Schiebinger2019–2i.

b, Within-date across-well correlations in Schiebinger2019–2i between cycle-score increments and P–M proximal shift ($-\Delta\text{DWUI}$) for three fixed panels (Fixed 85, Orth. 45 and Prox. 8 across 11 dates and 22 libraries; points, correlations; bars, leave-one-date-out ranges) and for the shared proximal set across seven paired dates (14 libraries, $2^7 = 128$ sign flips; exact $q_2 = 0.72$ for the cycle predictor; CPA-factor predictor in Table S7e).

c, External U1 perturbation (GSE140543) [52]: fraction of genes shifting proximally under U1 inhibition and distally under U1 overexpression at $|\log_2 \text{ ratio}| > 0$, ≥ 0.2 and ≥ 0.5 in $n = 10$ shared proximal (labeled Shared) and 176 other measurable genes (pale bars, non-reciprocal).

d, Observed/expected hits (open circles, all BH $q \geq 0.05$, with stems to 1) for distal ESCC miRNA seeds (AAGUGCU, $n = 67$ pairs), external QKI-knockdown proximal and epithelial–mesenchymal transition (EMT) distal targets ($n = 605$ genes) [51], four endoplasmic reticulum (ER), Golgi, vesicle, and cytoskeleton GO terms ($n = 751$ pairs), and three RNA-regulation GO terms on the $n = 48$ same-direction shared orthologs (gray bars on the three RNA-regulation rows, 95% null ranges).

e, Observed-minus-expected differences in PAS anchor features (labeled Shared $-$ expected, showing proximal rank, rank difference, and log span as bars with open endpoints) for the shared proximal genes in human (Hs) and mouse (Mm) under the architecture-matched null (all six BH $q_{12} \geq 0.05$).

f, g, Likelihood-ratio statistic adding all five cis features (All cis) to the baseline Firth-logistic model (M1, 5 df) against 4,999 parametric-bootstrap draws in the four primary settings (**f**; supported layer, $\tau = 0.02$; open circles, observed; ticks, null medians; gray bars, 95% null ranges; all BH $q_4 \geq 0.069$) and across all 32 settings (**g**; primary tests outlined; color maps $-\log_{10} q_{32}$, saturating at $q \leq 0.1$).

h, i, Schematic of the five cis features in the PAS (matched switching PASs, 0–2 within 25 nt, and matched discovery PAS fraction), Architecture ($A_g = 2 \times \text{matched}/(\text{human} + \text{mouse PASs})$) and Sequence ($-100$ to $+50$ nt phastCons and -35 to -9 nt hexamer rank, 0–3) groups (**h**), and primary cohort counts ($Y = 1$, predicted-species median effect $\geq \tau$ in the discovery direction, for 223/995, 99/335, 123/969 and 49/356 genes versus $Y = 0$ across human P–S, human P–M, mouse P–S and mouse P–M; **i**). See Supplementary Methods Sections S1.6 and S1.9, Supplementary Results Section S2.6, and Supplementary Tables S4e and S7d–S7f for full numerical summaries.

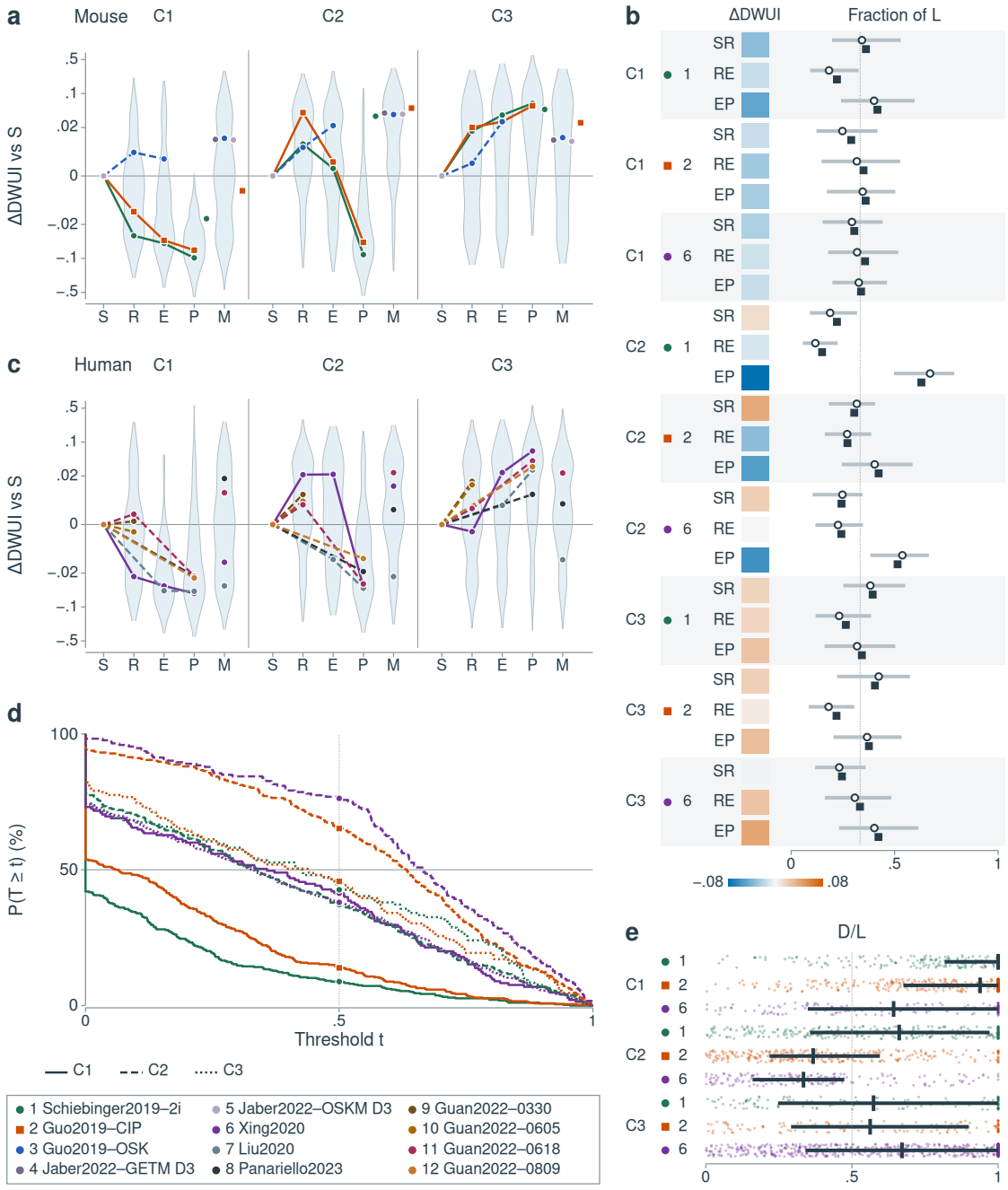

Figure S20. State-resolved APA profile classes and partial endpoint retention.

State codes follow Figures S1–S3. ΔDWUI is target minus S (negative, proximal; Sections S1.4 and S1.5). Classes were fitted jointly on $n = 902$ human (Xing2020: 145, 173, and 584 genes) and $n = 796$ mouse (Guo2019–CIP and Schiebinger2019–2i: 374, 293, and 129 genes) complete S–R–E–P candidates: progressive proximal (C1), distal-then-proximal reversal (C2), and distal (C3). For each profile, path length is $L = |R - S| + |E - R| + |P - E|$, endpoint displacement is $D = |P - S|$ and the turn score is $T = 1 - D/L$.

a, c, Class mean ΔDWUI trajectories per route in mouse (**a**) and human (**c**; solid lines, fitting routes Xing2020, Guo2019–CIP and Schiebinger2019–2i; dashed lines, projected routes without complete S–R–E–P profiles; M shown separately and horizontally offset in **a** in the order Schiebinger2019–2i, Jaber2022–GETM, Guo2019–OSK, Jaber2022–OSKM and Guo2019–CIP) overlaid on kernel-density distributions of all available gene–route values on a shared symmetric logarithmic scale (linear within ±0.02; the numbered study key below d also identifies routes 1–3 in b and e).

b, Adjacent-step structure (SR = S → R, RE = R → E and EP = E → P) by class and fitting route: tile color encodes mean signed step ΔDWUI (blue, negative; white, zero; orange, positive; saturating at ±0.08), open circles and gray bars show medians and interquartile ranges of each step's within-gene share of L, and filled squares show mean shares (dotted vertical line at 1/3).

d, e, Percentage of gene–route profiles with turn score $T \geq t$ (**d**; solid, C1; dashed, C2; dotted, C3; symbols at $t = 0.5$ and horizontal reference at 50%) and per-gene endpoint retention $D/L = 1 - T$ (**e**; jittered points, genes; dark ticks and bars, medians and interquartile ranges; dotted vertical line at 0.5). See Supplementary Methods Sections S1.4 and S1.5, Supplementary Results Section S2.8, and Supplementary Tables S8a, S8b and S8d for full numerical summaries and zoomable gene-level heat maps.

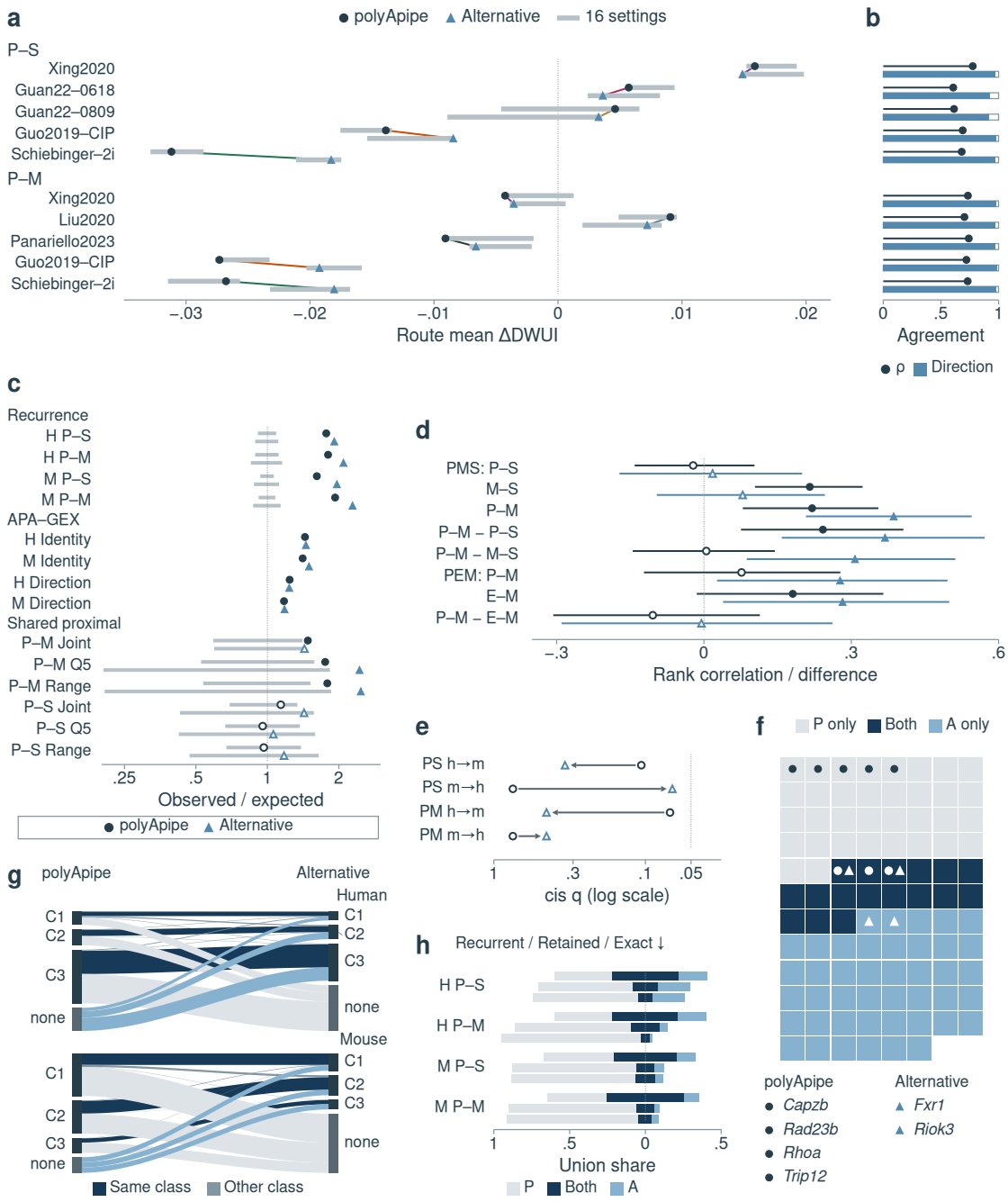

Figure S21. Main analyses repeated with alternative PAS calling.

State codes follow Figures S1–S3 (H and M in c and h, human and mouse; P and A in overlap keys, polyApipe and alternative calling). ΔDWUI is target minus reference (negative, proximal), and MPRO is the unsigned PAS-proportion change range. Circles denote polyApipe and triangles denote alternative PAS calling (Section S1.10). In c–e, filled and hollow markers denote BH $q < 0.05$ and $q \geq 0.05$ (shared key below c).

a, b, Primary route mean ΔDWUI (points) with 16-scenario min–max ranges (gray bars; **a**) and gene-level agreement (**b**; dark points and stems, Spearman ρ; blue bars and unfilled remainders, same- and opposite-direction fractions at $|\Delta\text{DWUI}| \geq 0.02$) joining polyApipe (upper line) to alternative calling (lower line) across the ten P–S and P–M series (Guan22, Guan2022; Schiebinger–2i, Schiebinger2019–2i; Xing2020, Liu2020, Panariello2023 and Guo2019–CIP).

c, Count-based tests on a log observed/expected scale (dotted line at 1) with 95% null ranges (gray bars, where available) for within-species recurrence ($|\Delta\text{DWUI}| \geq 0.02$, 24-test family), APA–GEX

identity and direction (8-test family), and shared P–S/P–M proximal orthologs under the joint, reference-DWUI quintile (labeled Q5) and reference-DWUI range nulls (2-test families).

d, Homologous-PAS (25 bp) rank correlations and paired differences with bootstrap 95% intervals and capacity-conditioned q_8 calls for Xing2020 P/M/S pair means (PMS, first five rows) and the Liu2020–Guo2019–CIP P/E/M control (PEM, last three rows; dotted line at 0).

e, Cis-feature likelihood-ratio test q_4 values (log scale, dotted line at $q = 0.05$) with arrows from polyApipe to alternative calling for h $\rightarrow$ m and m $\rightarrow$ h P–S (PS) and P–M (PM) prediction.

f, Low-net-shift mouse P–M screen ($n = 94$ union genes with $|\Delta\text{DWUI}| < 0.02$ and MPRO ≥ 0.10: 34 polyApipe only, 17 both, and 43 alternative only; circles and triangles mark strict intervals; $|\Delta\text{DWUI}| < 0.01$ strict genes are *Capzb*, *Rad23b*, *Rhoa* and *Trip12* for polyApipe, and *Fxr1* and *Riok3* for alternative calling).

g, Alluvial comparison of S–R–E–P profile classes (C1–C3, Figure S20) between polyApipe ($n = 902$ human and 796 mouse candidates; 403 and 277 jointly selected) and alternative calling (dark blue, same class; mid-gray, switched; light gray/blue, single-workflow).

h, Union partitioning (polyApipe only, shared Jaccard segment, and alternative only) by species and contrast for recurrent genes (Recurrent), site-retention genes (Retained), and exact sites in strict intervals (Exact). See Supplementary Methods Section S1.10, Supplementary Results Section S2.10 and Supplementary Tables S4b and S9a for full numerical summaries.

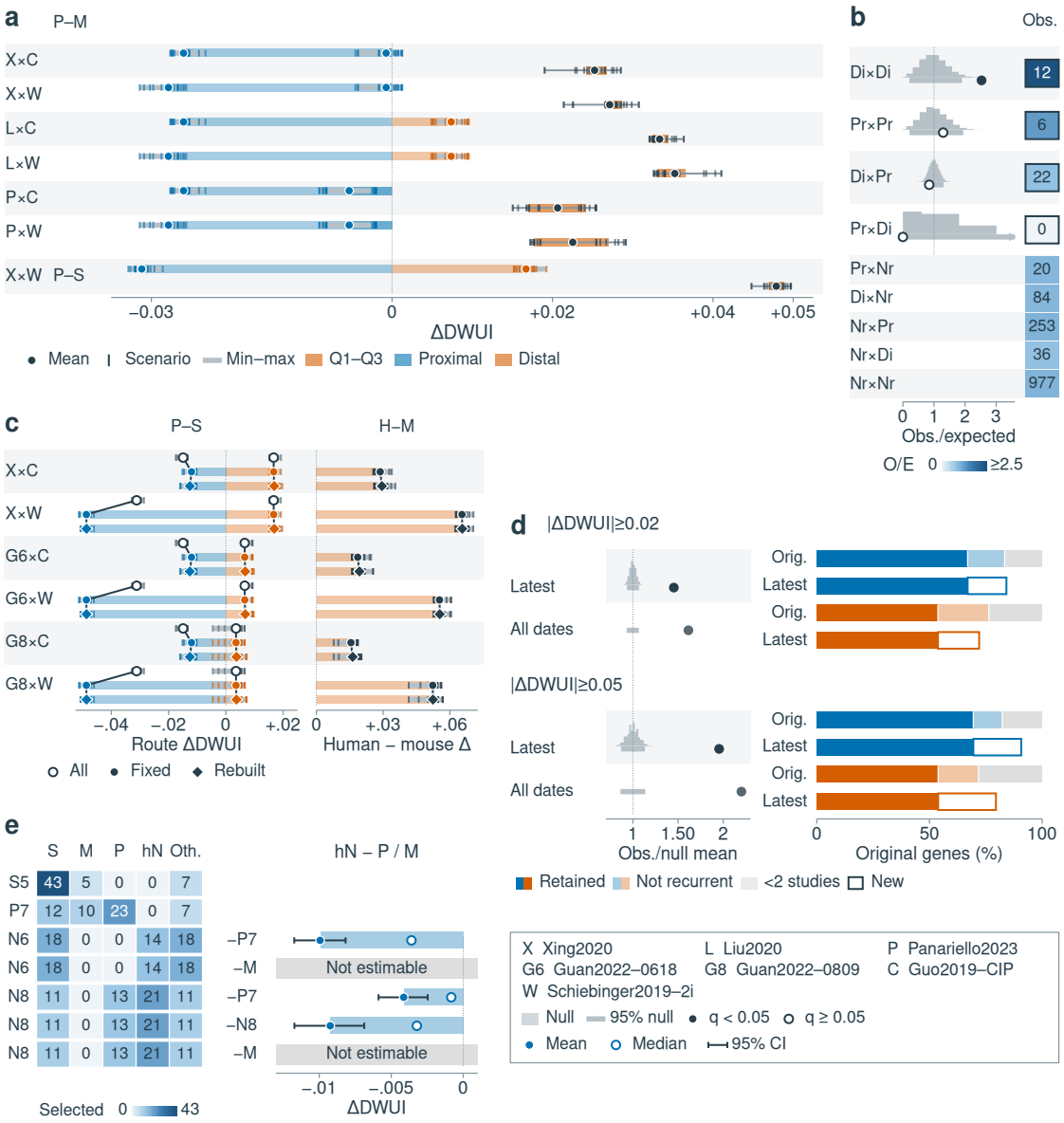

Figure S22. Route, sampling-date and state-reference sensitivity analyses.

State codes follow Figures S1–S3 (Other, Oth., pools E, K and hU). ΔDWUI is target minus reference (negative, proximal; Section S1.12). Paired labels in **a**–**c** list human first and mouse second (shared key at bottom).

a, Fibroblast-derived subset of primary ΔDWUI estimates across all 16 setting-by-background scenarios without recomputing backgrounds, spanning five paired P–M series (Xing2020, Liu2020 and Panariello2023 in human; Guo2019–CIP and Schiebinger2019–2i in mouse) and the transcription-factor-induced P–S pair (Xing2020 and Schiebinger2019–2i). Upper track per row, mouse (left) and human (right) route means (bars and filled circles, 16-scenario means; ticks, scenarios; gray bars, min–max). Lower track, matched human-minus-mouse differences (Human − mouse Δ; filled circles, means; orange boxes, interquartile ranges; whiskers, min–max; ticks, scenarios; all 96/96 P–M and 16/16 P–S positive).

b, Cross-species P–S direction pairing ($|\Delta\text{DWUI}| \geq 0.02$, $n = 1,410$ orthologs) after mouse latest-date restriction as in **c**, showing 3×3 human-by-mouse counts (Pr, proximal; Di, distal; Nr, non-recurrent; shaded by observed/expected ratio, tested cells outlined) alongside observed/expected ratios (circles, filled for BH $q_4 < 0.05$), 10,000-permutation histograms and 95% full-assay null ranges.

c, Documented-source P–S route mean ΔDWUI (left) and human-minus-mouse differences (right) across all dates (All, open circles) and after restricting mouse P to its latest date (D40 in Guo2019–CIP and D18 in Schiebinger2019–2i, with Xing2020, Guan2022–0618 and –0809 unchanged) on intersected original (Fixed, filled circles) and recomputed (Rebuilt, filled diamonds; bars, means; gray bars, min–max; ticks, scenarios; 96/96 positive) backgrounds.

d, Mouse P–S recurrence after latest-date restriction ($n = 2,077$ versus $2,521$ all-date genes) at $|\Delta\text{DWUI}| \geq 0.02$ and ≥ 0.05: observed/null-mean ratios (filled circles, $q_2 = 1.0 \times 10^{-4}$), 10,000-permutation histograms and 95% L3 null ranges (left), and direction-split stacked bars normalized to original counts (right; Orig. paired with Latest for proximal in blue and distal in orange). At 0.02 and 0.05, proximal counts were $n = 511$ and 226 originally versus 430 and 205 at the latest date, and distal counts were $n = 93$ and 39 versus 67 and 31. Segments partition genes into Retained, two-study non-recurrence (labeled Not recurrent), < 2 studies (gray), and newly recurrent at the latest date (labeled New; opposite recurrence $= 0$).

e, State composition of Liu2020 libraries S5 (GSM4546545), N6 (GSM4546546), P7 (GSM4546547), and N8 (GSM4546548; left, purity-≥ 0.8 selected metacells across 213/252 selected/unfiltered, with 10/12 selected/unfiltered M in P7 and 0 M in N6 and N8) and ΔDWUI (right; bars and filled circles with 95% bootstrap intervals, means; open circles, medians) for the three estimable hN–P contrasts (N6–P7, $n = 2,620$; N8–P7, $n = 2,675$; N8–N8 same-library hN–P, $n = 459$, where –P7 and –N8 denote P of those libraries) and unestimable hN–M rows (0/32 scenarios; S5 and P7 are inventory-only rows). See Supplementary Methods Section S1.12, Supplementary Results Sections S2.1 and S2.9, and Supplementary Tables S2b, S2e and S10d for full numerical summaries.

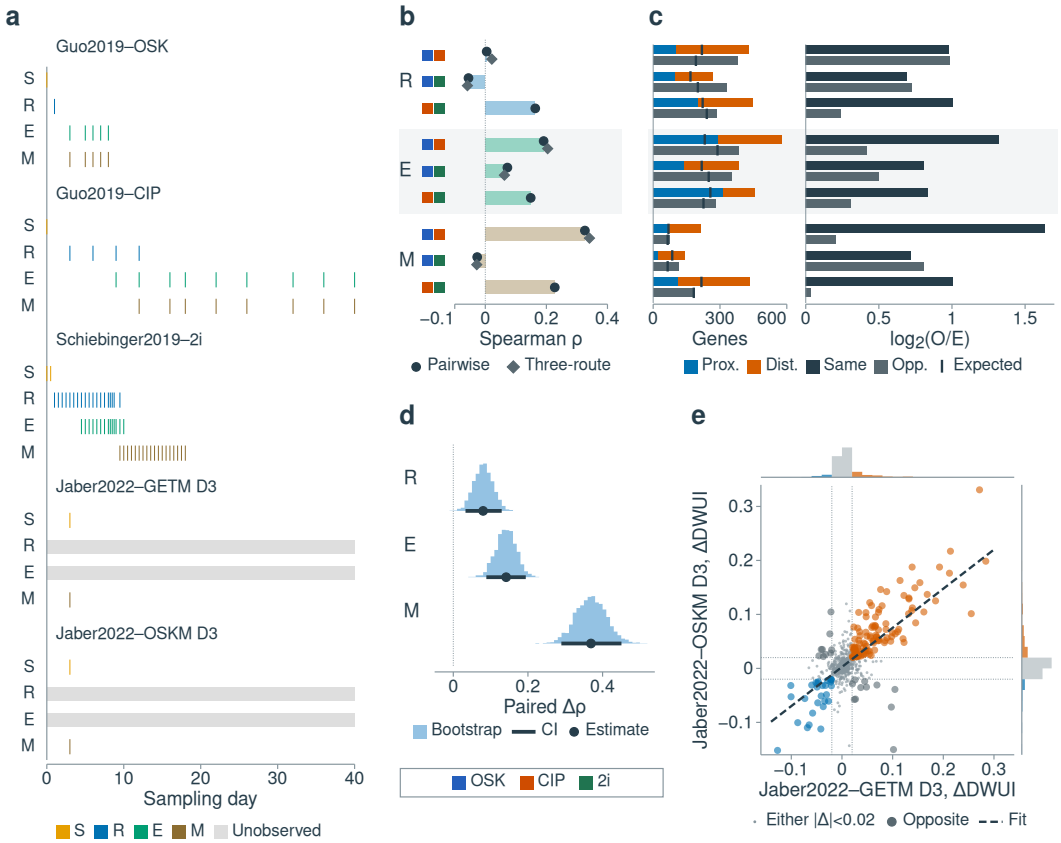

Figure S23. Gene-level APA response correspondence across R, E and M states and between day-3 captures.

State codes follow Figures S1–S3. ΔDWUI is target minus observed S (negative, proximal; Section S1.12).

a, Qualified sampling dates (colored ticks) of all five mouse routes on a common day axis across S, R, E and M (qualified library counts: 1, 1, 5, 5 in Guo2019–OSK; 1, 4, 9, 8 in Guo2019–CIP; 4, 36, 26, 36 in Schiebinger2019–2i; and 1 S and 1 M at day 3 in Jaber2022–GETM and –OSKM, with unobserved R and E in light gray).

b, Pairwise Spearman ρ of gene-level ΔDWUI relative to observed S across Guo2019–OSK (OSK), Guo2019–CIP (CIP) and Schiebinger2019–2i (2i; shared key below d) in R, E and M on each route pair's jointly measurable gene set (Pairwise, filled circles; $n = 3,713$–$4,576$ in R, $3,465$–$4,435$ in E and $1,289$–$2,731$ in M) and the three-route common intersection (Three-route, filled diamonds; $n = 3,576$, $3,327$ and $1,288$).

c, Observed same-direction (upper stacked bars: blue, both proximal, Prox.; orange, both distal, Dist.) and opposite-direction (lower gray bars, Opp.) gene counts at $|\Delta\text{DWUI}| \geq 0.02$ versus marginal expectations (E_{same} and E_{opp}, vertical ticks, Expected) in the row order of **b**, paired on the right with $\log_2(O/E)$ bars for same-direction (upper dark bars, Same) and opposite-direction (lower gray bars, Opp.) responses, where zero denotes $O = E$.

d, Difference in Spearman rank correlation $\Delta\rho = \rho(\text{Guo2019–OSK}, \text{Guo2019–CIP}) - \rho(\text{Guo2019–OSK}, \text{Schiebinger2019–2i})$ on the three-route common gene set in R, E and M, showing 2,000-resample conditional gene-bootstrap step histograms (0.01-unit bins, peak-scaled), point estimates (filled circles) and 95% confidence intervals (thick bars, CI).

e, Same-day M–S ΔDWUI comparison between day-3 Jaber2022 GETM (GSM6071749, horizontal axis) and OSKM (GSM6071750, vertical axis) captures across $n = 882$ jointly measurable mouse genes ($\rho = 0.465$; blue and orange points, shared proximal and distal responders at $|\Delta\text{DWUI}| \geq 0.02$; dark gray, opposite-direction responders, Opposite; light gray, $|\Delta\text{DWUI}| < 0.02$ in either capture, Either $|\Delta| < 0.02$; dotted lines, ± 0.02 thresholds; dashed line, linear fit, Fit; top and right peak-scaled marginal step histograms in 0.02-unit bins). See Supplementary Methods Section S1.12, Supplementary Results Section S2.9 and Supplementary Table S10f for full numerical summaries.

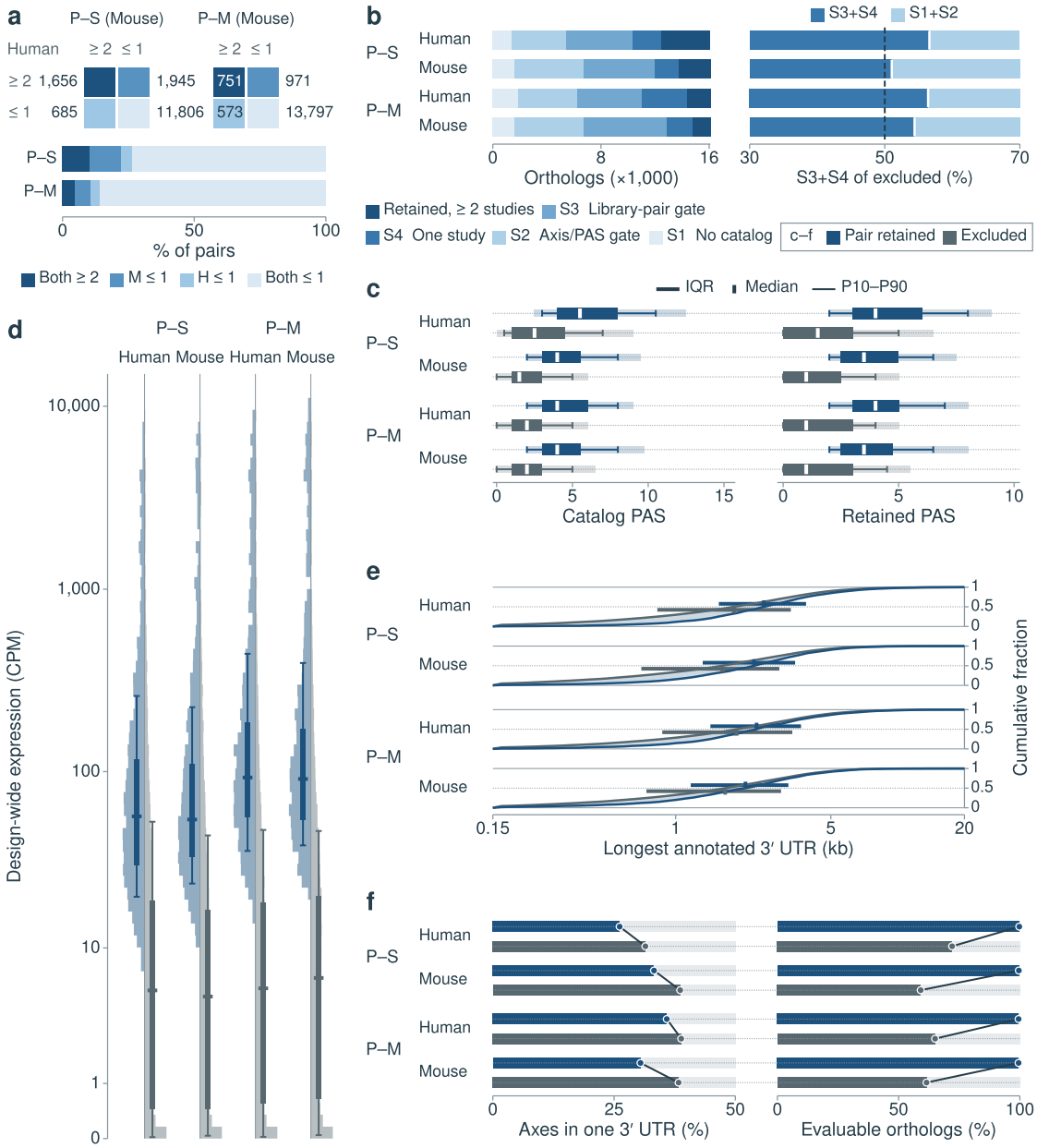

Figure S24. Stage-by-stage attrition and feature distributions of retained versus excluded one-to-one orthologs.

State codes follow Figures S1–S3 (in panel a, H and M denote human and mouse; Section S1.11).

a, Ortholog-pair retention (2 × 2 matrices above and four-category 0–100% stacked bars below) across all $n = 16,092$ Ensembl release 116 one-to-one human–mouse orthologs on the primary setting for documented-source P–S (1,656 retained, 10.3%, and 14,436 excluded) and paired P–M (751 retained, 4.7%, and 15,341 excluded).

b, Within-species furthest-step attrition across P–S human, P–S mouse, P–M human and P–M mouse: stacked counts (left, in thousands) across S1 No catalog, S2 Axis/PAS gate, S3 Library-pair gate, S4 One study, and retained in ≥ 2 studies ($n = 3,601$, 2,341, 1,722 and 1,324), paired with the percentage split of excluded genes between measurement and replication gates (S3+S4) and structural catalog and PAS gates (S1+S2; right, 30–70% axis, dashed 50% line; shared blue and gray key below b for c–f).

c, Study-median primary catalog PAS counts (left) and reference-supported retained PAS counts (right) in pair-retained (upper) versus excluded (lower) orthologs across the four groups (horizontal

box-percentile plots: interquartile boxes, white medians, 10th–90th percentile whiskers and 5th–95th percentile shading; S1 genes have 0 PASs).

d, Design-wide endpoint-metacell expression (counts per million, CPM, on a $\log_{10}(\mathrm{CPM}+1)$ scale; purity $\geq$ 0.8) shown as mirrored histograms with square-root frequency scaling normalized to each group's peak for pair-retained (left) and excluded (right) orthologs (bars, interquartile ranges; cross-ticks, medians; whiskers, 10th–90th percentiles [labeled P10–P90]).

e, Empirical cumulative distributions of longest annotated terminal 3′ UTR length (kb, Ensembl 116 GRCh38.116 and GRCm39.116; log axis spanning 0.15–20 kb with boundary pooling, shaded group differences, and bars at cumulative probability 0.5 marking medians and interquartile ranges).

f, Percentage of evaluable full primary PAS axes within one annotated terminal 3′ UTR (left) and percentage of orthologs with an evaluable annotated full axis (right; paired bars and connecting lines, pale tracks to axis limit). See Supplementary Methods Section S1.11, Supplementary Results Section S2.11 and Supplementary Table S10g for full numerical summaries.

S4. Supplementary tables

Supplementary Tables S1–S10 are supplied as one workbook, `Supplementary_Tables_S1-S10.xlsx`, with one worksheet per lettered table (including Tables S1i and S10c), grouped by topic. Each worksheet holds one or more data blocks with complete rows, denominators, negative results and correction families. Worksheet headers name the related figures or, where none applies, the analysis. Worksheets marked † hold analyses specified after the initial results. Some unmarked worksheets also contain blocks with such analyses, for example the nested null models in Table S3b (block S3b.2) and the sequence-background sensitivities in Table S5d (blocks S5d.6 and S5d.7). The Contents sheet indexes the worksheets, and the Sources sheet gives the source file, row filter and SHA-256 hash of every data block. In these files, columns labeled WPP denote DWUI. Every contrast code denotes target minus reference: P_S, PS and P-S denote P−S, and the reference-first codes of the interval tables denote, for example, SP = P−S and MP = P−M. The Contents sheet lists all codes. Plotting exports that are not needed to reuse the results are provided in the source-data archive.

Table S1. Datasets, libraries and expression states.

S1a Expression states, marker evidence, partition stability and sampling (Figures S1–S3).

S1b Datasets.

S1c Sequencing libraries.

S1d Expression-atlas libraries.

S1e Local expression partitions.

S1f Local-state annotations.

S1g Integration orthologs.

S1h Mouse annotation programs (Figure S2).

S1i† Extended route metadata, induction protocols, sampling units, library denominators and source provenance across studies (Table 2 of the main text; Guan2022 compound-code key in block S1i.2).

Table S2. PAS measurement and route-level PAS position.

S2a PAS catalog and reference support (Figure S4).

S2b Route means across 16 settings (Figure S5b,c).

S2c Tandem-3′ UTR restriction (Figure S5d).

S2d Common one-to-one ortholog background (1,306 P–S and 208 P–M genes; Figure S5b).

S2e Observed-state references (Figure S5a,e,f).
S2f† Route-mean composition by sign (Figure 1e).

Table S3. Within-species recurrence and its context.

S3a Contrast design, series and source libraries (Figures S3c; S6a–e).
S3b Recurrent genes and conditional nulls (Figure S6a,e).
S3c Direction composition of recurrent genes (Figure S6b).
S3d Measurement controls, wells and external PAS-seq (Figure S6c,d,f–h).
S3e APA–GEX response identity and direction (Figure S8a–c).
S3f† Nested functional backgrounds (Figure S7a,b,d,e).
S3g† Direction-specific recurrence (Figure 2a).
S3h† Strict tandem-3′ UTR subset (Figure S8d,e).

Table S4. Cross-species comparisons and cis-feature models.

S4a Sharing tests and correction families (Figure S9b–f).
S4b Shared proximal candidates (Figure S9a).
S4c Correspondence on homologous PASs and reference differences (Figure S11a–e).
S4d *PDLIM7*/*Pdlim7* structure (Figure S11f,g).
S4e Cis features and increment tests (Figure S19f–i).
S4f† Direction pairing between species (Figure 3a,b).
S4g† Event classes of paired responses (Figure 3c; Figure S10a–c).
S4h† Corresponding PAS switches and homologous seed matches (Figure S10d,e).
S4i† Naive-state specificity of the shared proximal set (Figure S12).
S4j† Orthologs with same-direction responses in both species (Figure 3a; Figure S19d).

Table S5. Interval inclusion and predicted-site retention.

S5a Union pool and interval models (Figure S13a).
S5b Interval agreement (Figure S13b,c).
S5c† Weighted predicted-site retention (Figure S13d,e).
S5d Site density and external miRNA seed groups (Figures S16a,d; S17a,b,d–f).
S5e† Candidate-RBP expression (Figure S17c,g,h).
S5f Exact-site partial retention (Figure S16b,c,e–g).
S5g RBP motif provenance (CisBP-RNA build 2.00).

Table S6. Low-net-shift genes and interval examples.

S6a† Strict intervals and gene-wide shifts (Figure 6b,d).
S6b The 51 low-net-shift genes (Figure S14).
S6c† *Trip12* (Figure S15).
S6d *Riok3* in both PAS workflows (Figure 6c; Figure S21).

Table S7. Candidate explanations of the shared proximal response.

S7a† Cell-cycle scores and within-state PAS position (Figure S18a,g).
S7b† Core CPA-factor expression (Figure S18b).
S7c† Upstream UGUA signature (Figure S18d).
S7d† S–M contrast on the shared proximal core (Figure S19a).
S7e† Within-date cell-cycle increments in Schiebinger2019–2i (Figure S19b).
S7f† Candidate mechanisms and functional categories (Figure S19c–e).

S7g† Cell-cycle scores and common-support diagnostics.

Table S8. State-resolved APA profile classes.

S8a Resolution and candidate membership (Figure S20a,c).

S8b Ortholog class correspondence (Figure S20a,c).

S8c Rank tests of GO and KEGG terms on APA and expression (Figure S7c).

S8d Stage contributions and path geometry (Figure S20b,d,e).

Table S9. Main analyses repeated with alternative PAS calling.

S9a Alternative PAS calling (Figure S21).

S9b Strict interval pairs under alternative PAS calls (Figure S21).

Table S10. Reference-state and revision sensitivity analyses.

S10a† Marker-defined P and M references.

S10b† Shared proximal set under marker-defined M.

S10c† Candidate-level retention across PAS-calling, reference-state and lower-cycle half of P sensitivity analyses and descriptive prioritization (Table 1 of the main text; Sections S1.11.2 and S1.7.2).

S10d† Fibroblast-derived series subset, latest eligible P sampling-date restriction and Liu2020 state-composition and naive-reference check (Table 1 of the main text; Figure S22).

S10e† Lower-cycle half of P and within-library common cycle-score support window analyses (Table 1 of the main text; Figure 5; Figure S18c,e,f).

S10f† Gene-level APA response correspondence across R, E and M states and between day-3 captures (Table 1 of the main text; Figure S23).

S10g† Stage-by-stage attrition and feature distributions of retained versus excluded one-to-one orthologs (Table 1 of the main text; Figure S24).

Analysis code and generator inputs are available with the source data (main-text Data Availability Statement).

References

1. Xing, Q.R.; El Farran, C.A.; Gautam, P.; Chuah, Y.S.; Warrier, T.; Toh, C.X.D.; Kang, N.Y.; Sugii, S.; Chang, Y.T.; Xu, J.; et al. Diversification of reprogramming trajectories revealed by parallel single-cell transcriptome and chromatin accessibility sequencing. *Sci. Adv.* **2020**, *6*, eaba1190. https://doi.org/10.1126/sciadv.aba1190.
2. Liu, X.; Ouyang, J.F.; Rossello, F.J.; Tan, J.P.; Davidson, K.C.; Valdes, D.S.; Schröder, J.; Sun, Y.B.Y.; Chen, J.; Knaupp, A.S.; et al. Reprogramming roadmap reveals route to human induced trophoblast stem cells. *Nature* **2020**, *586*, 101–107. https://doi.org/10.1038/s41586-020-2734-6.
3. Guan, J.; Wang, G.; Wang, J.; Zhang, Z.; Fu, Y.; Cheng, L.; Meng, G.; Lyu, Y.; Zhu, J.; Li, Y.; et al. Chemical reprogramming of human somatic cells to pluripotent stem cells. *Nature* **2022**, *605*, 325–331. https://doi.org/10.1038/s41586-022-04593-5.
4. Panariello, F.; Gagliano, O.; Luni, C.; Grimaldi, A.; Angiolillo, S.; Qin, W.; Manfredi, A.; Annunziata, P.; Slovin, S.; Vaccaro, L.; et al. Cellular population dynamics shape the route to human pluripotency. *Nat. Commun.* **2023**, *14*, 2829. https://doi.org/10.1038/s41467-023-37270-w.
5. Guo, L.; Lin, L.; Wang, X.; Gao, M.; Cao, S.; Mai, Y.; Wu, F.; Kuang, J.; Liu, H.; Yang, J.; et al. Resolving Cell Fate Decisions during Somatic Cell Reprogramming by Single-Cell RNA-Seq. *Mol. Cell* **2019**, *73*, 815–829.e7. https://doi.org/10.1016/j.molcel.2019.01.042.
6. Schiebinger, G.; Shu, J.; Tabaka, M.; Cleary, B.; Subramanian, V.; Solomon, A.; Gould, J.; Liu, S.; Lin, S.; Berube, P.; et al. Optimal-transport analysis of single-cell gene expression identifies

developmental trajectories in reprogramming. *Cell* **2019**, *176*, 928–943.e22; Erratum in *Cell* **2019**, *176*, 1517. https://doi.org/10.1016/j.cell.2019.01.006.
7. Jaber, M.; Radwan, A.; Loyfer, N.; Abdeen, M.; Sebban, S.; Khatib, A.; Yassen, H.; Kolb, T.; Zapatka, M.; Makedonski, K.; et al. Comparative parallel multi-omics analysis during the induction of pluripotent and trophectoderm states. *Nat. Commun.* **2022**, *13*, 3475. https://doi.org/10.1038/s41467-022-31131-8.
8. Zheng, G.X.Y.; Terry, J.M.; Belgrader, P.; Ryvkin, P.; Bent, Z.W.; Wilson, R.; Ziraldo, S.B.; Wheeler, T.D.; McDermott, G.P.; Zhu, J.; et al. Massively parallel digital transcriptional profiling of single cells. *Nat. Commun.* **2017**, *8*, 14049. https://doi.org/10.1038/ncomms14049.
9. Wolock, S.L.; Lopez, R.; Klein, A.M. Scrublet: Computational Identification of Cell Doublets in Single-Cell Transcriptomic Data. *Cell Syst.* **2019**, *8*, 281–291.e9. https://doi.org/10.1016/j.cels.2018.11.005.
10. Wolf, F.A.; Angerer, P.; Theis, F.J. SCANPY: large-scale single-cell gene expression data analysis. *Genome Biol.* **2018**, *19*, 15. https://doi.org/10.1186/s13059-017-1382-0.
11. Dong, W.; Charikar, M.; Li, K. Efficient k-nearest neighbor graph construction for generic similarity measures. In Proceedings of the 20th International Conference on World Wide Web, Hyderabad, India, 28 March–1 April 2011; pp. 577–586. https://doi.org/10.1145/1963405.1963487.
12. Traag, V.A.; Waltman, L.; van Eck, N.J. From Louvain to Leiden: guaranteeing well-connected communities. *Sci. Rep.* **2019**, *9*, 5233. https://doi.org/10.1038/s41598-019-41695-z.
13. Lopez, R.; Regier, J.; Cole, M.B.; Jordan, M.I.; Yosef, N. Deep generative modeling for single-cell transcriptomics. *Nat. Methods* **2018**, *15*, 1053–1058. https://doi.org/10.1038/s41592-018-0229-2.
14. Gayoso, A.; Lopez, R.; Xing, G.; Boyeau, P.; Valiollah Pour Amiri, V.; Hong, J.; Wu, K.; Jayasuriya, M.; Mehlman, E.; Langevin, M.; et al. A Python library for probabilistic analysis of single-cell omics data. *Nat. Biotechnol.* **2022**, *40*, 163–166. https://doi.org/10.1038/s41587-021-01206-w.
15. Klein, D.; Palla, G.; Lange, M.; Klein, M.; Piran, Z.; Gander, M.; Meng-Papaxanthos, L.; Sterr, M.; Saber, L.; Jing, C.; et al. Mapping cells through time and space with moscot. *Nature* **2025**, *638*, 1065–1075. https://doi.org/10.1038/s41586-024-08453-2.
16. McInnes, L.; Healy, J.; Saul, N.; Großberger, L. UMAP: Uniform Manifold Approximation and Projection. *J. Open Source Softw.* **2018**, *3*, 861. https://doi.org/10.21105/joss.00861.
17. Yates, A.D.; Austine-Orimoloye, O.; Azov, A.G.; Barba, M.; Barnes, I.; Barrera-Enriquez, V.P.; Becker, A.; Bennett, R.; Berry, A.; Bhai, J.; et al. Ensembl 2026. *Nucleic Acids Res.* **2026**, *54*, D1053–D1060. https://doi.org/10.1093/nar/gkaf1239.
18. Kinsella, R.J.; Kähäri, A.; Haider, S.; Zamora, J.; Proctor, G.; Spudich, G.; Almeida-King, J.; Staines, D.; Derwent, P.; Kerhornou, A.; et al. Ensembl BioMarts: a hub for data retrieval across taxonomic space. *Database* **2011**, *2011*, bar030. https://doi.org/10.1093/database/bar030.
19. Johnson, J.; Douze, M.; Jégou, H. Billion-Scale Similarity Search with GPUs. *IEEE Trans. Big Data* **2021**, *7*, 535–547. https://doi.org/10.1109/TBDATA.2019.2921572.
20. Aibar, S.; González-Blas, C.B.; Moerman, T.; Huynh-Thu, V.A.; Imrichova, H.; Hulselmans, G.; Rambow, F.; Marine, J.C.; Geurts, P.; Aerts, J.; et al. SCENIC: single-cell regulatory network inference and clustering. *Nat. Methods* **2017**, *14*, 1083–1086. https://doi.org/10.1038/nmeth.4463.
21. Monash Bioinformatics Platform. polyApipe: a pipeline for counting reads near polyadenylation sites in single-cell RNA-seq data (commit 43d866e15b22). Available online: https://github.com/swbioinf/polyApipe (accessed on 5 October 2026).
22. Liao, Y.; Smyth, G.K.; Shi, W. featureCounts: an efficient general purpose program for assigning sequence reads to genomic features. *Bioinformatics* **2014**, *30*, 923–930. https://doi.org/10.1093/bioinformatics/btt656.
23. Smith, T.; Heger, A.; Sudbery, I. UMI-tools: modeling sequencing errors in Unique Molecular Identifiers to improve quantification accuracy. *Genome Res.* **2017**, *27*, 491–499. https://doi.org/10.1101/gr.209601.116.
24. PolyASite. PolyASite v2.0 bulk 3-prime end-sequencing atlas. Available online: https://polyasite.unibas.ch/atlas (accessed on 3 October 2026).
25. Yu, S.; Chen, W.C.; Wang, L.; Jewell, S.; Mammedova, A.; Han, S.W.; Wickramasinghe, J.; Barash, Y.; Tian, B. PolyA_DB v4: systematic polyA site identification and isoform annotation in human

and mouse genomes using 3′ end and long-read sequencing data. *Nucleic Acids Res.* **2026**, *54*, D247–D254. https://doi.org/10.1093/nar/gkaf1212.
26. GENCODE Project. GENCODE human release 40. Available online: https://www.gencodegenes.org/human/release_40.html (accessed on 3 October 2026).
27. GENCODE Project. GENCODE mouse release M25. Available online: https://www.gencodegenes.org/mouse/release_M25.html (accessed on 3 October 2026).
28. Kent, W.J.; Sugnet, C.W.; Furey, T.S.; Roskin, K.M.; Pringle, T.H.; Zahler, A.M.; Haussler, D. The Human Genome Browser at UCSC. *Genome Res.* **2002**, *12*, 996–1006. https://doi.org/10.1101/gr.229102.
29. Persad, S.; Choo, Z.N.; Dien, C.; Sohail, N.; Masilionis, I.; Chaligné, R.; Nawy, T.; Brown, C.C.; Sharma, R.; Pe'er, I.; et al. SEACells infers transcriptional and epigenomic cellular states from single-cell genomics data. *Nat. Biotechnol.* **2023**, *41*, 1746–1757. https://doi.org/10.1038/s41587-023-01716-9.
30. Benjamini, Y.; Hochberg, Y. Controlling the false discovery rate: a practical and powerful approach to multiple testing. *J. R. Stat. Soc. Ser. B (Methodol.)* **1995**, *57*, 289–300. https://doi.org/10.1111/j.2517-6161.1995.tb02031.x.
31. Ashburner, M.; Ball, C.A.; Blake, J.A.; Botstein, D.; Butler, H.; Cherry, J.M.; Davis, A.P.; Dolinski, K.; Dwight, S.S.; Eppig, J.T.; et al. Gene ontology: tool for the unification of biology. *Nat. Genet.* **2000**, *25*, 25–29. https://doi.org/10.1038/75556.
32. The Gene Ontology Consortium. The Gene Ontology knowledgebase in 2026. *Nucleic Acids Res.* **2026**, *54*, D1779–D1792; Erratum in *Nucleic Acids Res.* **2026**, *54*, gkag678. https://doi.org/10.1093/nar/gkaf1292.
33. Kanehisa, M.; Furumichi, M.; Sato, Y.; Matsuura, Y.; Ishiguro-Watanabe, M. KEGG: biological systems database as a model of the real world. *Nucleic Acids Res.* **2025**, *53*, D672–D677. https://doi.org/10.1093/nar/gkae909.
34. Brumbaugh, J.; Di Stefano, B.; Wang, X.; Borkent, M.; Forouzmand, E.; Clowers, K.J.; Ji, F.; Schwarz, B.A.; Kalocsay, M.; Elledge, S.J.; et al. Nudt21 controls cell fate by connecting alternative polyadenylation to chromatin signaling. *Cell* **2018**, *172*, 106–120.e21; Erratum in *Cell* **2018**, *172*, 629–631. https://doi.org/10.1016/j.cell.2017.11.023.
35. Bartel, D.P. MicroRNAs: target recognition and regulatory functions. *Cell* **2009**, *136*, 215–233. https://doi.org/10.1016/j.cell.2009.01.002.
36. Kozomara, A.; Birgaoanu, M.; Griffiths-Jones, S. miRBase: from microRNA sequences to function. *Nucleic Acids Res.* **2019**, *47*, D155–D162. https://doi.org/10.1093/nar/gky1141.
37. Clarke, A.W.; Høye, E.; Hembrom, A.A.; Paynter, V.M.; Vinther, J.; Wyrożemski, Ł.; Biryukova, I.; Formaggioni, A.; Ovchinnikov, V.; Herlyn, H.; et al. MirGeneDB 3.0: improved taxonomic sampling, uniform nomenclature of novel conserved microRNA families and updated covariance models. *Nucleic Acids Res.* **2025**, *53*, D116–D128. https://doi.org/10.1093/nar/gkae1094.
38. Clancy, J.L.; Patel, H.R.; Hussein, S.M.I.; Tonge, P.D.; Cloonan, N.; Corso, A.J.; Li, M.; Lee, D.S.; Shin, J.Y.; Wong, J.J.L.; et al. Small RNA changes en route to distinct cellular states of induced pluripotency. *Nat. Commun.* **2014**, *5*, 5522. https://doi.org/10.1038/ncomms6522.
39. Cacchiarelli, D.; Trapnell, C.; Ziller, M.J.; Soumillon, M.; Cesana, M.; Karnik, R.; Donaghey, J.; Smith, Z.D.; Ratanasirintrawoot, S.; Zhang, X.; et al. Integrative analyses of human reprogramming reveal dynamic nature of induced pluripotency. *Cell* **2015**, *162*, 412–424. https://doi.org/10.1016/j.cell.2015.06.016.
40. Rosado-Tristani, D.A.; Albu, M.; Chen, X.; Sasse, A.; Laverty, K.U.; Ray, D.; Tam, C.L.; Ernst, K.; Lawson, L.P.; Morris, Q.D.; et al. CisBP-RNA: a web resource for eukaryotic RNA-binding proteins and their motifs. *Nucleic Acids Res.* **2026**, *54*, D98–D105. https://doi.org/10.1093/nar/gkaf1081.
41. Grant, C.E.; Bailey, T.L.; Noble, W.S. FIMO: scanning for occurrences of a given motif. *Bioinformatics* **2011**, *27*, 1017–1018. https://doi.org/10.1093/bioinformatics/btr064.
42. Marson, A.; Levine, S.S.; Cole, M.F.; Frampton, G.M.; Brambrink, T.; Johnstone, S.; Guenther, M.G.; Johnston, W.K.; Wernig, M.; Newman, J.; et al. Connecting microRNA genes to the core transcriptional regulatory circuitry of embryonic stem cells. *Cell* **2008**, *134*, 521–533. https://doi.org/10.1016/j.cell.2008.07.020.

43. Asikainen, S.; Heikkinen, L.; Juhila, J.; Holm, F.; Weltner, J.; Trokovic, R.; Mikkola, M.; Toivonen, S.; Balboa, D.; Lampela, R.; et al. Selective microRNA-offset RNA expression in human embryonic stem cells. *PLoS One* **2015**, *10*, e0116668. https://doi.org/10.1371/journal.pone.0116668.
44. Choi, Y.J.; Lin, C.P.; Ho, J.J.; He, X.; Okada, N.; Bu, P.; Zhong, Y.; Kim, S.Y.; Bennett, M.J.; Chen, C.; et al. miR-34 miRNAs provide a barrier for somatic cell reprogramming. *Nat. Cell Biol.* **2011**, *13*, 1353–1360. https://doi.org/10.1038/ncb2366.
45. Judson, R.L.; Babiarz, J.E.; Venere, M.; Blelloch, R. Embryonic stem cell-specific microRNAs promote induced pluripotency. *Nat. Biotechnol.* **2009**, *27*, 459–461. https://doi.org/10.1038/nbt.1535.
46. Agarwal, V.; Lopez-Darwin, S.; Kelley, D.R.; Shendure, J. The landscape of alternative polyadenylation in single cells of the developing mouse embryo. *Nat. Commun.* **2021**, *12*, 5101. https://doi.org/10.1038/s41467-021-25388-8.
47. Fort, V.; Khelifi, G.; He, R.; Watters, V.; Pye, M.; Yamanaka, N.; Gertsenstein, M.; Lelong, É.I.J.; Loehr, J.; Micha, V.; et al. Long-read RNA sequencing identifies non-coding isoform switching as a regulator of cell fate. *Nat. Commun.* **2026**, *17*, 11111. https://doi.org/10.1038/s41467-026-78011-z.
48. Leung, A.K.L.; Young, A.G.; Bhutkar, A.; Zheng, G.X.; Bosson, A.D.; Nielsen, C.B.; Sharp, P.A. Genome-wide identification of Ago2 binding sites from mouse embryonic stem cells with and without mature microRNAs. *Nat. Struct. Mol. Biol.* **2011**, *18*, 237–244; Erratum in *Nat. Struct. Mol. Biol.* **2011**, *18*, 1084. https://doi.org/10.1038/nsmb.1991.
49. Siepel, A.; Bejerano, G.; Pedersen, J.S.; Hinrichs, A.S.; Hou, M.; Rosenbloom, K.; Clawson, H.; Spieth, J.; Hillier, L.W.; Richards, S.; et al. Evolutionarily conserved elements in vertebrate, insect, worm, and yeast genomes. *Genome Res.* **2005**, *15*, 1034–1050. https://doi.org/10.1101/gr.3715005.
50. Firth, D. Bias reduction of maximum likelihood estimates. *Biometrika* **1993**, *80*, 27–38. https://doi.org/10.1093/biomet/80.1.27.
51. Neumann, D.P.; Pillman, K.A.; Dredge, B.K.; Bert, A.G.; Phillips, C.A.; Lumb, R.; Ramani, Y.; Bracken, C.P.; Hollier, B.G.; Selth, L.A.; et al. The landscape of alternative polyadenylation during EMT and its regulation by the RNA-binding protein Quaking. *RNA Biol.* **2024**, *21*, 199–209. https://doi.org/10.1080/15476286.2023.2294222.
52. Oh, J.M.; Venters, C.C.; Di, C.; Pinto, A.M.; Wan, L.; Younis, I.; Cai, Z.; Arai, C.; So, B.R.; Duan, J.; et al. U1 snRNP regulates cancer cell migration and invasion in vitro. *Nat. Commun.* **2020**, *11*, 1. https://doi.org/10.1038/s41467-019-13993-7.
53. The UniProt Consortium. UniProt: the Universal Protein Knowledgebase in 2025. *Nucleic Acids Res.* **2025**, *53*, D609–D617. https://doi.org/10.1093/nar/gkae1010.